Title
Low temperature studies on chemically substituted correlated electron systems

Author
Pouse, Naveen

Publication Date
2018

UNIVERSITY OF CALIFORNIA SAN DIEGO

Low temperature studies on chemically substituted correlated electron systems

A dissertation submitted in partial satisfaction of the
requirements for the degree Doctor of Philosophy

in

Physics

by

Naveen Pouse

Committee in charge:

Professor M. Brian Maple, Chair
Professor Daniel P. Arovas
Professor Richard Averitt
Professor Eric Fullerton
Professor Congjun Wu

2018

The Dissertation of Naveen Pouse is approved and is acceptable in quality and form for publication on microfilm and electronically:

Chair

University of California San Diego

2018

TABLE OF CONTENTS

LIST OF FIGURES

ACKNOWLEDGEMENTS

I would like to acknowledge the many people who have helped me become who I am today both as a person and as a member of the scientific community.

I would like to thank Dr. Brian Maple for his support and guidance throughout my Ph.D. program. As a member of Brian's lab, I have learned a lot about what it takes to be successful in a competitive field and how to carry myself as a professional as well as an ambassador for the groups and organizations I have represented or will represent in the future. Working in the Maple lab has taught me how to develop into someone that can be counted as well as allowing me to build confidence so that I can be a leader.

Throughout my academic and research career, I have had the fortune to work with a lot of great people, too many for me to name. I would like to acknowledge the many research collaborators with whom I have worked on interesting projects and learned how to expand my research horizon. I would like to thank my fellow lab members, both former and current: postdocs who taught me how to be a good scientist, fellow graduate students who were there to help when I needed it and made my PhD program a unique experience, and undergraduate interns who were both willing and able to aid in my research when I became overwhelmed. I want to also thank the many professors with whom I have taken courses and who tested the boundaries of my knowledge while I grew into a critical thinker. I would also like to acknowledge the many different staff members I have worked or interacted with from both the Physics department or outside who went out of their way to help me so that I could focus on research.

To my many friends, whether you are in San Diego or are elsewhere, I would like to say thank you. There are too many times for me to remember where I needed advice and you were there to help no matter how many times I bombarded you with questions. Thanks for all the times when you were there just to have a drink, talk, or watch sports when I was stressed with work. I look forward to keeping in touch with all of you as we progress through our careers.

Thank you to my family and close family friends who always supported me even when I did not know what I wanted in life and needed help. Thank you for your various forms of support in times where maybe I did not deserve it or ask for it, but you knew I needed it anyway. I will never forget all the things you did for me, both big and small, so that I could focus on what was in front of me.

To my younger brother Winston, I look forward to reading your Ph.D. dissertation in a few years. Even though you are my younger brother, I still learned a lot from you. Your determination and focus has often inspired me to set a good example for others. I know you will do well no matter what career you decide to pursue, whether it is in physics research or somewhere else. I hope that you were able to learn from both my successes and my mistakes.

Finally, and most importantly, thank you Amma and Appa. Things were not always smooth, but the times that were easy were because you gave everything: your health, your time, your money, and countless other immeasurable things so that Winston and I could have a comfortable life. No matter what I do or say, I will never forget what it took for me to get here. There were so many times you could have taken a day off or quit, but you didn't because that's how much you cared about me and my future. My name is not on a Physics Ph.D. degree without your sacrifice. I am thrilled to share this accomplishment with you.

Chapter 2, in part is currently being prepared for submission for publication of the material. Pouse, N., Yazici, D., Friedman, A. J., Maple, M. B. The dissertation author was the primary investigator and author of this material.

Chapter 3, in full, is a reprint of the material as it appears in Physical Review B (2018). Jang, S., Pouse, N., Keiber, T., White, B. D., Disseler, S. M., Lynn, J. W., Collini, J. C., Janoschek, M., Bridges, F., Maple, M. B., APS, 2018. The dissertation author was the primary investigator and author of this paper.

Chapter 4, in full, is a reprint of the material as it appears in Physical Review B (2018). Pouse, N., Jang, S., White, B. D., Ran, S., Adhikari, R. B., Almasan, C. C., Maple, M. B., APS, 2018. The dissertation author was the primary investigator and author of this paper.

Chapter 5, in part is currently being prepared for submission for publication of the material. Pouse, N., Ran, S., Graf, D., Lai, Y., Singleton, J., Balakirev, F. F., Baumbach, R. E., Maple, M. B. The dissertation author was the primary investigator and author of this material.

VITA

2012	B.S. in Physics, Georgia Institute of Technology
2014	M.S. in Physics, University of California San Diego
2018	Ph.D. in Physics, University of California San Diego

PUBLICATIONS

Pouse, N., Ran, S., Graf, D., Lai, Y., Singleton, J., Balakirev, F. F., Baumbach, R. E., Maple, M. B., “$URu_{2-x}Fe_xSi_2$,” In preparation (2018).

Pouse, N., Yazici, D., Friedman, A. J., Maple, M. B., “$Yb_{1-x}Sc_xCo_2Zn_{20}$,” In preparation (2018).

Jang, S., **Pouse, N.**, Keiber, T., White, B. D., Disseler, S. M., Lynn, J. W., Collini, J. C., Janoschek, M., Bridges, F., Maple, M. B., “Tuning the magnetic ground state of $Ce_{1-x}Yb_xRhIn_5$ by Yb valence fluctuations,” Physical Review B 98, 195118.

Pouse, N., Jang, S., White, B. D., Ran, S., Adhikari, R. B., Almasan, C. C., Maple, M. B., “Temperature versus Sm concentration phase diagram and quantum criticality in the correlated electron system $Ce_{1-x}Sm_xCoIn_5$,” Physical Review B 97 (23), 235149.

Jeon, I., Huang, K., Yazici, D., Kanchanavatee, N., White, B. D., Ho, P.-C., Jang, S., **Pouse, N.**, Maple, M. B., “Investigation of superconducting and normal-state properties of the filled-skutterudite system $PrPt_4Ge_{12-x}Sb_x$,” Physical Review B 93 (10), 104507.

Ran, S., Jeon, I., **Pouse, N.**, Breindel, A. J., Kanchanavatee, N., Huang, K., Gallagher, A., Chen, K.-W., Graf, D., Baumbach, R. E., Singleton, J., Maple, M. B., “Phase diagram of $URu_{2-x}Fe_xSi_2$ in high magnetic fields,” Proceedings of the National Academy of Sciences 114 (37), 9826-9831.

Ran, S., Wolowiec, C. T., Jeon, I., **Pouse, N.**, Kanchanavatee, N., White, B. D., Huang, K., Martien, D., DaPron, T., Snow, D., Williamsen, M., Spagna, S., Riseborough, P. S., Maple, M. B., “Phase diagram and thermal expansion measurements on the system $URu_{2-x}Fe_xSi_2$,” Proceedings of the National Academy of Sciences 113 (47), 13348-13353.

Huang, K., Yazici, D., White, B. D., Jeon, I., Breindel, A. J., **Pouse, N.**, Maple, M. B. (2016). “Superconducting and normal state properties of the systems $La_{1-x}M_xPt_4Ge_{12}$

(M= Ce, Th),” Physical Review B, 94(9), 094501.

White, B. D., Yazici, D., Ho, P.-C., Kanchanavatee, N., **Pouse, N.**, Fang, Y., Breindel, A. J., Friedman, A. J., Maple, M. B. “Weak hybridization and isolated localized magnetic moments in the compounds $\mathrm{Ce}T_2\mathrm{Cd}_{20}$ (T= Ni, Pd),” Journal of Physics: Condensed Matter 27 (31), 315602.

ABSTRACT OF THE DISSERTATION

Low temperature studies on chemically substituted correlated electron systems

by

Naveen Pouse

Doctor of Philosophy in Physics

University of California San Diego, 2018

Professor M. Brian Maple, Chair

The research presented in this dissertation is a result of several chemical substitution studies on correlated electron systems. Through careful synthesis and measurement at low temperatures, we create lanthanide- and actinide-based compounds and environments in which various exotic phenomena can be studied in detail. Such phenomena include heavy fermion behavior (HF), superconductivity (SC), exotic magnetic ordering, the Kondo effect, valence fluctuations, non-Fermi liquid behavior (NFL), quantum criticality, among many others. Not only are these phenomena probed through measurements at extreme conditions like low temperatures down to 30 mK and high magnetic fields up

to 65 T, but they are also studied as the electronic structure is modified through the substitution of atoms. By providing a detailed survey of certain correlated electron systems through multiple measurement techniques, we hope to better understand the underlying physical phenomena which drive the macroscopic behavior in these compounds which have been the subject of great interest for decades.

Chapter 1

Introduction

We discuss various physical phenomena common to correlated electron systems and present our research highlights from the dissertation work. In particular, our research was focused on utilizing chemical substitution as a tuning parameter to observe how various correlated electron systems behave in response to changes to the chemical composition which include studying the evolution of these physical phenomena as a function of chemical substitution, x. The following phenomena are critical to our understanding of the results of these studies:

1.1 Heavy fermion behavior

Heavy fermion behavior is behavior in a system such that the effective mass of a fermion system is several orders of magnitude larger than the mass of an electron, $m^*/m_e >> 1$, where $m_e = 9.11 \times 10^{-31}$ kg. The fermion mass is characterized in many ways, the most direct of which is calculation via measurements of the electronic structure, which provides detailed information on the Fermi surface. Using techniques such as angle resolved photoemission spectroscopy (ARPES), one can calculate m^*. Additionally, one can model low temperature resistivity according to Fermi liquid theory using the equation $\rho = \rho_0 + AT^2$. The coefficient A is proportional to the density of states (DOS), which is a reflection of m^*. Another method of characterizing m^* lies in the modeling of the low-temperature behavior of a system's specific heat, C, according to the Debye approximation, $C = \gamma T + \beta T^3$. In this model, γ is the Sommerfeld coefficient which reflects the electronic contribution to the total specific heat. γ is also proportional to the effective mass m^*, which means a large Sommerfeld coefficient is indicative of heavy fermion behavior. A ratio of A/γ^2, known as the Kadowaki-Woods ratio (KWR), is used to classify heavy fermion behavior.[6] The KWR is shown to be independent of the material and is approximately 25 times larger for heavy fermion systems in comparison to normal metals.

1.2 The Kondo effect

The Kondo effect is a phenomenon in which a conducting material exhibits an upturn in electrical resistivity at low temperatures. This phenomenon contrasts the typical behavior of a conductor where resistivity decreases monotonically as $T \to 0$ K, which reflects the relationship between the cooling of the conductor resulting in weaker phonon behavior and decreased electron scatter. Jun Kondo provided a theoretical model for this phenomenon where the increase in low-temperature resistivity can be attributed to electron scatter off of other conduction electrons which establish spin interactions with magnetic impurities.[3] Since these spin interactions are more favorable at low-temperature, depending on the amount of magnetic impurity ions, this effect becomes the main contributor to the electrical resistivity.

When the concentration of magnetic impurities is low, the Kondo effect contribution to the resistivity is a logarithmic expression and can be expressed as $\rho = A \ln T$, where A is proportional to the concentration of magnetic impurities. This is often described as the single-ion Kondo effect.

Additionally, when the spin pairing between conduction electrons and magnetic ions happens not just with the impurity ions, but with many of the host ions throughout the lattice, coherence is developed. Instead of the logarithmic divergence of resistivity with $T \rightarrow 0$ K, one might observe a steady increase in resistivity before sharply decreasing, leading to a local resistivity maximum. This resistivity maximum is known as a Kondo coherence peak, where the Kondo effect stops being localized to the impurities (single-ion Kondo effect) and becomes prevalent across the lattice. The periodicity of this behavior results in a coherence that develops at lower temperatures, which is why the resistivity drops after increasing.

1.3 Valence fluctuations in correlated electron systems

Since the focus of this dissertation work was on lanthanide- or actinide-based correlated electron systems, the valence of the individual $4f$ or $5f$ ions becomes critical to the behavior of the overall system. The valence of each of these ions can take on multiple states, though they often tend to stabilize in the trivalent (3+) state in the compounds we study. For example, the various ions we might observe are: $\text{Ce}^{3+,4+}$, $\text{Sm}^{2+,3+}$, $\text{Yb}^{2+,3+}$, or $\text{U}^{3+,4+,5+,6+}$.

1.4 Superconductivity

Since discovery of the superconductivity of mercury in 1911 by Kamerlingh Onnes,[7] and subsequent findings of the expulsion of magnetic fields in superconductors in 1933, known as the Meissner effect,[8] much effort has gone into the research and development of new superconductors due to their potential for significant applications. The ability for materials to exhibit zero electrical resistance has huge implications, from being used as high field magnets, to applications for power transmission, as well as many other potential uses in the future. One critical development in the medical field has been the introduction of superconducting magnets, which are high efficiency magnets that make MRI machines much more accessible as a technology. The history of superconductivity will be discussed in the following sections with a brief introduction to the underlying phenomena and their relation to the development of the field of correlated electron systems.

key points: how magnetism affects unconventional superconductivity, quantum critical points, common materials

1.4.1 Conventional superconductivity

When the theory of superconductivity is discussed, one often talks about conventional or “BCS”-type superconductivity, which comes out of Ginzberg-Landau theory[9] and is described by Bardeen, Cooper, Schreiffer (BCS) theory.[10] The novel description of the electric current in superconductors below their superconducting critical temperature, T_c, was that “Cooper pairs” would form at sufficiently low temperatures and move as part of a superfluid following Bose-Einstein statistics. Cooper pairs can be thought of as electrons pairing indirectly through an electron-phonon interaction. As an electron moves through the lattice at low temperatures, it locally attracts the ions in the lattice, which is treated as a phonon, a quasiparticle. This local displacement of phonons results in an electric force on another electron, dragging this second electron toward the first electron, thereby creating a pair of electrons, which can be identified as a boson. BCS theory was a revolutionary theory for condensed matter, and was long thought to be the only way for superconductivity to exist in a system and that T_c should accordingly be below approximately 30 K. However, in 1986, the ”cuprate” superconductor LaBaCuO[11] was found to exhibit superconductivity at 35 K, and later YBaCuO (YBCO) at 92 K.[12] This ”high temperature superconductivity” suggested that the BCS theory was not sufficient for describing all superconductivity, leading to attempts to formulate theory describing the phenomenon known as “unconventional superconductivity”.

1.4.2 Unconventional superconductivity

Unconventional superconductors tend to exhibit most phenomena common to conventional superconductivity, however the underlying mechanisms for their behavior are different. One possibility is the idea that phonons may not be the pairing mechanism. Other potential scenarios are the non-zero angular momentum of the electron pair's wave function where the symmetry is either $p-$ or $d-$wave symmetric. Unconventional superconductivity is what allows researchers to realize superconductivity well above 30 K to the point that they can be commonly used in technology. The development of Josephson junctions, superconducting electronics, and high powered electromagnets would be very difficult if limited to conventional superconductivity. While discovered T_c values continue to approach room temperature, we have yet to discover a useful superconducting material which can be utilized without cryogenics.

1.5 Quantum criticality

Quantum criticality is the behavior exhibited by a system near what is known as a quantum critical point (QCP). In a traditional phase transition, thermal fluctuations lead to abrupt phase changes. Quantitatively a phase transition can be identified with an order parameter approaching zero as the system nears its phase transition. A quantum phase transition is therefore a phenomena where quantum fluctuations yield a phase transition rather than thermal fluctuations. Tuning parameters such as magnetic field H, applied pressure P, or even chemical substitution x are non-thermal tuning parameters which can yield quantum phase transitions. A QCP is the point at where this quantum phase transition occurs at $T = 0$ K. A system in proximity to its QCP exhibits quantum criticality, where the system will display non-Fermi liquid (NFL) behavior. This behavior can be characterized by a low temperature divergence of specific heat divided by temperature

C/T or sub-quadratic temperature dependence of the resistivity ρ. Systems typically behave according to Fermi liquid theory near 0 K in a magnetically ordered state, so the crossover from Fermi liquid behavior to NFL behavior is a good way to characterize quantum phase transitions.

The goal of the research presented in this dissertation was to learn more about the various phenomena described above and find new ways to develop our understanding of these phenomena. Chemical substitution is therefore a very powerful way of probing these mechanisms, as modifications to the stoichiometry should reflect in slow, but systematic changes of these phenomena and yield further insight into the physics behind them. Our research presents the results of such chemical substitution studies where substitution shows quantitative changes in the heavy fermion behavior and the Kondo effect, valence fluctuations in Yb, suppression of SC, as well as the characterization of quantum criticality. Additionally we present results where chemical substitution was a method of applying chemical pressure rather than an attempt to modify electronic structure, as well as a study where we performed an intense study on quantum phase transitions under application of high magnetic fields. These all-encompassing studies will hopefully shed a broad light on these topics of interest so that future researchers can better understand which paths to take in further understanding these compounds.

1.6 Research highlights

In this section, we discuss the motivations for the studies conducted as part of this dissertation as well as the highlights of each study.

Chapter 1 - $\mathbf{Yb_{1-x}Sc_xCo_2Zn_{20}}$

Motivation

We performed various measurements on single crystals of $Yb_{1-x}Sc_xCo_2Zn_{20}$ from the so-called “1-2-20” class of heavy fermion compounds. Our motivation for studying $Yb_{1-x}Sc_xCo_2Zn_{20}$ came from the study on the YbT_2Zn_{20} family of 1-2-20s, where $M =$ Fe, Co, Ru, Rh, Os, or Ir.[1] These 1-2-20s were studied in particular because of their ability to provide a dilute environment in which to study Yb. $YbCo_2Zn_{20}$ was particularly interesting due to its abnormally heavy fermion behavior compared to the rest of the 1-2-20s, along with an apparent lack of magnetic ordering. This system also appeared to show a very strong single-ion-like Kondo effect. When pressure was applied to this system, magnetic ordering developed at very low temperatures.[13] Our goal with Sc-substitution for Yb in $YbCo_2Zn_{20}$ was to attempt to create a chemical pressure on the system to observe the same type of magnetic ordering without introducing additional magnetic moment.

Highlights

The major findings of this study include an apparent decrease in the valence of Yb^{3+} as Sc is substituted which shown by: (a) the insensitivity of the lattice constant $a(x)$ to Vegard’s law as Sc is substituted and (b) a drop in the effective magnetic moment of Yb as x is increased. The other major finding is the behavior of the single-ion Kondo effect which is suppressed with increasing x which can be characterized using the decrease of the strength of the Kondo contribution to the electrical resistivity and the evolution of the angular momentum, J, and the Kondo temperature, T_K, which are parameters extracted from the fitting of the resonance-level model to the specific heat of $Yb_{1-x}Sc_xCo_2Zn_{20}$.[14] Despite substitution of non-magnetic Sc, Yb is shown to change behavior uncharacteristically in an otherwise dilute 1-2-20 system, and makes

$Yb_{1-x}Sc_xCo_2Zn_{20}$ a good subject of further study due to the link between the valence behavior of Yb and the single-ion Kondo effect.

Chapter 2 - $Ce_{1-x}Yb_xRhIn_5$

Motivation

The chemical substitution study of the compound $Ce_{1-x}Yb_xRhIn_5$ was highly motivated by the related study on $Ce_{1-x}Yb_xCoIn_5$. The “1-1-5” system known as $CeCoIn_5$ is well-known heavy fermion superconductor which is unique in being Ce-based while having a relatively high superconducting critical temperature with $T_c = 2.3$ K. The superconductivity in this compound is unconventional with d-wave symmetry. Additionally, a Kondo coherence behavior is observed at high temperatures. When Yb was substituted into $CeCoIn_5$, a myriad of phenomena, such as valence transitions and Fermi surface (FS) reconstructions, are observed which are further discussed in the described chapter. The related 115 compound $CeRhIn_5$ exhibits magnetic ordering in the ground state in contrast to the superconductivity of $CeCoIn_5$. We attempted a similar substitution of Yb into this system to compare and contrast the behavior of $Ce_{1-x}Yb_xRhIn_5$ with that of $Ce_{1-x}Yb_xCoIn_5$.

Highlights

$Ce_{1-x}Yb_xRhIn_5$ exhibited various types of phenomena dependent on Yb concentration x, much like the sister compound $Ce_{1-x}Yb_xCoIn_5$. In particular, Yb exhibited valence instability as it was substituted into the Ce site, with the valence of Yb decreasing from 3+ to 2.1+ by $x_{\text{act}} = 0.2$. This valence behavior potentially led to many of the other observed phenomena which could be better understood if one were to study the dependence of the Fermi surface on x which would suggest changes in the electronic structure. One such x-dependent phenomena was the change in the magnetic structure from commensurate to incommensurate. While $Ce_{1-x}Yb_xRhIn_5$ represents a substitution study on a magnetic system, its similarities to $Ce_{1-x}Yb_xCoIn_5$ could yield valuable insight on how to further study $Ce_{1-x}Yb_xRhIn_5$.

Chapter 3 - $Ce_{1-x}Sm_xCoIn_5$

Motivation

Our study on $Ce_{1-x}Sm_xCoIn_5$ was also motivated by the study on $Ce_{1-x}Yb_xCoIn_5$. Due to the various phenomena observed in $Ce_{1-x}Yb_xCoIn_5$ as a result of valence fluctuations in Yb, by using an analogous lanthanide in Sm, which can exhibit both trivalent and divalent states, we hoped to observe similar effects by substituting Ce for Sm in $CeCoIn_5$.

Highlights

Instead, Sm was found to remain trivalent throughout the full concentration range $0 \leq x \leq 1$. However, due to the parent compound $SmCoIn_5$ exhibiting three unique magnetic ordering phases, we instead were able to study a system which had competing phases in SC from $CeCoIn_5$ and AFM from $SmCoIn_5$. This study yielded a quantum critical point near the concentration $x = 0.15$, near which NFL behavior was observed in both specific heat and electrical resistivity. $Ce_{1-x}Sm_xCoIn_5$ is a good candidate for a compound where the competition between magnetism and SC can be studied and its quantum critical point can be further explored.

Chapter 4 - $URu_{2-x}Fe_xSi_2$

Motivation

The heavy fermion compound URu_2Si_2 has been an important topic of in the study of correlated electron systems for decades. At 17.5 K, URu_2Si_2 goes through a transition of which the order parameter is unknown. This transition is famously known as "hidden order" (HO) and has been a highly controversial topic since its discovery.[15,16,17]

Numerous theories and hypotheses have been put forth as to what HO is; however, none have been able to fully explain this phase transition. One common attempt to probe this phase transition is through the application of pressure on the system.[18] Additionally, the substitution of Fe into the Ru site has been shown to also apply a "chemical pressure" to the system.[19,20,21] This substitution gives us the ability to perform difficult measurements on URu_2Si_2 without having to apply external pressure - one such measurement being the measurement of resistance at high magnetic fields. In applying this pressure, the introduction of a large-moment antiferromagnetic (LMAFM) phase is made at $x = 0.15$.[22] LMAFM is peculiar because it appears similar to HO throughout multiple measurements, however the magnetic moment of U in the LMAFM is much higher than that of the HO. One avenue of study in addition to probing HO is to study the differences between HO and LMAFM. The motivation of the following study was to study URu_2Si_2 under chemical pressure through Fe substitution, at high magnetic fields ($0 < B < 45$ T) like the study performed in Ref. 23 with the key difference being that B was applied at some angle θ to the c-axis of URu_2Si_2. This thorough study provides us a full phase diagram of essentially four tuning parameters (T, B, x, θ) which allows a thorough probing of the HO phase. The aim is to better understand HO as it responds to these tuning parameters in $URu_{2-x}Fe_xSi_2$.

Our study follows in the footsteps of two previous reports: Ref. 24 where the magnetoresistance of URu_2Si_2 was measured through the HO transition under a magnetic field which was rotated from $H//ab$ to $H//c$, and Ref. 23 where $URu_{2-x}Fe_xSi_2$ was studied at high magnetic fields where $H//c$. Ref. 24 characterized the behavior of URu_2Si_2 under a rotated magnetic field as exhibiting higher-order symmetry (4-, 6-, and 8-fold) at the HO transition. Ref. 23 maps out a full three-dimensional phase diagram (T, H, and x) for $URu_{2-x}Fe_xSi_2$ and shows the behavior of HO and LMAFM under high fields, as well as the existence and location of various other high field phases such as spin-density wave (SDW), Fermi surface reconstruction (FS), resistance maximum, among others. Additionally, the study conducted by[25] performs high field measurements on the resistance of URu_2Si_2 at various angles. This particular study showed that for URu_2Si_2, the phase diagram was insensitive to the angle - any apparent angle-dependent behavior was actually the result of the system depending on $H//c$, such that $H//c = H\cos\theta$, where θ is the angle between H and the c-axis of URu_2Si_2. Our goal was to reconcile the results of these three studies and to gain further insight into $URu_{2-x}Fe_xSi_2$, and by extension, the HO.

Highlights

In continuing the study of Ref. 24 on $URu_{2-x}Fe_xSi_2$ at higher fields, using the facilities at the National High Magnetic Field Laboratory (NHMFL), we attempted to characterize the apparent high order symmetries introduced in transitions through the HO phase. In particular, we were curious to see if this behavior extended to compounds where $x > 0$, and if the behavior existed in the same capacity at the LMAFM phase transition. Any changes between the HO and LMAFM phases would yield valuable insight in making a clear distinction between the two phases which has so far been difficult to do.

We attempted to reconcile results reported by Scheerer *et al.*[25] with those reported by Kanchanavatee *et al.*[24] as they should be measuring the same phenomena, and to do so, we converted R vs. θ data, which was guided by Kanchanavatee *et al.*, into R vs. $H//c$. After doing this, we found that any apparent increase in angular symmetry was actually a reflection of phase transitions at a critical $H\cos\theta$, which allowed us to construct our own phase diagram from these measurements. The phase diagram not only showed agreement with Scheerer *et al.* that $H\cos\theta$ is the tuning parameter, we were also able to completely reconstruct the phase diagram shown by Ran *et al.*,[23] meaning that

$URu_{2-x}Fe_xSi_2$ did not depend on H or θ individually, but depends on $H\cos\theta$ throughout the entire phase diagram. Our finding was that the study by Scheerer *et al.* extends up to $x = 0.3$ for $URu_{2-x}Fe_xSi_2$ even when the LMAFM phase is the ground state. Finally, the phase boundaries between LMAFM and HO, LMAFM and the paramagnetic phase (PM), and the HO and PM phases were all characterized. We show that the transition between HO and LMAFM has a very weak signature and happens abruptly, whereas the transition from the PM phase to either the HO or LMAFM phase is near identical in behavior, which continues to show how indistinguishable the two phases are. The LMAFM phase appears to be a subset of HO behavior based on the constructed phase diagram.

The findings presented in this study are useful because we have shown that there is no angle-dependent behavior of $URu_{2-x}Fe_xSi_2$ for any of the phases, not just HO, and also because it presents an interesting perspective on the differences between the HO and LMAFM phases.

Chapter 2

Yb valence fluctuations and Kondo-like behavior in the $Yb_{1-x}Sc_xCo_2Zn_{20}$ system

We report x-ray powder diffraction (XRD), energy-dispersive x-ray spectroscopy (EDX), magnetization (M), specific heat (C), and electrical resistivity (ρ) measurements on the heavy fermion system $Yb_{1-x}Sc_xCo_2Zn_{20}$ for $0 \leq x \leq 1$. The Yb valence, v_{Yb}, calculated from XRD and $M(T)$ measurements, decreases linearly from $\sim 3+$ at $x = 0$ to $\sim 2.7+$ at $x = 0.3$ before stabilizing back at $\sim 3+$ for $0.3 < x \leq 1$. Additionally, $\rho(T)$ measurements reveal a low-temperature upturn consistent with Kondo-like scattering, where the upturn can be described by a $\log T$-dependence according to the prediction of the single ion Kondo model. The Kondo-like behavior can be separated into the same two regimes which correspond to the behavior of the Yb valence, suggesting that the Kondo-like behavior persists in the range where $2.7 \leq v_{\mathrm{Yb}} \leq 3+$ in $Yb_{1-x}Sc_xCo_2Zn_{20}$. For $0 \leq x \leq 0.3$, the Kondo contribution to the resistivity is large and robust but becomes much weaker in the region $0.3 < x \leq 1$. $C(T)$ measurements also show signatures which maybe indicative of valence fluctuations of the Yb ion and the strength of the Kondo effect. The specific heat, $C(T)$, data are analyzed according to the resonance level model (RLM). The $Yb_{1-x}Sc_xCo_2Zn_{20}$ system appears to show a confluence of phenomena typically found in $4f$ electron systems including crystalline electric field effects, valence fluctuations, the Kondo effect, and heavy fermion behavior.

2.1 INTRODUCTION

Intermetallic compounds containing Yb have attracted considerable interest due to the possible instability of the Yb $4f$ electron shell which is induced by hybridization between the Yb localized $4f$ and conduction electron states. This provides an opportunity to investigate and tune the interplay of magnetic order, heavy fermion (HF) behavior, and quantum criticality. In these compounds, two nearly degenerate Yb valence configurations, Yb^{2+} ($4f^{14}$) (non-magnetic) and Yb^{3+} ($4f^{13}$) (magnetic) states coexist in the intermediate valence IV state with temporal and quantum mechanical fluctuations between these states accompanied by the emission and absorption of an electron to and from the conduction band. This happens when the difference in Fermi energy E_F and $4f$ energy level E_f is comparable to the width of the hybridized 4_f level.[26,27,28,29]

$\mathrm{YbCo_2Zn_{20}}$ is a particularly interesting correlated electron system due to the following qualitative differences observed by Torikachvili *et al.*[1] from thermodynamic and transport measurements on this system: (1) Magnetization, $M(H,T)$, measurements show no apparent contribution from itinerant magnetism as the magnetic susceptibility, $\chi(T)$, of $\mathrm{YbCo_2Zn_{20}}$ strictly obeys a Curie-Weiss law for all temperatures above 1.8 K, (2) Measurements of $\rho(T)$ also show a low-temperature feature reminiscent of single-ion Kondo scattering with phonon contributions apparently comprising the high-temperature $\rho(T)$, and (3), though the Kadowaki-Woods ratio is on the same order of magnitude for $\mathrm{Yb}M_2\mathrm{Zn}_{20}$ $M=$Fe, Ru, Rh, Os, Ir, the individual values of A, the coefficient of the low-T quadratic term in $\rho(T)$, and γ, the Sommerfeld coefficient of the specific heat, are much larger, indicating abnormally heavy fermion behavior.

The strength of the hybridization between the localized $f-$ and conduction electrons can be controlled by pressure and chemical substitution, and hence nonmagnetic-magnetic and/or valence quantum phase transitions are expected. In this system, application of pressure to $\mathrm{YbCo_2Zn_{20}}$ is shown by Saiga *et al.* to induce a magnetically-ordered ground state - this transition is determined by a feature in $\rho(T)$ at T_M and a deviation from Fermi-liquid behavior.[13]

To further investigate the relationship between pressure and the magnetically-ordered ground state of Yb, chemical substitution of Sc for Yb was undertaken to tune the properties of $\mathrm{YbCo_2Zn_{20}}$. Chemical pressure can be introduced by partial substitution of Yb by smaller Sc ions. Being able to access the magnetically-ordered state without applying external pressure could allow for a more diverse set of measurements to probe the nature of the ground state and to better understand the role of Yb in correlated electron systems.

The major findings of this study include an apparent decrease in the valence of $\mathrm{Yb^{3+}}$ as Sc is substituted which shown by: (a) the insensitivity of the lattice constant $a(x)$ to Vegard's law as Sc is substituted and (b) a drop in the effective magnetic moment of Yb as x is increased. The other major finding is the behavior of the single ion Kondo-like behavior which is suppressed with increasing x and can be characterized using the decrease of the strength of the Kondo contribution to the electrical resistivity as well as the evolution of the angular momentum, J, and the Kondo temperature, T_K, which are parameters extracted from the fitting of the resonance-level model to the specific heat of $\mathrm{Yb_{1-x}Sc_xCo_2Zn_{20}}$.[14] Despite substitution of non-magnetic Sc, Yb is shown to change behavior uncharacteristically in an otherwise dilute 1-2-20 system, and makes $\mathrm{Yb_{1-x}Sc_xCo_2Zn_{20}}$ a good subject of further study due to the link between the valence behavior of Yb and the single ion Kondo-like behavior.

2.2 EXPERIMENTAL DETAILS

Single crystalline samples of $Yb_{1-x}Sc_xCo_2Zn_{20}$ were grown using a molten Zn flux as described in Ref. 30. The crystal structure was characterized through analysis of powder x-ray diffraction patterns collected by a Bruker D8 Discover X-ray diffractometer using a Cu-K_α source. Four-wire electrical resistivity measurements were performed from 300 K down to $\sim$ 1.1 K in a pumped ^{4}He Dewar. Magnetization measurements were performed between 300 and 2 K in a Quantum Design Magnetic Property Measurement System (MPMS) equipped with a 7 T superconducting magnet. Specific heat measurements were performed down to 1.8 K using a Quantum Design Physical Property Measurement System (PPMS) DynaCool. The heat capacity measurements employed a standard thermal relaxation technique. The chemical composition of $Yb_{1-x}Sc_xCo_2Zn_{20}$ was investigated by means of energy-dispersive x-ray spectroscopy (EDX) using an FEI Quanta 250 scanning electron microscope equipped with an UltraDry EDS detector from Thermo Scientific.

2.3 RESULTS

2.3.1 Crystal Structure

Rietveld refinements were performed on data collected from XRD measurements for each sample using GSAS[31] and EXPGUI.[32] The $Yb_{1-x}Sc_xCo_2Zn_{20}$ system exhibits a single cubic $CeCr_2Al_{20}$ structure with space group $Fd\overline{3}m$ over the entire range of x at room temperature. A representative XRD pattern ($x = 0.7$) is shown in Fig. 2.1. The measured XRD data are plotted in black and the calculated Bragg reflection pattern is plotted as a red line; the blue line is the measured XRD data from which the calculated XRD data from Rietveld refinement has been subtracted. The agreement between the patterns and the refinement results was excellent for all samples with typical reduced χ^2

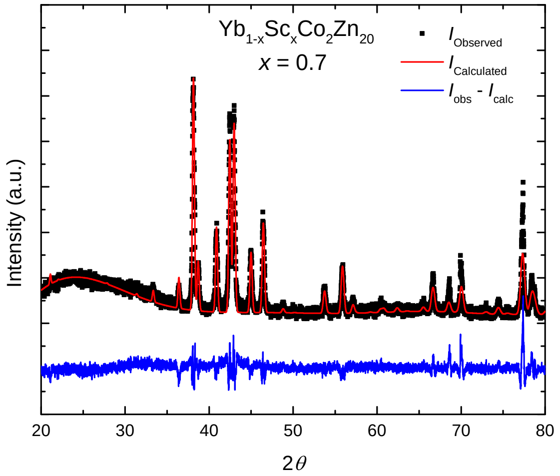

Figure 2.1. Powder XRD pattern for a representative concentration of $Yb_{1-x}Sc_xCo_2Zn_{20}$ ($x = 0.7$) at room temperature (black squares), fit from Rietveld refinement (red line), and the difference between the measured data and the fit (blue line). The XRD pattern shows a small background signal with no clear impurity peaks suggesting a high sample quality with the expected 1-2-20 structure.

values less than 5.

The calculated lattice parameter $a(x)$ is plotted in Fig. 2.2 and shows two separate regimes of behavior with increasing x: nearly constant $a(x)$ for $0 \leq x \leq 0.3$ and a standard Vegard's law behavior in a for $0.3 < x \leq 1$. The behavior is visualized in the inset of Fig. 2.2 by the shifting of the (531) Bragg peak with x. This change in behavior of $a(x)$ is attributed to the decrease in Yb valence as a function of x in the region $0 \leq x \leq 0.3$ and is further discussed in the 'Discussion' section. The ionic radius of Sc is less than that of Yb, suggesting that chemical pressure is induced in $Yb_{1-x}Sc_xCo_2Zn_{20}$, which is aligned with our goal of trying to observe the pressure-induced magnetic transition in the parent compound $YbCo_2Zn_{20}$.[13] However, this system presents an unexpected, yet interesting result in that the lattice parameter does not follow a simple adherence to Vegard's law due to the decreasing valence of Yb.

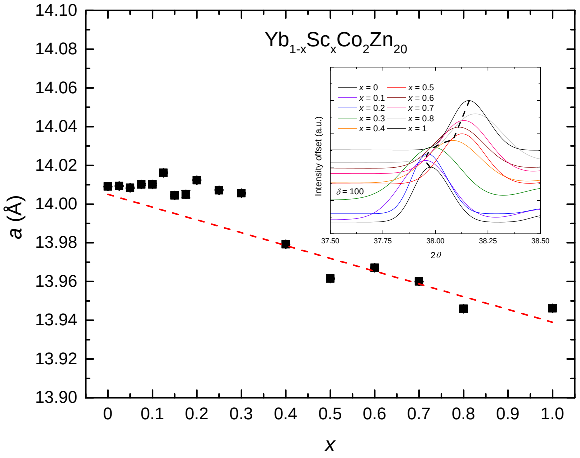

Figure 2.2. Lattice parameter a determined from Rietveld refinements on Yb_{1-x} $Sc_xCo_2Zn_{20}$, plotted vs. Sc concentration x. The dashed red line represents Vegard's law using published values of a from Torikachvili *et al.* for $x = 0$[1] and Nasch *et al.* for $x = 1$.[2] Our data show good agreement with previously published values for $x = 0$ and agreement in the range $0.4 \leq x \leq 1$ with limited scatter. The systematic behavior of the (531) diffraction peak is shown in the inset of the figure. The dashed line is a guide to the eye.

2.3.2 Magnetization

Magnetization divided by magnetic field, M/H, is displayed as a function of temperature T in Fig. 2.3. The measurements were performed in an applied magnetic field of $\mu_0 H = 0.5$ T for the samples with higher Yb concentrations. Since the magnitude of M/H decreases with Sc concentration, measurements were performed in magnetic fields $\mu_0 H = 1$ T for the samples with higher Sc concentrations. Almost no magnetic anisotropy is observed in the temperature-dependence of the magnetization data in the entire temperature range from 1.8 to 300 K.[33] For this reason, magnetization measurements were performed on random directions for $Yb_{1-x}Sc_xCo_2Zn_{20}$ single crystals. Temperature-dependent data for M/H are described well by a Curie-Weiss law in Eq.2.1 (where $C = \mu_{\text{eff}}^2 N_A/3k_B$, N_A is Avogadro's number, and k_B is Boltzmann's constant) with

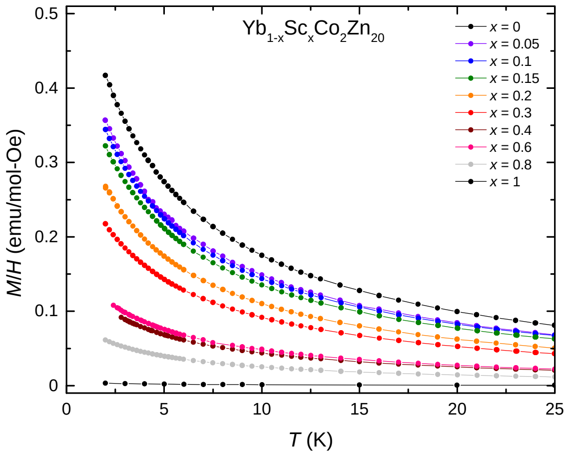

Figure 2.3. M/H vs. T, measured in an applied magnetic field of $\mu_0 H = 1$ T for samples with higher Sc concentrations and 0.5 T for samples with higher Yb concentrations.

no apparent magnetic ordering down to 2 K.

$$M/H = C/(T - \theta_{\mathrm{CW}}) + \chi_0, \tag{2.1}$$

We extracted the effective magnetic moment, μ_{eff}, from the Curie constant C. The values of μ_{eff} are reduced with respect to the Hund's rule value for the Yb^{3+} (μ = 4.54 μ_B) free ion as shown in Fig. 2.4(a). This result suggests that the Yb ions in this compound assume an intermediate valence. Values of the Curie-Weiss temperature, θ_{CW}, and temperature-independent magnetic susceptibility, χ_0, vs. x are also presented in Fig. 2.4.

2.3.3 EDX

In order to verify the magnetic properties of the $Yb_{1-x}Sc_xCo_2Zn_{20}$ single crystals described in the prior section, EDX measurements were performed on the same crystals used for magnetization measurements in order to determine the concentration of Sc, x_{EDX}. Data were collected on the atomic ratio of Yb to Sc from multiple EDX measurements on

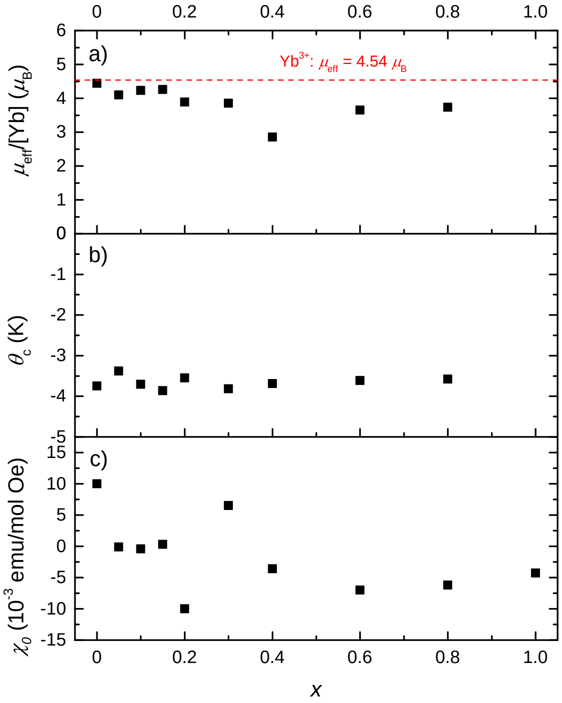

Figure 2.4. Plots of obtained values from the fitting of the Curie-Weiss law (Eq. 2.1) to the M/H data, as a function of x: a) effective magnetic moment per Yb ion, μ_{eff}/[Yb], with the dashed line as a guide to the eye to indicate the theoretical free ion moment of 4.54 μ_{B} for Yb^{3+} b) Curie-Weiss temperature, θ_c, and c) the temperature-independent susceptibility, χ_0.

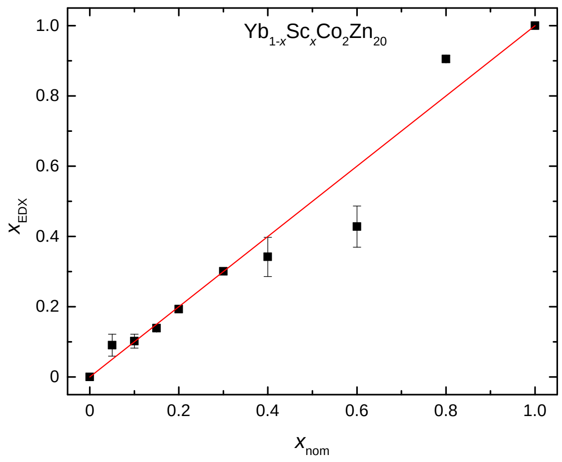

Figure 2.5. Measured Sc concentration, x_{EDX}, vs. nominal Sc concentration, x_{nom}, for single crystals used in the magnetization measurements. Values of x_{EDX} and x_{nom} are in good agreement, with moderate scatter in the range $0.4 \leq x_{\mathrm{nom}} \leq 0.8$. The red line drawn through $x_{\mathrm{EDX}} = x_{\mathrm{nom}}$ is a guide to the eye.

the surface of the single crystals and averaged to provide a reasonable estimate of x_{EDX}, which is plotted vs. the nominally-substituted concentration of Sc, x_{nom}, in Fig. 2.5. For each sample, x_{EDX} was calculated using the equation:

$$x_{\mathrm{EDX}} = \frac{[\mathrm{Sc}]_{\mathrm{EDX}}}{[\mathrm{Sc}]_{\mathrm{EDX}} + [\mathrm{Yb}]_{\mathrm{EDX}}} \tag{2.2}$$

Significant inhomogeneities in $[\mathrm{Sc}]_{\mathrm{EDX}}$ and $[\mathrm{Yb}]_{\mathrm{EDX}}$ were observed in the concentration range $0.4 \leq x \leq 0.8$. Since EDX measurements can only collect data on the surface, which is shown to vary significantly, it is difficult to make conclusions on x_{EDX} for the bulk single crystals which were analyzed through magnetization measurements. In the later discussion of valence fluctuations of Yb in this manuscript, where we use μ_{eff}/[Yb] data to calculate the valence of Yb, we use x_{EDX} instead of x_{nom}.

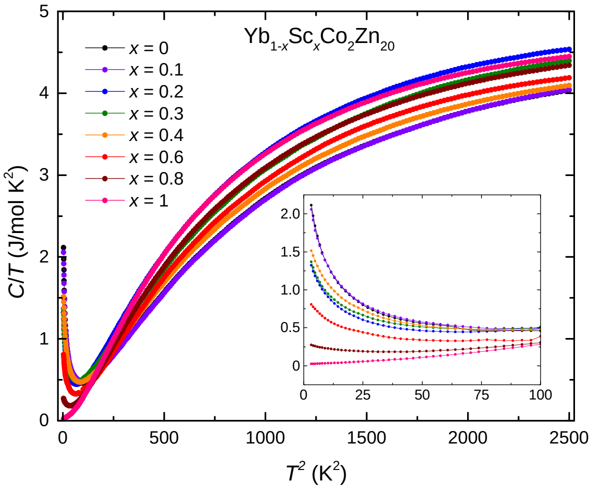

Figure 2.6. Specific heat divided by temperature, C/T, vs. T^2 for selected x of Yb$_{1-x}$Sc$_x$Co$_2$Zn$_{20}$. Shown in the inset is a zoomed-in plot of C/T vs. T^2 where low-temperature upturn in $C(T)/T$ is reminiscent of the Kondo effect. The C/T vs. T^2 data are linear in the temperature range $10K \lesssim T \lesssim 20$ K, consistent with the Debye approximation with a Debye temperature $\theta_D \approx 80$ K.

2.3.4 Specific Heat

Specific heat divided by temperature, C/T, of Yb$_{1-x}$Sc$_x$Co$_2$Zn$_{20}$ is plotted vs. T^2 in Fig. 2.6. Consistent with the specific heat measurements on YbCo$_2$Zn$_{20}$ by Torikachvili *et al.*,[1] a low-temperature upturn is observed in $C(T)/T$. High-temperature behavior of C/T appears to be consistent across all x; however, at low T, the magnitude of the upturn is shown to change with x. The electronic and phonon contributions to the specific heat as well as other characterizations are discussed later in the manuscript.

2.3.5 Electrical Resistivity

Measurements of $\rho(T)$ were performed on the Yb$_{1-x}$Sc$_x$Co$_2$Zn$_{20}$ system for selected samples and the data are displayed in Fig. 2.7. A sharp upturn in $\rho(T)$ as $T \to 0$ K is observed in samples with low values of x. This upturn, which has a nearly logarithmic behavior in T, is reminiscent of single-ion Kondo-like scattering of elec-

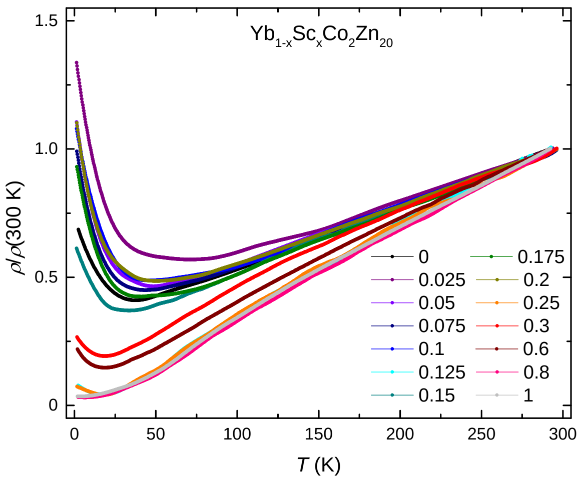

Figure 2.7. Electrical resistivity normalized to its value at 300 K, $\rho(T)/\rho(300\text{ K})$, vs. temperature for $\mathrm{Yb}_{1-x}\mathrm{Sc}_x\mathrm{Co}_2\mathrm{Zn}_{20}$ with various values of x.

trons by the magnetic moment of Yb ions that act as magnetic impurities. To further evaluate the Kondo contribution to the electrical resistivity from localized $4f$-electrons in $\mathrm{Yb}_{1-x}\mathrm{Sc}_x\mathrm{Co}_2\mathrm{Zn}_{20}$, ρ_{Kondo}, the electron-phonon scattering component has been subtracted using $\rho(T)$ data for the $\mathrm{ScCo}_2\mathrm{Zn}_{20}$ reference compound which does not contain $4f$-electrons. This component of ρ is described by

$$\rho_{\mathrm{Kondo}} = \rho - \rho_{\mathrm{ScCo_2Zn_{20}}} \equiv -A\ln(T/\mu), \tag{2.3}$$

where A represents the strength of the Kondo contribution to the resistivity and is proportional to the concentration of magnetic impurities.[3] The resistivity attributed to the Kondo effect, $\rho_{\mathrm{Kondo}}(T)$, is vs. T in Fig. 2.8, and vs. $\log T$ in the inset of Fig. 2.8. The linear portion of the resistivity on the semi-log plot is consistent with the predictions of the Kondo effect for $T >> T_K$, where T_K is the Kondo temperature.[3,4]

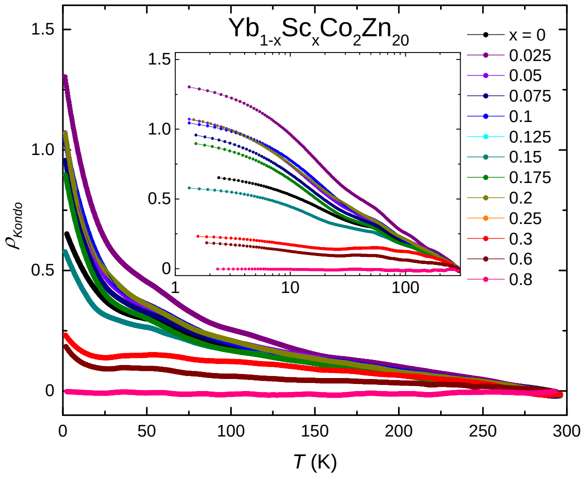

Figure 2.8. Electrical resistivity normalized to its value at 300 K, for the resistivity of the nonmagnetic $ScCo_2Zn_{20}$, ρ_{Kondo}, vs. T. A significant, low-temperature logarithmic upturn is observed in correlation with the Yb concentration, consistent with the Kondo effect. (Inset) ρ_{Kondo} vs. log T showing linear behavior in accord with the predictions of the Kondo effect for $T >> T_K$, where T_K is the Kondo temperature.[3,4]

2.4 Discussion

2.4.1 Yb valence

The valence of Yb, v_{Yb}, was calculated from the lattice parameter, a, obtained through Rietveld refinement of XRD data,[32] and the effective magnetic moment, μ_{eff}, was extracted from the fits of a Curie-Weiss law (Eq. 3.2) to the magnetic susceptibility data.

Calculating Yb valence from XRD measurements

Vegard's law was employed to estimate v_{Yb}.[34] In the Vegard's law analysis, the lanthanide sites in $Ln\mathrm{Co_2Zn_{20}}$ are occupied by lanthanide ions according to their nominal concentrations, and the deviations of the lattice parameters from Vegard's law can be used to estimate the valence of the lanthanide ions.[35,36]

The lattice parameter, a, of $Yb_{1-x}Sc_xCo_2Zn_{20}$ should follow Vegard's law between the Yb and Sc end-member compounds and decrease linearly with increasing Sc concentration, according to Eq. 2.4, if the valence of Yb and Sc do not change. Because Vegard's law is simply a linear relationship representing the weighted average, we can even introduce a third term to represent a for Yb^{2+}.

$$a(x) = (1-x)a_{Yb^{3+}} + xa_{Sc} \tag{2.4}$$

Since $a_{\mathrm{Yb}^{2+}}$ for the hypothetical $\mathrm{Yb}^{2+}\mathrm{Co}_2\mathrm{Zn}_{20}$ is unknown, the following method was used to estimate its value. We make use of work by Jia *et al.*[5] which relates the lattice parameter for various trivalent lanthanides in the system $Ln^{3+}\mathrm{Co}_2\mathrm{Zn}_{20}$ to the known ionic radii, r_{ion}, for a lattice coordination number (CN) of 9, taken from Ref. 37. A linear extrapolation of the lattice parameter vs. ionic radius was used to estimate a for $\mathrm{Yb}^{2+}\mathrm{Co}_2\mathrm{Zn}_{20}$. The final step to determine $a_{\mathrm{Yb}^{2+}}$ is to find an ionic radius for Yb^{2+} with CN = 9. This value was not available in Ref. 37. Instead, using established examples of the ratios of ionic radii between Yb^{3+} and Yb^{2+} for various CNs < 9, an estimation can be made, yielding $r_{\mathrm{ion}} \approx 1.20$ pm for Yb^{2+} with CN = 9. Using this value, $a_{\mathrm{Yb}^{2+}} = 14.14$ Å is calculated from the lanthanide contraction shown by Jia *et al.*[5] which is displayed in Fig. 2.9 along with the extrapolation of $a_{Ln\mathrm{Co}_2\mathrm{Zn}_{20}}$ vs. Ln ionic radius through other selected Ln^{2+}.

With a known for the 3 potential occupants of the Yb site in $\mathrm{Yb}_{1-x}\mathrm{Sc}_x\mathrm{Co}_2\mathrm{Zn}_{20}$, ($\mathrm{Yb}^{3+}$, Yb^{2+}, or $\mathrm{Sc}^{(3+)}$), Vegard's law can be constructed according to the following relation:

$$a(x) = (1-x)[(v_{\mathrm{Yb}}-2)a_{Yb^{3+}} + (3-v_{\mathrm{Yb}})a_{Yb^{2+}}] + xa_{Sc} \tag{2.5}$$

where $a(x)$ is calculated from Rietveld refinement[32] of the XRD data, x is the nominal concentration of Sc, and the lattice parameters for Yb^{3+} and Sc which are in good agreement with published literature values for $\mathrm{YbCo}_2\mathrm{Zn}_{20}$[1] and $\mathrm{ScCo}_2\mathrm{Zn}_{20}$[2]. The lattice

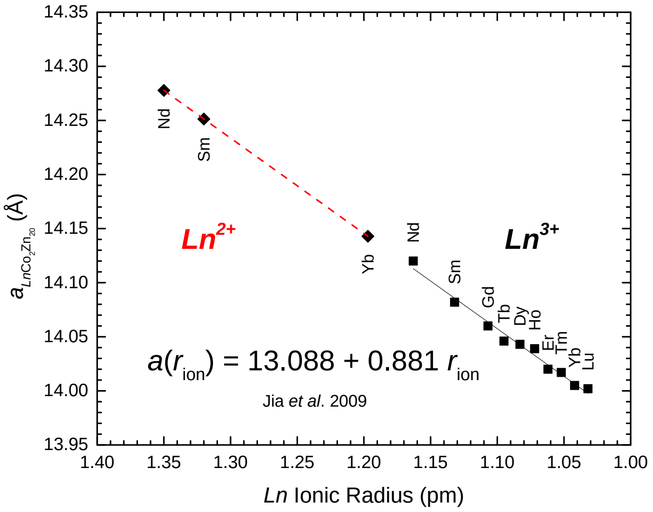

Figure 2.9. Lattice parameter *a* for *Ln*Co_2Zn_{20} vs. *Ln* ionic radius (CN = 9), based on the work of Jia *et al.*[5]

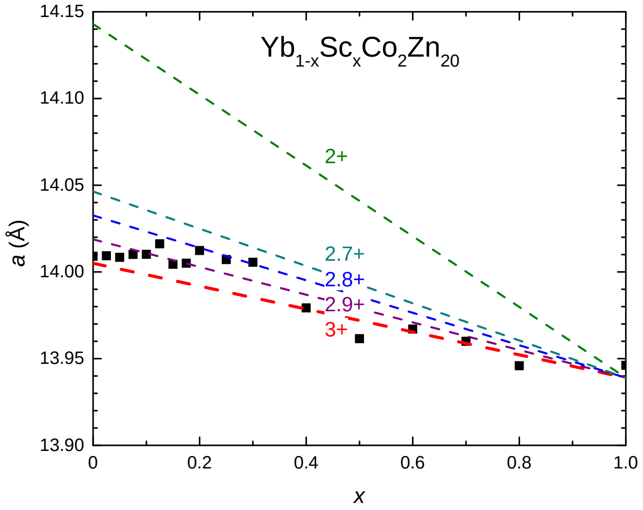

Figure 2.10. Using the approximation for *a* of $Yb^{2+}Co_2Zn_{20}$ from Fig. 2.9, the valence of Yb, $v_{Yb}(x)$, can be calculated in $Yb_{1-x}Sc_xCo_2Zn_{20}$ by looking at the weighted average of *a* between Yb^{3+} and Yb^{2+} as it falls in accordance with Vegard's law.

parameter for Yb^{2+} is established in the prior discussion along with the extrapolation demonstrated in Fig. 2.9. With all these known parameters, the resulting unknown in Eq. 2.5 is v_{Yb} which can now be calculated as a function of the lattice parameter. The amount of deviation from Vegard's law between just Yb^{3+} and Sc represents the closer the valence is to 2+. Fig. 2.10 demonstrates Vegard's law being traced out for the lattice parameter from the parent $\mathrm{ScCo_2Zn_{20}}$ at $x = 1$ back to Yb^{3+} and Yb^{2+}, as well as a few intermediate valences which are simply weighted averages of the two integer valence states. The valence of Yb at a particular value of x is determined by the Vegard's law linear relation between $a_{\mathrm{Yb}^{v+}}$ and $a_{\mathrm{Sc}^{3+}}$ that passes through the value of a at x.

Estimation of Yb valence from mangetization measurements

Values of the effective magnetic moment, μ_{eff}, per Yb ion, calculated from fits of a Curie-Weiss law to data in Fig. 2.3, are plotted in Fig. 2.4 and can be used to estimate the valence of Yb. A similar analysis was performed for Yb in the $\mathrm{Ce}_{1-x}\mathrm{Yb}_x\mathrm{RhIn}_5$ system by Jang *et al.* (2018).[38] Since μ_{eff}^2 can be calculated as the weighted average of the squared magnetic moment of each potential occupant of the site R in $R\mathrm{Co_2Zn_{20}}$, and both Sc and Yb^{2+} are non-magnetic, the following equation can be used:

$$\mu_{\mathrm{eff}}^2 = (v_{\mathrm{Yb}} - 2)(1-x)\mu_{\mathrm{Yb}^{3+}}^2 \tag{2.6}$$

With $\mu_{\mathrm{Yb}^{3+}} = 4.54\ \mu_B$, the calculated $\mu_{\mathrm{eff}}(x)$ can be used to directly calculate v_{Yb} which should lie between 2 to 3. Since the Sc concentration was analyzed for the single crystals whose magnetization measurements were performed, we use x_{EDX} in the analysis in an attempt to correct for any deviations in $\mu_{\mathrm{eff}}(x)$ from their expected values. Significant deviations of the valence calculations on μ_{eff}^2 data from the $a(x)$ data may therefore be attributed to the fact that EDX can only measure the Sc concentration, x, on the surface, which may be different from x of the bulk sample since inhomogeneities in x are common in flux-grown single crystals.

Yb valence results

From the calculations detailed above, we plot v_{Yb} data from XRD and magnetization measurements as a function of Sc concentration, x_{nom} for XRD (red), and x_{EDX} for magnetization (black) for $\mathrm{Yb}_{1-x}\mathrm{Sc}_x\mathrm{Co}_2\mathrm{Zn}_{20}$ in Fig. 2.11. For $x \leq 0.3$, the Yb valence calculated from the lattice parameters and μ_{eff} show almost identical behavior where v_{Yb} linearly decreases from 3+ at $x = 0$ to ≈ 2.8+ at $x = 0.3$. The calculated valence values show discrepancies for $x > 0.3$, where the values for the actual and nominal concentrations of Sc deviate from each other. Calculated v_{Yb} from XRD data show scatter around 3+ for $x > 0.3$ which is reasonable due to Sc being trivalent.

In contrast, magnetization measurements show significant scatter of the Yb valence at $x \geq 0.4$, but this may be from the inhomogeneity of Sc concentration in the single crystals or due to large errors in the measured magnetization at lower Yb concentration, since the magnetization signal is significantly weaker for the concentrations near $x = 0$, as well as the calculations for magnetic moment being potentially influenced by the negative magnetization background measured in the end-member compound $\mathrm{ScCo}_2\mathrm{Zn}_{20}$.

Despite these discrepancies at higher x, the $\mathrm{Yb}_{1-x}\mathrm{Sc}_x\mathrm{Co}_2\mathrm{Zn}_{20}$ system appears to show a robust change in the valence of Yb, which is not surprising given the reported behavior of Yb in other correlated electron systems such as $\mathrm{Ce}_{1-x}\mathrm{Yb}_x\mathrm{CoIn}_5$[39] and $\mathrm{Ce}_{1-x}\mathrm{Yb}_x\mathrm{RhIn}_5$[38] where in both cases Ce remains trivalent, much like Sc in $\mathrm{Yb}_{1-x}\mathrm{Sc}_x\mathrm{Co}_2\mathrm{Zn}_{20}$. One difference is that for the aforementioned “1-1-5” system, Yb is being substituted for Ce and, as a result, has its valence reduced, whereas in $\mathrm{Yb}_{1-x}\mathrm{Sc}_x\mathrm{Co}_2\mathrm{Zn}_{20}$, Sc is being substituted for Yb whose valence is reduced. These substitution effects on the Yb valence appear to be opposite, in some regards, perhaps either due to the fact that Sc has a smaller ionic radius than Yb whereas the radius for

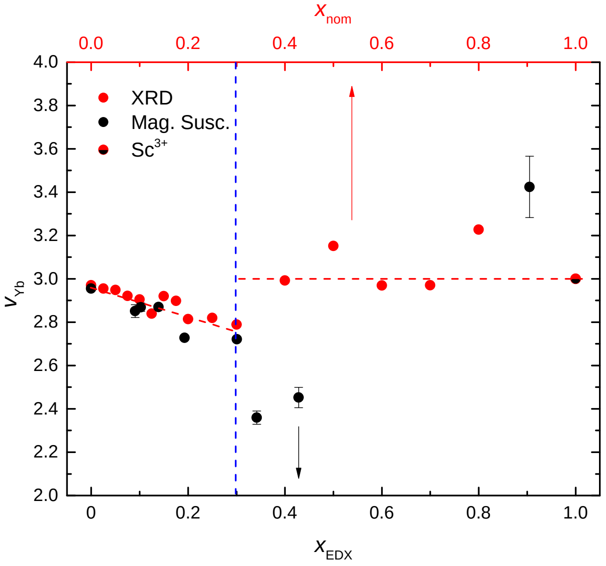

Figure 2.11. Values of Yb valence, v_{Yb}, which were independently calculated from XRD and magnetization measurements, are plotted as a function of Sc concentration, x_{nom} for XRD (red), and x_{EDX} for magnetization (black). For $x \leq 0.3$, both sets of valence calculations show good agreement, indicating a decrease in valence from $v_{\mathrm{Yb}} = 3+$ down to $\approx 2.8+$. Valence data from XRD measurements show scatter around 3+ for $x > 0.3$. In this concentration range, valence data calculated from M/H show significant scatter due to likely possible inhomogeneities in the single crystals, as measured by EDX. Another potential explanation is since Yb is the main contributor to the observed phenomena, samples in the Sc-rich region will have larger errors in the Yb concentration, yielding larger deviations from expected behavior of the data.

Ce is larger or because Sc is non-magnetic while Ce is very magnetic, or very likely it is a combination of both of these factors. Further analysis using techniques such as x-ray absorption spectroscopy (XAS) may allow independent measurement of the Yb valence.

2.4.2 Kondo Effect in $Yb_{1-x}Sc_xCo_2Zn_{20}$

Kondo behavior in the electrical resistivity

The Kondo contribution to the electrical resistivity from localized Yb 4f-electron states in the $Yb_{1-x}Sc_xCo_2Zn_{20}$ system is characterized using Eq. 2.3.[3] The extracted parameters A (black), $A/[\mathrm{Yb}]$ (blue), and T_{min}, are presented as a function of Sc concen-

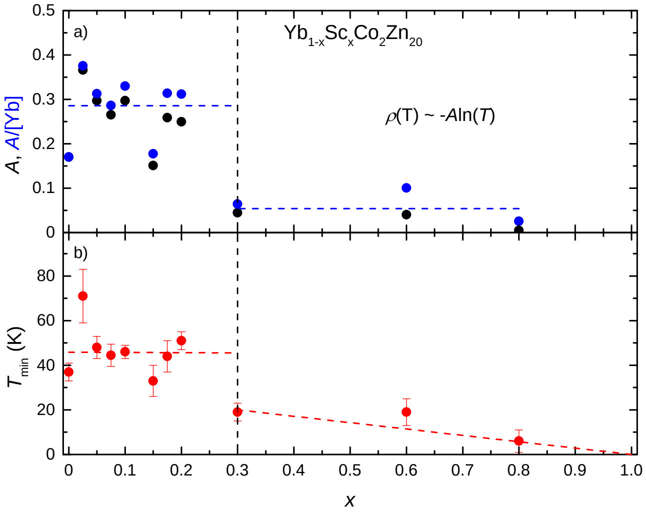

Figure 2.12. Parameters extracted from fitting the Kondo equation to the resistivity from Fig. 2.8: a) A, the strength of the Kondo scattering in black ($A/[\mathrm{Yb}]$ in blue), and b) T_{min}, the temperature of the resistivity minimum, are plotted against Sc concentration x.

tration x in Fig. 2.12 to observe how the Kondo effect changes as Yb is systematically replaced by Sc. A/[Yb] is fairly large and robust at high Yb concentrations in the range $0 \leq x \leq 0.3$, which is consistent with theory for a Kondo system. However, at $x = 0.3$, the same concentration where there appears to be a shift in change in the behavior of the Yb valence, there is a precipitous drop in A/[Yb] to much lower values, which reflects a very weak Kondo-like contribution in the range $0.3 < x \leq 1$. In this region, Yb is observed to have a constant valence of 3+. Because of this stable valence, the region $0.3 < x \leq 1$ may more accurately represent a magnetically dilute regime. The range $0 \leq x \leq 0.3$ may be more reflective of strong correlations between the Yb ions, due to the co-existence of a robust Kondo-like behavior and an apparently changing Yb valence.

Resonance level model in specific heat

We attempt to characterize $Yb_{1-x}Sc_xCo_2Zn_{20}$ using measurements on $C(T)/T$ from Fig. 2.6 by fitting the resonance level model (RLM) for the Kondo effect derived by Schotte and Schotte.[14] The low-temperature upturns were fit well by the equation described in Ref. 14 for $x \leq 0.6$, in addition to a fit for the phonon contribution to C/T of βT^2, up to $T = 25$ K. We used values of β to calculate the the characteristic Debye temperature, Θ_D using the relation

$$\beta = \frac{12\pi^4 N_A k_B}{5\Theta_D^3}. \tag{2.7}$$

Calculated values for Θ_D are plotted in Fig. 2.14(a). The RLM fits, shown in Fig. 2.13, yielded two useful parameters in describing the behavior of $\mathrm{Yb_{1-x}Sc_xCo_2Zn_{20}}$. An approximation for the Kondo temperature, T_K, was extracted from the RLM fit and plotted in Fig. 2.14(b). T_K appears to increase with x and saturate at $T_\mathrm{K} \approx 5$ K before dropping back to 0 in the region where the RLM fails to accurately describe the system. The parameter for the effective angular momentum, J, was also extracted from the fit, and is shown to decrease monotonically from $J \approx 3$ for $x = 0$ down to near $J = 0$ at $x = 1$, where the RLM fails to properly fit the data. Angular momentum per Yb ion, $J/[\mathrm{Yb}]$ was also plotted and may show behavior consistent with changes in the Yb valence near $x = 0.3$, however it is difficult to distinguish between abrupt changes in J and the quality of the RLM fit. It is possible that there is a correlation between $J/[\mathrm{Yb}]$ and the calculated valence of Yb, v_Yb. The Hund's rule ground state for Yb would suggest a value of $J = 7/2$, which is close to the calculated value of $J/[\mathrm{Yb}] \approx 3$ from the RLM fit for $0 \leq x < 0.2$. For concentrations $0.2 \leq x < 0.6$, we observe intermediate valence behavior for Yb which may explain the behhavior of J in this range, dropping near $J/[\mathrm{Yb}] = 1$ before slowly climbing up to ≈ 2.8. In the region where the RLM fit fails to accurately describe C, $0.6 \leq x \leq 1$, J converges to 0. From this model, it appears there is some relationship between the valence of Yb and the angular momentum in the ground state J.

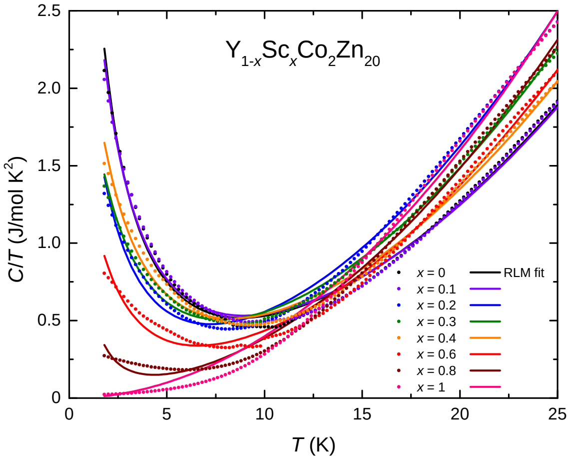

Figure 2.13. Fits of the RLM to C/T in the range $0 \leq T \leq 25$ K. Good agreement between the RLM and the measured C/T data for concentrations $0 \leq x \leq 0.4$. For $x \geq 0.6$, the RLM fails to accurately describe the C/T data due to the decreasing presence of the Kondo effect.

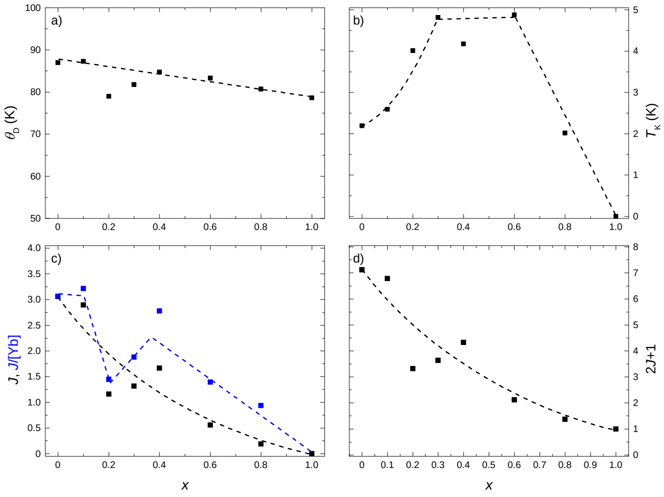

Figure 2.14. a) Debye temperature, θ_D, calculated from the fitted phonon contribution to C/T, βT^2, using Eq. 2.7, b) calculated Kondo temperature, T_K using fitting of C/T to the RLM, c) angular momentum of $Yb_{1-x}Sc_xCo_2Zn_{20}$, J, in black and J per Yb, $J/[Yb]$, in blue and d) $2J+1$ representing the ground state degeneracy.

2.5 Concluding Remarks

The initial goal of studying $\mathrm{Yb}_{1-x}\mathrm{Sc}_x\mathrm{Co}_2\mathrm{Zn}_{20}$ was to observe the effects of "chemical pressure" induced by Sc-substitution on a Yb-based heavy fermion system where the two components (γ, A) of the Kadowaki-Woods ratio were abnormally high, suggesting a heavy fermion mass well beyond typical values for Yb-based 1-2-20s.[1] $\mathrm{YbCo}_2\mathrm{Zn}_{20}$ also showed a very robust single-ion Kondo-like logarithmic behavior at low T. The applied pressure effects on this Yb parent compound have also been previously studied, showing magnetic ordering and development of non-Fermi liquid behavior in the resistivity.[13] The presence of these phenomena suggest that pressure can induce a QCP in a system which tends to hybridize, providing valuable insight into one of the few Yb-based $4f$-electron systems. Were Sc-substitution to provide similar effects, one could observe an array of interesting phenomena at ambient pressure, allowing for even more challenging measurements into the system allowing us to gain valuable information on this class of Yb-based heavy fermion systems. However, subverting our expectations was a more interesting observation in that Sc-substitution in the Yb-rich regime did not appear to induce any pressure, but instead resulted in a fairly robust lattice volume as a function of x. The behavior of $a(x)$, along with $\mu_{\mathrm{eff}}(x)$/[Yb], shows that the Yb valence actually decreases linearly with x from 3+ at $x = 0$ to 2.8+ at $x = 0.3$.

In a system where the Yb valence is expected to be stable, as applied pressure tends to do with valence-fluctuating lanthanides, the decrease in unit cell volume with x in the $\mathrm{Yb}_{1-x}\mathrm{Sc}_x\mathrm{Co}_2\mathrm{Zn}_{20}$ system results in a decreasing of the Yb valence. Only when the Yb substitution is significantly diluted by non-magnetic Sc in the region $0.3 < x \leq 1$, does Yb appear to return to its trivalent state. In addition to this unexpected behavior, we observe that the Kondo contribution to $\rho(T)$ depends on the Yb concentration. According to the Kondo impurity model, this Kondo contribution to $\rho(T)$ should be a linear function of Yb ocncentration.[3] However, two regimes, correlated with the Yb valence, are observed; the Kondo contribution to $\rho(T)$ is large and stable for $0 \leq x \leq 0.3$, but then drops abruptly by $\sim 90\%$ in the Sc-rich region $0.3 < x \leq 1$. This, along with characterization of $C(T)$ according to the RLM which yields fitting parameters of T_K and J, suggests there is a strong link between the behavior of the Yb valence and the nature of the Kondo effect in this compound. The $Yb_{1-x}Sc_xCo_2Zn_{20}$ system provides an unexpected intersection of a variety of fascinating phenomena found in correlated $f-$electron systems and can be a subject of great interest for future investigations using more advanced measurement techniques.

Though valence fluctuations appear to be present in Yb for $0 \leq x \leq 0.3$, according to measurements of a and $M(T)$, further measurements are useful to confirm the behavior of the valence such as x-ray absorption near edge structure (XANES). XANES measurements can characterize the valence of Yb by looking at the Yb L_{III} edges and the relative step heights at energies corresponding to both Yb^{2+} and Yb^{3+}. The ratio of Yb^{2+} to Yb^{3+} is derived from Yb L_{III} edges. This method was used to estimate the valence of Yb in the correlated electron systems $Ce_{1-x}Yb_xCoIn_5$[40] and $Ce_{1-x}Yb_xRhIn_5$.[38]

Acknowledgements

Research at the University of California San Diego was supported by the U.S. Department of Energy, Office of Basic Energy Sciences, Division of Material Science and Engineering under Award Grant No. DE-FG02-04-ER46105.

Chapter 2, in part is currently being prepared for submission for publication of the material. Pouse, N., Yazici, D., Friedman, A. J., Maple, M. B. The dissertation author was the primary investigator and author of this material.

Chapter 3

Tuning the magnetic ground state of $Ce_{1-x}Yb_xRhIn_5$ by Yb valence fluctuations

We characterize the properties of $Ce_{1-x}Yb_xRhIn_5$ single crystals with $0 \leq x \leq 1$ using measurements of powder x-ray diffraction (XRD), energy dispersive x-ray spectroscopy (EDS), electrical resistivity, magnetic susceptibility, specific heat, x-ray absorption near edge structure (XANES), and neutron diffraction. The Yb valence, v_{Yb}, calculated from the magnetic susceptibility and measured using XANES, decreases from 3+ at $x = 0$ to $\sim$2.1+ at $x_{act} = 0.2$, where x_{act} is the measured Yb concentration. A transition from incommensurate to commensurate antiferromagnetism (AFM) is observed in neutron diffraction measurements along Q = (0.5, 0.5, l) between $0.2 \leq x_{act} \leq 0.27$; this narrative is supported by specific heat measurements in which a second robust feature appears at a temperature T_I ($T_I < T_N$) for the same concentration range. Magnetic susceptibility measurements also reveal features which provide additional evidence of magnetic ordering. The results of this study suggest that the evolution of the Yb valence plays a critical role in tuning the magnetic ground state of $Ce_{1-x}Yb_xRhIn_5$.

3.1 Introduction

Numerous studies on Ce-based heavy fermion compounds, notably the CeMIn$_5$ (M = Co, Rh, Ir) family of compounds, have demonstrated the crucial role played by $4f$ electrons in unconventional superconductivity (SC), magnetic order, quantum criticality, and valence fluctuations.[41,42,43,44] The compound CeRhIn$_5$ is an ideal system in which to study the coexistence between magnetism and SC. Its temperature−pressure ($T-P$) phase diagram shows antiferromagnetic (AFM) ordering below a Néel temperature $T_N = 3.8$ K at ambient pressure, with T_N being suppressed to a quantum critical point as pressure is applied at a critical pressure $P_c = 2.25$ GPa. Near P_c, a broad dome of unconventional superconductivity with a maximum superconducting critical temperature of $T_c = 2.2$ K is found. The compound CeRhIn$_5$ is a relatively rare case in which the characteristic temperatures T_N and T_c are of the same magnitude, indicating a robust competition between antiferromagnetism and superconductivity.[45,46,47,48,49]

Neutron diffraction experiments on CeRhIn$_5$ in zero applied magnetic field revealed that the antiferromagnetic ground state consists of antiferromagnetically-coupled spin spirals that propagate along the c-axis as characterized by propagation vector q_M = (0.5, 0.5, 0.297) in terms of the reciprocal lattice $2\pi/a$, $2\pi/b$, $2\pi/c$ [r.l.u.] and with Ce ion magnetic moments that reside within the tetragonal basal plane.[46,50] Neutron spectroscopy further demonstrated that this complex spiral ground state is a consequence of frustrated nearest and next-nearest neighbor exchange interactions along the c axis.[51] A spin-flop transition is observed when an external magnetic field of $\mu_0 H = 2$ T is applied within the ab-plane.[52,46]. Here the magnetic field induces a surprisingly large easy-axis magnetic anisotropy that together with frustrated exchange interactions results in a rich low magnetic field phase diagram that can be explained by a model related to the Axial Next-Nearest-Neighbor Ising (ANNNI) model.[53] At low temperatures $T < T_1$

the field-induced easy-axis anisotropy results in a commensurate, "+ + − −" magnetic structure, where the magnetic moments lying in the *ab*-plane follow an up-up-down-down periodicity along the *c*-axis.[46,53] A third, incommensurate magnetic phase is observed in the region $T_1 < T < T_N$, where the effect of the anisotropy is softened due to magnetic fluctuations arising near T_N. This results in an elliptical spin spiral with modulated magnetic moments that are predominately oriented along the easy axis but exhibit small components perpendicular to it.[46] In agreement with the ANNNI, model the propagation vector of the elliptical phase is strongly temperature dependent.[53] A study at higher magnetic fields uncovered evidence for nematic ordering similar to what is observed in iron-based superconductors.[54] These recent studies suggest that the magnetic order in $CeRhIn_5$ is highly tunable and here we explore this in more detail by means of Yb substitution on the Ce site.

The striking effects of Yb substitution on the physical properties of the heavy-fermion superconductor $CeCoIn_5$, which have been reported in detail,[55,28,56,57,58] motivated us to study the related system $Ce_{1-x}Yb_xRhIn_5$. One interesting materials science issue encountered in the $Ce_{1-x}Yb_xCoIn_5$ system is the discrepancy between the nominal Yb concentration, x_{nom}, and the actual Yb concentration, x_{act}, of the flux-grown single crystals; this issue is discussed in Refs. 59,40. While the Ce valence remains stable at 3+ for all x in the $Ce_{1-x}Yb_xCoIn_5$ system, the Yb valence decreases from 3+ to 2.3+ near $x_{nom} = 0.2$.[39] At the critical concentration of $x_{nom} = 0.2$ where the Yb valence stabilizes, various unusual phenomena emerge. At this Yb concentration, the Fermi surface undergoes a reconstruction[60] and the quantum critical field, H_{QCP}, is suppressed.[61] There is also evidence from London penetration depth measurements that the nodal superconducting energy gap of $CeCoIn_5$ crosses over to a nodeless gap at this Yb concentration;[62] on the other hand, recent thermal conductivity measurements are consistent with a robust nodal superconducting energy gap for all Yb concentrations.[63] Identifying the symmetry of the superconducting order parameter remains an interesting and unresolved issue in the system $Ce_{1-x}Yb_xCoIn_5$.

In this manuscript, we report the results of powder x-ray diffraction, energy dispersive x-ray spectroscopy, electrical resistivity, magnetization, specific heat, and neutron diffraction measurements on the $Ce_{1-x}Yb_xRhIn_5$ system; these measurements reveal many similarities with the $Ce_{1-x}Yb_xCoIn_5$ system. The unit cell volume vs. x exhibits an analogous deviation from Vegard's law, demonstrating a discrepancy between Yb concentrations x_{act} and x_{nom}. The Yb valence, which is determined through multiple experimental techniques, is found to change from 3+ to 2.1+ near $x_{act} \approx 0.2$. Neutron diffraction measurements show that there is also a crossover from an incommensurate to a commensurate magnetic structure near this Yb concentration. Furthermore, a second feature, presumably of magnetic origin, emerges in specific heat measurements for samples with $x_{act} \geq 0.18$. These and other observations hint at a potential relationship between the magnetic ground state in $Ce_{1-x}Yb_xRhIn_5$ and the valence of Yb. Since the discrepancy in Yb concentration of $Ce_{1-x}Yb_xRhIn_5$ single crystals is qualitatively identical to that of $Ce_{1-x}Yb_xCoIn_5$ and thoroughly explained in the paper of Jang *et al.*,[40] all of the references to Yb concentration x in the present manuscript represent the actual Yb concentration ($x = x_{act}$).

3.2 Experimental Details

Single crystalline samples of $Ce_{1-x}Yb_xRhIn_5$ were grown using a molten indium flux method.[64] For concentrations $x_{\mathrm{nom}} > 0.9$, heat treatment at significantly higher temperature ($T > 1300$ °C) is required with the elements sealed in a metallic crucible, such as a Ta or Mo tube, as opposed to quartz in order to successfully grow the crystals.[65] Since our lab did not have access to these temperatures or metallic crucibles, we attempted to grow these Yb-rich compounds with $T < 1200$ °C in a quartz crucible. This resulted in an inability to form high quality single crystals with $0.28 \leq x_{\mathrm{act}} \leq 1$. Additionally, the reported discrepancies in the Yb concentration could be attributed to this difficulty in synthesizing crystals with higher Yb concentrations due to the lower than ideal melting temperatures in conjunction with the potential for the Yb to react with the excess In to form the binary compound $\mathrm{YbIn_3}$. For these reasons, we were unable to perform reliable measurements, including neutron scattering, on single crystals of $\mathrm{Ce_{1-x}Yb_xRhIn_5}$ for $0.28 \leq x_{\mathrm{act}} \leq 1$. Polycrystalline ingots of $\mathrm{Ce_{1-x}Yb_xRhIn_5}$ were formed using traditional arc-melting techniques for selected Yb concentrations. X-ray diffraction (XRD) measurements were performed on powdered single crystals in a Bruker D8 Discover x-ray powder diffractometer using a Cu-K_α source to characterize the crystal structure. Analysis of chemical compositions was performed through transmission x-ray spectroscopy (TXAS) and energy dispersive x-ray spectroscopy (EDS) measurements, as described previously.[40]

Magnetic susceptibility measurements were performed between 300 and 2 K using a Magnetic Property Measurement System (MPMS) equipped with a 7 T superconducting magnet from Quantum Design (QD). Four-wire electrical resistivity measurements were performed from 300 K down to $\sim$ 1.1 K in a pumped ^{4}He Dewar. Specific heat measurements were performed down to 1.8 K in a QD Physical Property Measurement System (PPMS) DynaCool using a standard thermal relaxation technique. Extended x-ray absorption fine structure (EXAFS) measurements were collected on powdered samples at the SLAC National Accelerator Laboratory on beamline 4-1. Transmission spectroscopy measurements were performed on the Ce and Yb $\mathrm{L_{III}}$ edges and on the Rh K edge.

Neutron diffraction measurements were made on BT-4 and BT-7 triple-axis spectrometers at the NIST Center for Neutron Research (NCNR).[66] Single crystals were mounted in the *HHL* scattering plane and measured with neutrons of incident energy $E_i = 14.7$ meV ($\lambda = 2.359$ Å). Coarse collimations of open 80'-80'-120' or 40'-40'-40'-

open full-width-at half-maximum (FWHM) were used on BT-7 and BT-4, respectively, while 10’-10’-40’ and open-50’-40’-radial were used for the high-resolution diffraction with the position sensitive detector on BT-7. Measurements were performed either in a helium cryostat with a base temperature of 1.5 K, or a He^3 system with a base temperature of 0.3 K.

3.3 Results and Discussion

3.3.1 X-ray Diffraction

The crystal structure of $Ce_{1-x}Yb_xRhIn_5$ is tetragonal with space group $P4/mmm$ for all temperatures below 300 K and for all x values. Rietveld refinements were performed on several XRD patterns using GSAS[31] and EXPGUI[32]. In Fig. 3.1, the powder XRD pattern for a representative sample is shown. The Rietveld refinement is plotted in red and the measured XRD data are plotted as a black curve. We obtained good agreement between the measured XRD pattern and the refinement calculations for the expected crystal structure, which is quantified by reduced χ^2 values of less than 3 for most concentrations, but with some deviation when x is large. The inset of Fig. 3.1 illustrates the shift in Bragg-peak positions as x increases, indicating systematic changes in the lattice parameters. Using the Rietveld refinement technique, lattice parameters a and c were determined and are plotted along with the calculated unit-cell volume in Fig. 3.2.

Single crystals of $Ce_{1-x}Yb_xCoIn_5$, synthesized using an indium flux technique, are well-known to have a sub-nominal Yb concentration. As part of this study, we found that our $Ce_{1-x}Yb_xRhIn_5$ single crystals also contain a sub-nominal Yb concentration. To address this issue in the Rh system, we compare the results from XRD, EDS, TXAS, and neutron diffraction measurements in Fig. 3.2. The initial indication of the discrepancy

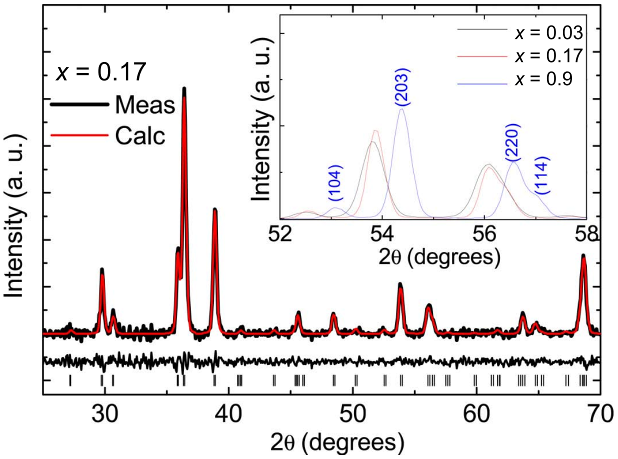

Figure 3.1. A representative XRD pattern for the $x = 0.17$ sample is plotted. The expected Bragg peak positions are indicated with small ticks above the labeled 2θ axis. The calculated fit from Rietveld refinement is plotted as the top (red) curve and the deviation from the fit is shown as the bottom (black) curve above the Bragg peak indicators. The inset illustrates differences in the XRD patterns for different Yb concentrations over a narrow window of 2θ. The peaks shift slightly between $x = 0.03$ and $x = 0.17$, and then shift significantly for $x = 0.9$.

between the nominal Yb concentration x_{nom} and the actual Yb concentration x_{act} comes from unit-cell volume data, where a deviation from Vegard's law is shown in Fig. 3.2(a). Since the valences of Ce and Yb are known to be constant from supporting measurements of XAFS and magnetic susceptibility for $x > 0.2$, the deviation from Vegard's law can be explained by a discrepancy between x_{act} and x_{nom}; this is resolved by shifting unit-cell volume data so that it coincides with the linear extrapolation of Vegard's law and defining the resulting x value as the actual concentration of Yb, x_{act}. When x_{act} is plotted as a function of x_{nom} in Fig. 3.2(b), we see a relationship between the two concentrations which can be represented by the equation $x_{act} = x_{nom}/3$ up to about $x_{nom} = 0.7$. There is a sharp deviation from this behavior over a narrow concentration range between $0.7 \leq x_{nom} \leq 0.85$ before Vegard's law ($x_{act} = x_{nom}$) is obeyed for $x_{nom} \geq 0.9$. The conclusions drawn from this application of Vegard's law are supported by EDS and TXAS measurements on the single crystals, which are also shown in Fig. 3.2(b). This scenario is qualitatively identical to that of the Co series, which is discussed in the paper of Jang *et al.*[40] We found that polycrystalline samples of $Ce_{1-x}Yb_xRhIn_5$, which were also studied using XRD and EDS measurements, show an agreement between x_{nom} and x_{act}; the discrepancy, therefore, appears to be limited by the solubility of Yb in Ce for the temperature range (Room temperature $\leq T \leq 1200$ °C) covered in our flux growth technique. With the relationship between actual and nominal concentrations of Yb being well-established, all mentions of Yb concentration x for $Ce_{1-x}Yb_xRhIn_5$ hereafter refer to the actual concentration of Yb ($x = x_{act}$) in this manuscript.

3.3.2 XANES

The step height in the absorption edge in transmission x-ray spectroscopy (TXAS) is a direct measurement of the number of atoms in the unfocused x-ray beam. Consequently, the ratio of the edge step heights for different elements in a sample, keeping the illuminated region of the sample the same for each edge energy, provides a measure of the relative concentrations. To get actual concentration ratios each edge step height must be divided by the absorption cross-sectional area for that element.[67] The absorption edge step height was determined by a simple linear construction technique above and below the edge. We have used this approach recently to determine concentration ratios in the $Ce_{1-x}Yb_xCoIn_5$ system.[40] and use a similar approach here. For such measurements, thin layers of powdered material were used to minimize the effects of pinholes, inclusions of indium flux, and to prevent saturation effects.

The XANES for Ce L_{III}, Yb L_{III}, and Rh K edges are shown in Fig. 3.3 parts (a), (b), and (c) for the $x = 0.03$, 0.1, and 0.17 samples, respectively. The ratio of the In (edge not shown) concentration to the Rh concentration was roughly 4.8 ± 0.2 for each of the three concentrations measured, indicating that the Rh site is nearly fully occupied. The occupation of the Ce L_{III} and Yb L_{III} edges were determined by comparing the

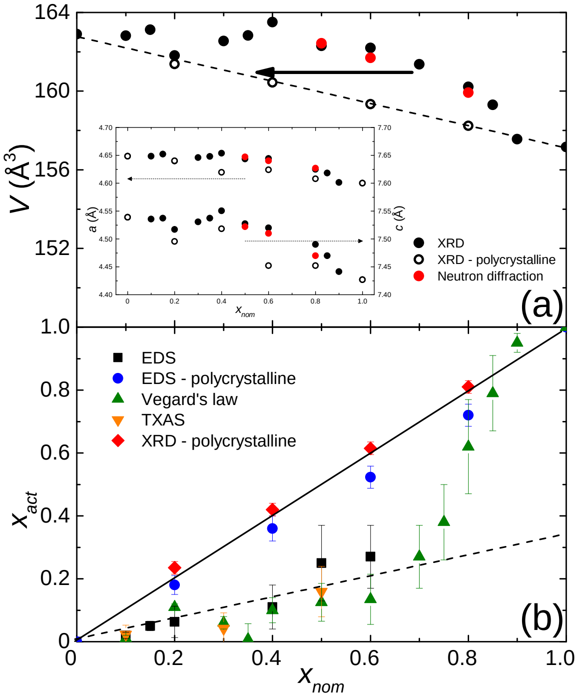

Figure 3.2. (a) Unit-cell volumes, plotted as a function of x_{nom}, calculated from XRD and neutron diffraction measurements on single- and polycrystalline samples. A linear extrapolation representing Vegard's law between the two parent compounds is shown as a guide to the eye; the horizontal (black) arrow emphasizes the discrepancy between the measured behavior of $V(x)$ and the Vegard's law construction. Plotted in the inset are the lattice parameters a and c vs. x_{nom}. (b) Comparison between the nominal and actual Yb concentrations determined from EDS, TXAS, and XRD measurements. A dashed line is drawn with slope $x_{act} = x_{nom}/3$, which fits the single crystal data well for concentrations $x_{nom} < 0.7$. For higher concentrations, the data deviate from this line and approach the $x_{act} = x_{nom}$ line. The results from EDS and XRD measurements on polycrystalline samples fit the expected relation shown by the line $x_{act} = x_{nom}$. Error bars where indicated represent one standard deviation throughout the article. These analyses establish a relationship between x_{act} and x_{nom}, ensuring that all subsequent discussions of Yb concentration can be limited to the actual concentration, such that $x = x_{act}$, unless otherwise stated.

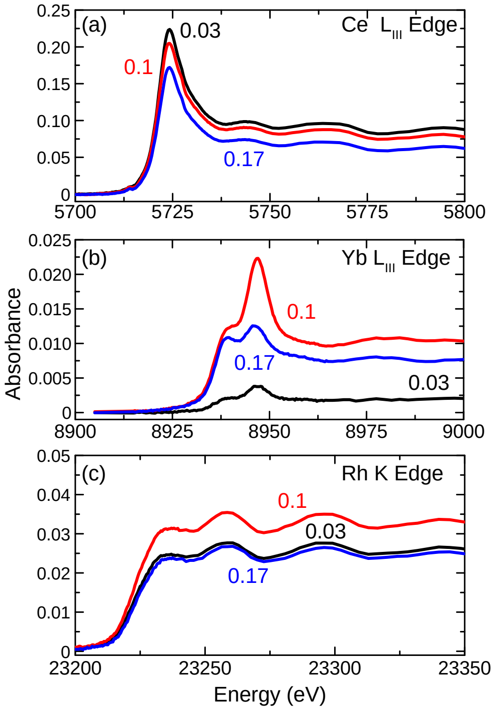

Figure 3.3. Un-normalized XANES data for Yb, Ce, and Rh. (a) shows the Ce L$_{\mathrm{III}}$ XANES for Ce$_{1-x}$Yb$_x$RhIn$_5$ where $x = 0.03$ is the top black line, followed by $x = 0.1$ as the red intermediate line, and $x = 0.17$ as the lower blue line. (b) The Yb L$_{\mathrm{III}}$ XANES, and (c) the Rh K XANES are shown for the same concentrations. All data were collected at $T = 200$ K and the 'pre-edge' has been subtracted from the data.

aforementioned cross-section adjusted edge height ratios to the Rh K edge for the same concentration. These results are presented in Fig. 3.2(b) for Yb for comparison with EDS and XRD measurements.

The Ce L$_{\mathrm{III}}$ edge and Rh K edge exhibit only a single-edge feature which indicates that only a single valence state is present for these atoms in the material. In contrast, the Yb L$_{\mathrm{III}}$ edge, shown in detail in Fig. 3.4, is composed of two slightly offset edges, indicating a mixed valence state. We briefly describe the XANES analysis used to determine the valence states for the different concentrations. The Yb^{2+} and Yb^{3+} valence states have different edge energies which are offset by several eV; Yb^{2+} absorbs near 8938 eV and Yb^{3+} near 8946 eV. To quantitatively determine the valence, two different offset edges were fit to the XANES data. Each edge is a sum of a broadened step function plus a Gaussian peak, centered at the same energy; the edge step is modeled as a convolution of a Gaussian distribution with a unit step function, and all Gaussians are assumed to have the same width, σ. The relative amplitudes of the Gaussians, the locations of each edge, E_1 and E_2, σ, and relative step heights were all determined from non-linear fits for each concentration. The fit was conducted only in the immediate vicinity of the edges where additional features of the XANES edge are minimal compared with the first, large peaks. In a recent XANES study of CaF_2:Yb, the absorption matrix element for the 2+ valence was found to be about 7% lower than for the 3+ valence state.[68] This correction was included in estimating the fractions $p_{\mathrm{Yb}^{2+}}$ and $p_{\mathrm{Yb}^{3+}}$ of the 2+ and 3+ valences respectively. Then the Yb average valence, z is given by $z = 2\ p_{\mathrm{Yb}^{2+}} + 3\ p_{\mathrm{Yb}^{3+}}$. These measurements show that the substituted Yb ion shifts from nearly trivalent Yb^{3+} at $x = 0$ down to intermediate-valence $\mathrm{Yb}^{2.1+}$ by $x = 0.2$.

3.3.3 Electrical Resistivity

Electrical resistivity measurements were performed on selected $\mathrm{Ce}_{1-x}\mathrm{Yb}_x\mathrm{RhIn}_5$ samples. These data are plotted in Fig. 3.5 and show an evolution of the Kondo lattice with Yb concentration in the range $0 \leq x \leq 0.27$. We observe a coherence peak associated with the Kondo lattice behavior which is manifested as a knee-like feature.

In Fig. 3.6, the Kondo coherence temperature, T^*, and $\rho(T^*)/\rho(200\ \mathrm{K})$ are plotted as a function of x. We defined T^* as the temperature where the slope of the resistivity exhibits the largest change; an example of this procedure is provided in the inset of Fig. 3.5. Values for T^* and $\rho(T^*)/\rho(200\ \mathrm{K})$ remain relatively stable with a slight dip as x increases from 0 to 0.2, before being rapidly suppressed as the Kondo lattice loses coherence at higher values of x; this coincides with the concentration where the Yb valence stabilizes at $v_{Yb} = 2.1+$. The stability of the Kondo lattice in the region

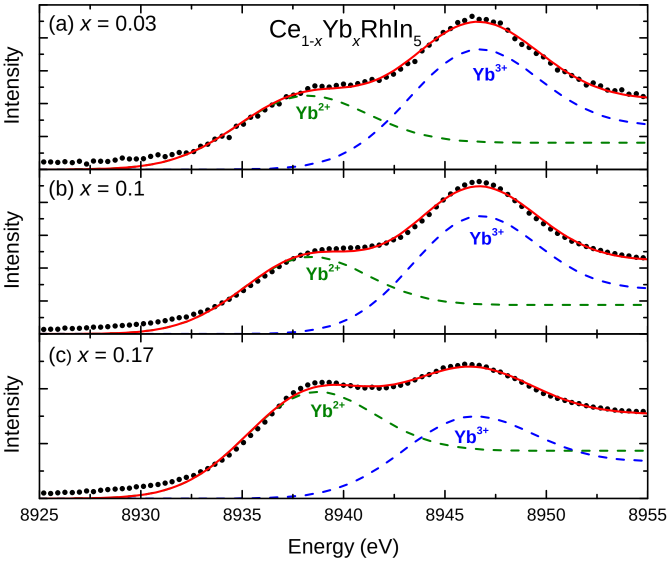

Figure 3.4. Measured Yb L_{III} edge data for $Ce_{1-x}Yb_xRhIn_5$ is plotted as black circles. The fit to the two-edge model is shown as the red solid line, while the dashed green line represents the contribution from Yb^{2+}, and the dashed blue line represents the contribution from Yb^{3+}. The results are shown over the same energy ranges for $x = 0.03$, 0.1, and 0.17 in panels (a), (b), and (c), respectively.

$x < 0.2$ may suggest a cooperative relationship between a decreasing, unstable Yb valence and the decrease in number of host Ce^{3+} ions with increasing x. Once the Yb valence becomes stable at about 2.1+, the Kondo lattice behavior weakens as Ce is replaced by Yb. This x-dependent behavior of the Kondo lattice is consistent with other findings in the $Ce_{1-x}Yb_xRhIn_5$ system where the valence of Yb and the magnetic structure are intertwined.

For the samples whose measurements are presented in Figs. 3.5 and 3.6, the residual resistivity ratio (RRR) was calculated according to the relation

$$\mathrm{RRR} = \rho(300\ \mathrm{K})/\rho(0\ \mathrm{K}), \tag{3.1}$$

where the values of $\rho(0\ \mathrm{K})$ were estimated by extrapolating the $\rho(T)$ data to 0 K. The evolution of the RRR with x_{nom} shows significantly large values of the RRR for

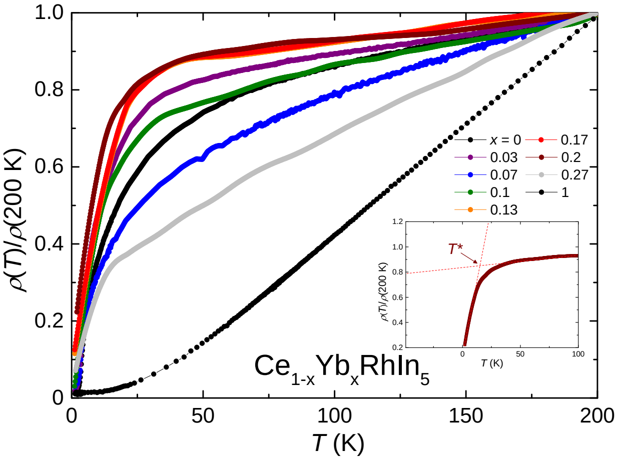

Figure 3.5. Electrical resistivity data for selected samples of $\mathrm{Ce}_{1-x}\mathrm{Yb}_x\mathrm{RhIn}_5$, normalized by electrical resistivity values measured at 200 K. The Kondo coherence feature for samples is observed near 25 K. (Inset) Example of T^* being calculated for the $x = 0.2$ sample.

both parent compounds ($x = 0$ and $x = 1$). However, as x_{nom} is increased from 0, the RRR drops precipitously, which suggests a possible relationship between the RRR and the difficulty in synthesizing substituted samples of $\mathrm{Ce}_{1-x}\mathrm{Yb}_x\mathrm{RhIn}_5$ (described in the Experimental Details section).

3.3.4 Magnetic Susceptibility

Measurements of magnetic susceptibility as a function of temperature were made with the magnetic field, H, oriented both in the *ab*-plane and along the *c*-axis; the measured magnetization, M, was divided by the applied magnetic field $\mu_0 H = 0.5$ T to obtain the magnetic susceptibility. These data are plotted as a function of temperature in Fig. 3.8. Two features are apparent in the data at low temperature, which are highlighted in the inset of Fig. 3.8(a). The inflection point, which is the signature for the AFM transition, is indicated by a dotted black line that acts as a guide to the eye. The maximum value of the magnetic susceptibility is observed at a temperature T_M that decreases with increasing x. This maximum at T_M corresponds to a deviation from Curie-Weiss behavior and is

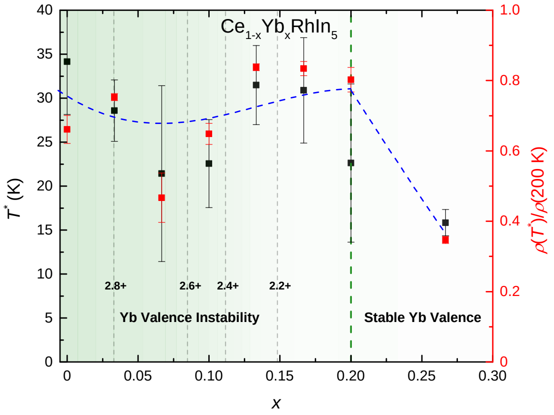

Figure 3.6. The characteristic Kondo coherence temperature, T^*, and $\rho(T^*)/\rho(200\text{ K})$, vs. Yb concentration x. The Yb valence is indicated by the false (color) background (3+ on the green side at $x = 0$ and $\sim 2.1+$ for $x > 0.2$). The Yb valence crossover at $x = 0.2$ is indicated by a vertical dashed (green) line that acts as a guide to the eye. A blue dashed curve shows the progression of both T^* and $\rho(T^*)/\rho(200\text{ K})$ as a function of x.

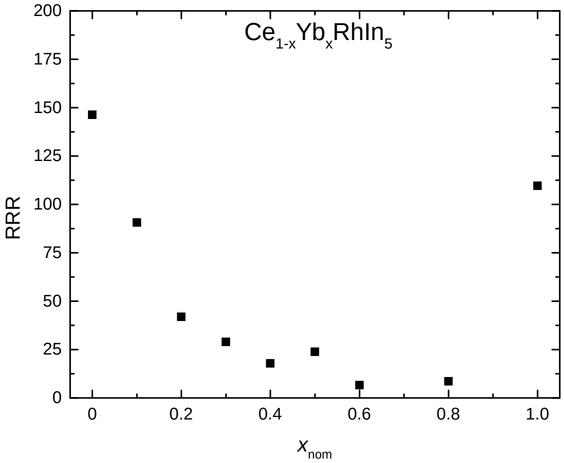

Figure 3.7. Calculated RRR values from $\rho(T)$ plotted vs. x_{nom} for Ce$_{1-x}$Yb$_x$RhIn$_5$. At $x_{\text{nom}} = 0$, the RRR ≈ 150. As Yb is introduced, the RRR drops precipitously. For the pure YbRhIn$_5$ compound, the RRR increases to above 110, suggesting that substituted samples are likely to yield low RRR values, potentially related to the issues raised regarding synthesis in the range $x_{\text{nom}} > 0.8$ discussed in the text.

consistent with the crystalline electric field effects observed in $CeRhIn_5$.[69,70] The inset of Fig. 3.8(b) shows the ratio of magnetic susceptibility with magnetic field applied in both orientations at 10 K. The ratio is roughly constant at $\chi_{ab}/\chi_c = 0.5$ for $x < 0.3$.

The inverse of the magnetic susceptibility, χ^{-1}, vs. T is plotted over a large temperature range in Fig. 3.9(a). For all x, the $\chi(T)$ data can be described by the Curie-Weiss relation,

$$M/H = C_0/(T - \Theta_{CW}), \tag{3.2}$$

where C_0 is the Curie constant and Θ_{CW} is the Curie-Weiss temperature. The average effective magnetic moment of the rare-earth ions, μ_{eff}, is estimated using the relation $C_0 = \mu_{eff}^2 N_A/3k_B$, where N_A is Avogadro's number and k_B is Boltzmann's constant.

Values of $\mu_{eff}(x)$ are found to decrease monotonically from $\sim 2.5\ \mu_B$ for $x = 0$ to approximately $1.6\ \mu_B$ at $x = 0.27$. To obtain an estimate for the valence of Yb, v_{Yb}, data for $\mu_{eff}(x)$ can be modeled using the equation:

$$\mu_{eff} = \sqrt{(\mu_{Ce^{3+}})^2(1-x) + [(\mu_{Yb^{3+}})^2(v_{Yb}(x)-2)(x)]} \tag{3.3}$$

where the free ion values of $\mu_{Ce^{3+}}$ and $\mu_{Yb^{3+}}$ are 2.54 and 4.54 μ_B, respectively, and v_{Yb} represents the valence of Yb.

Values of μ_{eff} are plotted in Fig. 3.9(b) as a function of x. The dashed lines represent the theoretical behavior for $\mu_{eff}(x)$ using Eq. 3.3 and assuming that all Yb ions are either divalent or trivalent. In these calculations, Ce is always assumed to be trivalent. We observe that $\mu_{eff}(x)$ follows the behavior expected for Yb^{3+} for very low x until it crosses over to being more consistent with Yb^{2+}. This result is consistent with the study of $Ce_{1-x}Yb_xCoIn_5$ where Yb is trivalent near $x = 0$, but its valence decreases to an intermediate value of 2.3+ at $x \approx 0.07$.[39] We applied Eq. 3.3 to extract values for v_{Yb} as a function of x; the values obtained are consistent with results from TXAS measurements

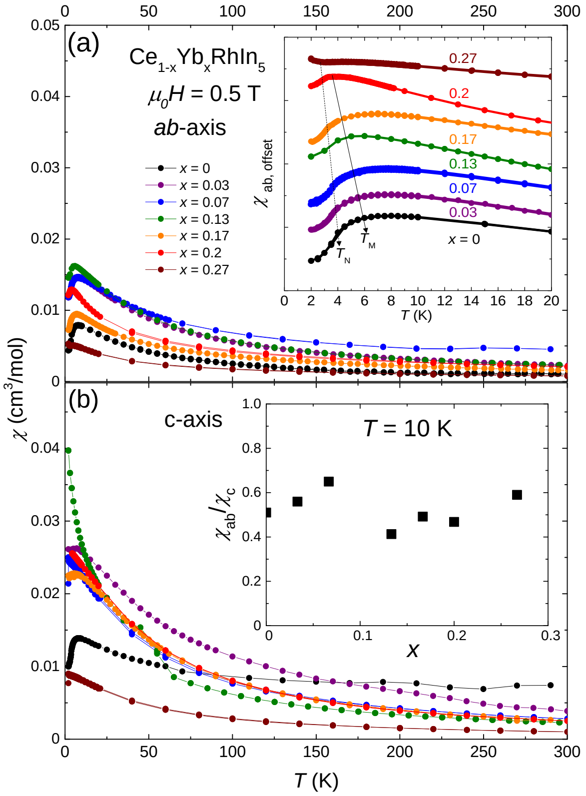

Figure 3.8. (a) Magnetic susceptibility measured in an applied magnetic field of $\mu_0 H =$ 0.5 T along the *ab*-plane is plotted from 0 to 300 K. The inset shows data for $0 \leq T \leq 20$ K where a black, dotted line is drawn through an inflection point, which is a signature of the AFM transition. The maximum value of magnetic susceptibility decreases with x. The temperature of the maximum is denoted T_M and is shown by the dash-dotted line. Due to a low-T upturn in the magnetic susceptibility for $x = 0.27$, T_N is difficult to define, and thus not indicated with the dashed line. (b) Magnetic susceptibility data measured with magnetic field applied along the c-axis are plotted from 0 to 300 K. For this orientation, only some concentrations exhibit a clear feature at low temperature associated with AFM ordering; other concentrations are dominated by an upturn in this temperature range. The inset shows the ratio χ_{ab}/χ_c at 10 K, which is above the AFM transition but below the temperature range exhibiting Curie-Weiss behavior. The values of χ_{ab}/χ_c are scattered about 0.5 over the range of concentrations measured.

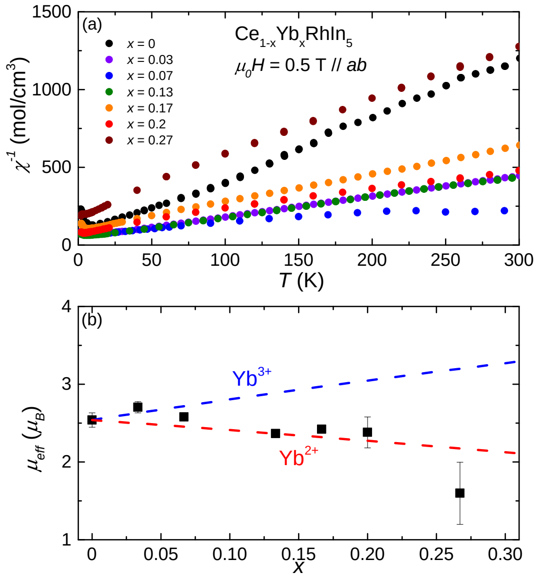

Figure 3.9. (a) Inverse magnetic susceptibility, χ_{ab}^{-1}, plotted for temperatures up to 300 K, exhibits linear Curie-Weiss behavior at high temperatures. (b) The effective magnetic moment, μ_{eff}, for $x < 0.33$ was calculated from the c-axis measurements and is plotted as a function of x. Dashed curves indicate theoretical calculations for μ_{eff} in $Ce_{1-x}Yb_xRhIn_5$ assuming Yb valences of Yb^{2+} and Yb^{3+}.

as described in the discussion section.

3.3.5 Specific Heat

Specific heat measurements were performed in zero magnetic field on samples in the system $Ce_{1-x}Yb_xRhIn_5$ with actual Yb concentrations of x_{act} = 0, 0.07, 0.13, 0.15, 0.17, 0.18, 0.2, 0.23, and 0.27. These data are displayed in Fig. 3.10(a) with C/T plotted as a function of temperature below 20 K. A dramatic evolution of the magnetic phase transition with Yb concentration is evident both in the suppression of T_N and in the change in magnitude of the feature at T_N. These results are consistent with a similar evolution with x that was observed in the systems $Ce_{1-x}La_xRhIn_5$ and $Ce_{1-x}Y_xRhIn_5$.[71,64] The magnitude of the peak at T_N decreases with increasing x as a broad hump feature emerges near T_N. This broad hump is a signature of short-range magnetic correlations that take an increasing amount of the entropy, leaving a smaller peak feature with less entropy at T_N.[71]

The Sommerfeld coefficient, γ, and Debye temperature, Θ_D, were determined from these data by plotting C/T vs. T^2 and fitting the linear portion for $T > T_N$ with the expression, $C/T \simeq \gamma + \beta T^2$, where $\beta = \frac{12\pi^4 N_A k_B}{5\Theta_D^3}$. Such a procedure is shown for representative data in Fig. 3.10(b), where a linear region is seen for $T > T_N$. The best-fit results for γ and Θ_D are plotted as functions of x in Figs. 3.10(c) and (d), respectively. The Sommerfeld coefficient for most Yb concentrations is roughly $\gamma \approx 200$ mJ mol^{-1} K^{-2}. γ was previously determined from low-temperature ($T < T_N$) fits to C/T data in two studies of the system Ce$_{1-x}$La$_x$RhIn$_5$;[72,71] this procedure resulted in smaller values of γ: ≤ 100 mJ mol-Ce^{-1} K^{-2} and $\sim$50 mJ mol^{-1} K^{-2}.[72,71] Kim, *et al.* discussed the difficulty of extracting γ from data for CeRhIn$_5$ because of the contributions due to magnetic order.[72] Our results for γ may be higher than previous results due to partial gapping of the Fermi surface that is associated with the formation of the SDW ground state.[50] We extracted γ using data measured at $T > T_N$ where the Fermi surface is presumably ungapped, while Refs. 72,71 used fits to data in the temperature range $T < T_N$. The Debye temperature is relatively x-independent, as expected, maintaining a value of $\Theta_D \simeq 200$ K for all Yb concentrations.

In zero magnetic field, the compound CeRhIn$_5$ exhibits an incommensurate antiferromagnetic structure below T_N, characterized by a wave vector q_M = (1/2, 1/2, 0.297) and Ce moments that reside within the easy *ab*-plane.[50] When a magnetic field is applied within the *ab*-plane, a field-induced phase transition is observed.[52,46] Such a transition has also been observed in measurements on the system Ce$_{1-x}$La$_x$RhIn$_5$ under similar conditions.[71] Below T_1, as field is applied, CeRhIn$_5$ enters the "$++--$", commensurate magnetic phase.[46] Data from heat capacity measurements on CeRhIn$_5$ in magnetic fields up to $\mu_0 H$ = 9 T are shown in Fig. 3.11(a). A magnetic field-induced

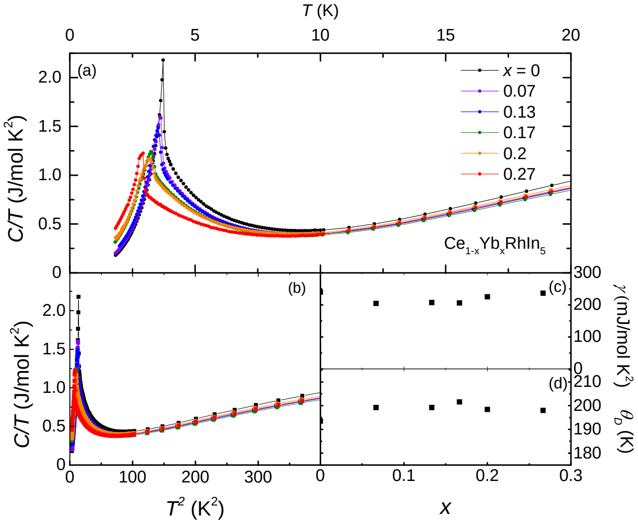

Figure 3.10. (a) Specific heat divided by temperature, C/T, plotted as a function of temperature, T. (b) C/T plotted as a function of T^2 for selected concentrations; the linear region of data in the temperature range $T > T_N$ obeys the relationship $C/T \simeq \gamma + \beta T^2$. Best fit results are plotted as functions of actual Yb concentration, x_{act}, for (c) the Sommerfeld coefficient, γ, and (d) the Debye temperature, Θ_D.

feature at $T_1 < T_N$ is observed when $\mu_0 H \geq 3$ T and $H \parallel ab$, and T_N is observed to increase with increasing H. When $H \parallel c$, T_N is slowly suppressed and it appears that no magnetic field-induced features emerge. These results agree with those from previous reports.[71]

Zero-field specific heat measurements for Ce$_{1-x}$Yb$_x$RhIn$_5$ single crystals are displayed in Fig. 3.11(b); these data have been offset by an amount $\delta C/T = 0.5$ J mol^{-1} K^{-2} for visual clarity. Yb substitution for Ce suppresses T_N at a rate that appears to be consistent with that for La- and Y-substitution.[72,71,64] On the other hand, unlike in previous work on La- and Y-substitution, we observe a second feature that emerges at a temperature $T_I < T_N$ for $x \geq 0.18$. T_I decreases slowly with increasing x. The character of this broad feature seems to preclude it from being associated with a first-order phase transition.

Specific heat measurements were performed in the vicinity of the AFM transition

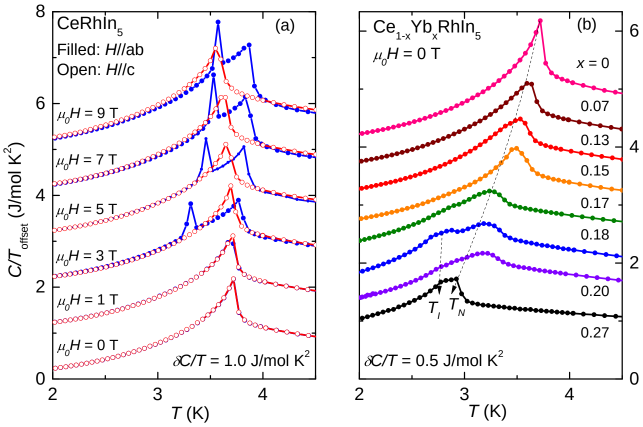

Figure 3.11. (a) Specific heat divided by temperature, C/T, for CeRhIn$_5$ in applied magnetic fields $\mu_0 H$ of up to 9 T; H was applied parallel to both the *ab*-plane (filled circles) and along the *c* axis (open circles). Note that data measured in different magnetic fields have been offset from one another by an amount $\delta C/T$ = 1.0 J/mol K^2 for visual clarity. When $H \parallel c$, we observe a single feature at T_N which is gradually suppressed to lower temperature with increasing H. When $H \parallel ab$ and $\mu_0 H > 3$ T, we observe a feature at T_N and a magnetic field-induced phase transition at T_1 ($T_1 < T_N$). (b) C/T data for Ce$_{1-x}$Yb$_x$RhIn$_5$ are plotted in the vicinity of T_N. The data for different concentrations have been offset from one another by an amount $\delta C/T$ = 0.5 J mol/K^2 for visual clarity. A second feature emerges at temperatures $T_I < T_N$ for $x_{act} > 0.18$. Dashed lines are guides to the eye which emphasize the evolution of T_N and T_I with Yb-concentration.

for $Ce_{1-x}Yb_xRhIn_5$ with x_{act} = 0, 0.07, 0.13, 0.20 in applied magnetic fields up to $\mu_0H = 9$ T. These results are summarized in Fig. 3.12. The data measured at different magnetic fields have been offset by amounts $\delta C/T$ to more clearly follow the evolution of behavior with H. A first-order magnetic-field induced phase transition is observed for x_{act} = 0, 0.07, and 0.13 when $\mu_0H \geq 3$ T; we were unable to observe any strong signature of this magnetic field-induced transition in data for $x_{act} = 0.20$. It appears that the separation between T_1 and T_N decreases with increasing x, suggesting that disorder may promote a commensurate magnetic structure over the incommensurate magnetic structure of $CeRhIn_5$.

One explanation for the tendency towards commensurate magnetic order may be that disorder weakens the next-nearest neighbor exchange interactions, thus lifting the magnetic frustration between antiferromagnetic nearest (J_1) and next-nearest neighbor (J_2) exchange along the c axis that drives the emergence of the incommensurate antiferromagnetic structure for x_{act} = 0.[51] Another possibility is that changes in the Yb valence as x is increased could affect the orbital characteristics of the $4f$ electronic wave function and, in turn, result in additional magnetic anisotropies that favor commensurate order. We note that such changes in orbital character have recently been reported both as a function of chemical substitution[73] and magnetic field.[74] Both T_1 and T_N increase with increasing H, which is consistent with the $H-T$ phase diagram determined by Light *et al.* for the case of La substitution.[71] One possibility is for the two effects described above to work in tandem to generate the observed behavior. However, based on similarities to the $Ce_{1-x}Yb_xCoIn_5$ system, which exhibits a valence transition at the same value of x where there is a change in the electronic structure, and the fact that the RRR is consistently large throughout the full range of x shown in Fig. 3.7, it seems more likely that the latter mechanism involving changes in the orbital characteristics of the $4f$ electronic wave functions causes the modifications in the magnetic structure.

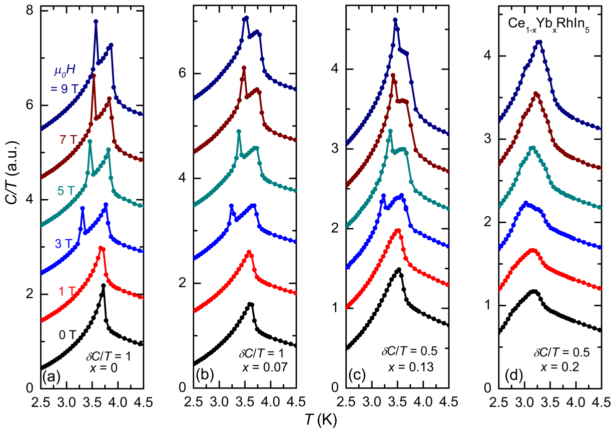

Figure 3.12. Specific heat divided by temperature, C/T, vs. temperature T for selected Yb concentrations in the system $\mathrm{Ce}_{1-x}\mathrm{Yb}_x\mathrm{RhIn}_5$: (a) $x = 0$, (b) $x = 0.07$, (c) $x = 0.13$, and (d) $x = 0.20$. For each concentration, measurements were performed in applied magnetic fields of $\mu_0 H = 0$, 1, 3, 5, 7, and 9 T (applied along the *ab*-plane). Data measured in different magnetic fields have been offset from one another by an amount $\delta C/T$ = 0.5-1 J/ mol K^2 for visual clarity. Two distinct features are observed in CeRhIn_5 for $\mu_0 H \geq 3$ T. At constant magnetic field, these features appear to merge with increasing x, such that a single broad feature is observed for $x = 0.20$ in magnetic fields of up to 9 T.

3.3.6 Neutron Diffraction

Neutron diffraction measurements, collected in the HHL scattering plane with neutrons of incident energy $E_i = 14.7$ meV, are able to probe the crystal structure, magnetic moments of the constituent ions, and the magnetic structure of the ordered ground states. We performed such measurements on our $\mathrm{Ce}_{1-x}\mathrm{Yb}_x\mathrm{RhIn}_5$ single crystals to determine whether or not there is a link between the variation of the Yb valence and the magnetic structure. To extract meaningful magnetic moments from neutron scattering data, corrections for neutron-neutron absorption must be made.[75] Due to the large neutron absorption cross-sections of both In and Rh, and the irregular shape of the samples, making the corrections is problematic in the present case, and hence, the moment values from the magnetic susceptibility measurements are likely more reliable.

An incommensurate AFM structure was found for samples with $x = 0.17$ and

0.2 that could be described by a propagation vector q = (0.5, 0.5, 0.297(0.002)); this magnetic structure is identical to that of $\mathrm{CeRhIn_5}$.[50] The magnetic scattering intensity is obtained in terms of absolute units by normalizing the integrated intensity of these magnetic reflections by the (110) and (002) nuclear reflections. Using the details of the magnetic structure determined by Bao *et al.*[76] for the parent compound, the results from neutron diffraction for $\mathrm{Ce_{1-x}Yb_xRhIn_5}$ were expressed in units of μ_B^2/f.u. and plotted as a function of temperature in Fig. 3.13(a)-(c); the resulting intensities show the development of magnetic order as the temperature is cooled below the Néel temperature, T_N.

A region of the HHL zone in reciprocal space was mapped using the position-sensitive detector (PSD) for a representative concentration, $x = 0.17$; it is shown in Fig. 3.13(d). The PSD covers an angular range over five degrees in scattering angle, and hence data were collected for several scattering angles separated by 5°, rotating the crystal in steps on 0.25° over a range of 100°. This measurement was conducted to ensure that no extraneous reflections are present which would suggest additional modifications to the magnetic structure, relative to that of the parent compound. In addition to the bright (110) and (002) nuclear reflections, we find a series of peaks along the $q = (0.5, 0.5, l)$ vector in the inset of Fig. 3.13(d). Note that because of the small dimensions of the sample relative to the aluminum sample plate, a substantial background contribution is observed for parts of the map appearing as temperature-independent streaks or peaks of elevated intensity at larger ‘radii’.

The Néel temperatures, T_N, for $x = 0.17$, 0.20, and 0.27, were extracted by fitting the integrated intensity of a representative magnetic reflection at $Q = G + q$, where G is a reciprocal lattice vector, with a mean-field order parameter function. The best fits are denoted by the solid lines in Fig. 3.13(a)-(c). The ordering temperatures are plotted in Fig. 3.14(b).

In contrast to the results for the other concentrations, the $x = 0.27$ sample exhibits commensurate order along the unit-cell diagonal described by a propagation vector q = (0.5, 0.5, 0.5). No evidence for the incommensurate phase was observed along the (0.5, 0.5, l) direction as shown in the inset of Fig. 3.13(c).

For the compound with $x = 0.27$, a second transition, T_I, below T_N is observed in $C(T)$. However, neutron diffraction measurements show only one transition in this compound, described above as commensurate AFM order at T_N, revealing that T_I is unaccounted for in the neutron diffraction measurements. Possible reasons for this can be that the changes in the magnetic structure below T_I are subtle, or that a different magnetic structure with a distinct propagation vector coexists with the identified commensurate order. Additionally, the inability to detect this potential propagation vector may suggest that the second modulation may have a miniscule magnetic moment. Finally, the transition T_I may be associated with a different phenomenon such as a Lifshitz transition that reflects subtle changes in the electronic density of states. This may be related to changes in the hybridization of conduction- and f-electron states due to the observed valence change.

The difference in magnetic structure for $Ce_{1-x}Yb_xRhIn_5$ between the $x = 0.17$, 0.20, and the $x = 0.27$ samples suggests that there is a crossover or transition from incommensurate to commensurate AFM order between $0.20 \leq x \leq 0.27$, which coincides with changes observed in the behavior of electrical resistivity, magnetic susceptibility, and specific heat measurements for this concentration range.

3.4 Concluding Remarks

3.4.1 Phase Diagram

Shown in Figs. 3.14(a) and (b) are the Yb valence, v_{Yb}, and the Néel temperature, T_N, vs. Yb concentration, respectively. Plots of these v_{Yb} and T_N vs. x are shown to emphasize a potential link between the magnetic structure of $Ce_{1-x}Yb_xRhIn_5$ and the valence of Yb. The incommensurate AFM phase appears to correspond to the region over which the Yb valence varies between 3+ and 2.1+, while the commensurate AFM phase appears when the Yb valence becomes stable at 2.1+.

3.4.2 Discussion

The phase purity and crystal structures of $Ce_{1-x}Yb_xRhIn_5$ single crystals, synthesized using a molten In flux technique, were confirmed through Rietveld refinement analysis on powder XRD patterns. Given the well-documented subnominal Yb concentrations found in single crystals of the related system, $Ce_{1-x}Yb_xCoIn_5$, we determined the actual Yb concentrations in our $Ce_{1-x}Yb_xRhIn_5$ single crystals using EDS and TXAS measurements. Combining the results from these measurements with a Vegard's law analysis of the unit-cell volume as a function of x, we determined that the actual Yb concentrations, x_{act}, are lower in our $Ce_{1-x}Yb_xRhIn_5$ single crystals than the nominal values, x_{nom}. In contrast, results of similar chemical and structural analysis on polycrystalline samples of $Ce_{1-x}Yb_xRhIn_5$ showed $x_{act} \simeq x_{nom}$. Using measurements of magnetic susceptibility and XANES, we estimated the Yb valence as a function of x. Just as has been observed in $Ce_{1-x}Yb_xCoIn_5$, we found that the Yb valence decreases as a function of x until stabilizing at an intermediate valence of 2.1+ near $x = 0.2$. Since the behavior of the valence of $Ce_{1-x}Yb_xRhIn_5$ is similar to that of $Ce_{1-x}Yb_xCoIn_5$, where there is also a Fermi surface reconstruction at $x = 0.07$ indicating an overall change in the electronic structure, it is reasonable to expect a Fermi surface reconstruction at $x = 0.2$ for $Ce_{1-x}Yb_xRhIn_5$. However, additional and difficult types of measurements such as Shubnikov-de Haas would need to be performed to confirm this scenario, although it could potentially provide an explanation for the observed magnetic phase transitions. Neutron scattering experiments demonstrate that the abrupt change in the x-dependence of the Yb valence near $x = 0.2$ coincides with a change in the magnetic structure from

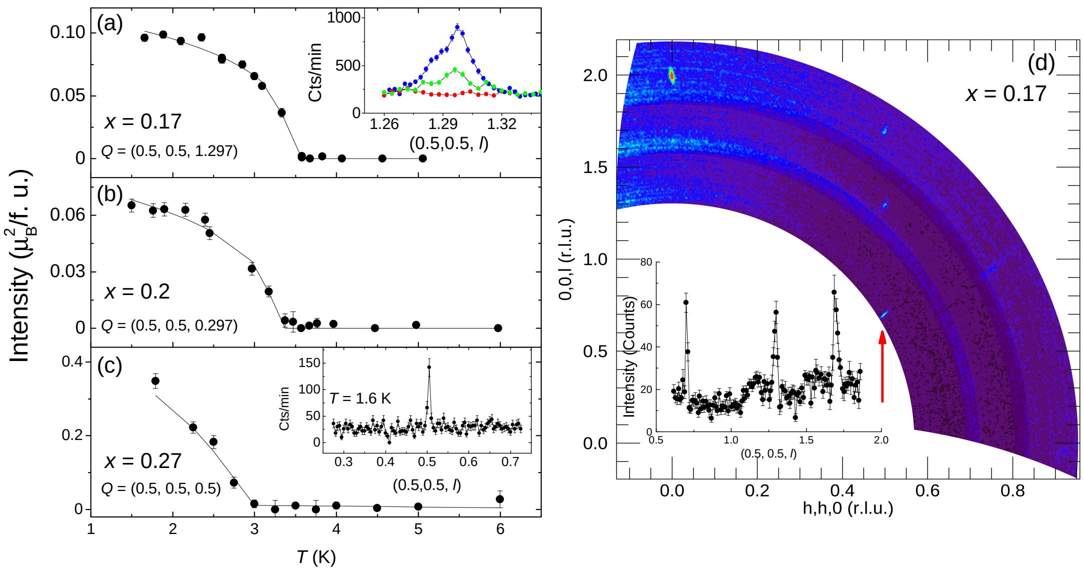

Figure 3.13. Neutron diffraction measurements on the BT-4 and BT-7 triple-axis spectrometers at the NIST Center for Neutron Research. (a)-(c) The Néel temperature T_N was determined for concentrations $x = 0.17$, 0.2, and 0.27 by fitting the integrated intensity of a representative magnetic reflection at $Q = G + q$, where G is reciprocal lattice vector, with a mean-field order parameter function denoted by the solid line. Examples of curves for selected temperatures are shown in the inset of (a), where at the lowest temperature, the peaks were resolution limited. A shoulder-like feature is observed at a slightly lower l; however, no shoulder is observed in scans of the nuclear reflections which indicates a distribution of q values. The inset of panel (c) demonstrates that no evidence for the incommensurate phase was observed for $x = 0.27$ along the (0.5, 0.5, l) direction. (d) A region of the HHL zone in reciprocal space was mapped at 1.5 K for $x = 0.17$. No additional magnetic reflections are present, which would suggest additional modifications to the magnetic structure. The inset of the panel (d), plotted using DAVE,[77] shows that, in addition to the bright (110) and (002) nuclear reflections, we observed a series of peaks along (0.5, 0.5, l), which are indexed using the same magnetic propagation vector, q.

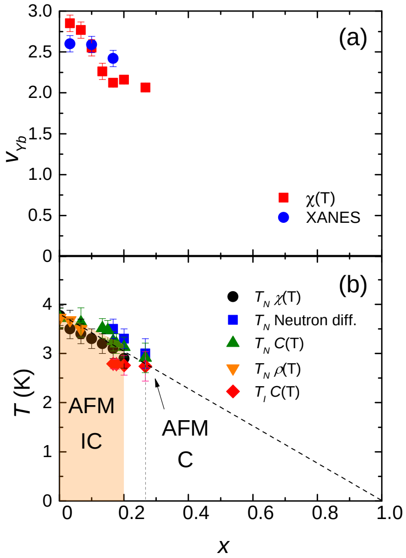

Figure 3.14. (a) Yb valence vs. Yb concentration, x, over the same concentration range as the temperature T vs. x phase diagram in the panel below. The valence was calculated from magnetic susceptibility measurements with the magnetic field in the *ab* and *c* orientations and from XANES measurements. (b) The T vs. x phase diagram for $Ce_{1-x}Yb_xRhIn_5$. The Néel temperature T_N is taken from measurements of the electrical resistivity, magnetic susceptibility, specific heat, and neutron diffraction. A linear fit, indicated by the dashed line, to the $T_N(x)$ data for $Ce_{1-x}Yb_xRhIn_5$ extrapolates to 0 K at $x = 1$. The orange region delineates incommensurate AFM order and the clear region represents commensurate AFM order.

an incommensurate AFM ground state for $0 \leq x \leq 0.2$ to a commensurate AFM ground state for $0.2 < x \leq 0.27$. Heat capacity measurements reveal that a second phase transition of magnetic origin emerges in this concentration range at a temperature $T_I < T_N$. Taken together, these results suggest a correlation between the magnetic structure of the heavy-fermion system, $\mathrm{Ce}_{1-x}\mathrm{Yb}_x\mathrm{RhIn}_5$, and the intermediate valence of Yb.

Acknowledgements

Research at UCSD was supported by the Air Force Office of Scientific Research MURI under Grant No. FA9550-09-1-0603 (sample synthesis and screening for superconductivity), the US Department of Energy under Grant No. DE-FG02-04-ER46105 (sample characterization and physical properties measurements), and the National Science Foundation under Grant No. DMR-0802478 (low-temperature measurements). The EXAFS work was supported under NSF Grant No. DMR1005568, and the experiments were performed at Stanford Synchrotron Radiation Lightsource, operated by the US Department of Energy, Division of Chemical Sciences. Support for J. C. was provided by the National Science Foundation under Agreement No. DMR-1508249. The identification of any commercial product or trade name does not imply endorsement or recommendation by the National Institute of Standards and Technology.

Chapter 3, in full, is a reprint of the material as it appears in Physical Review B (2018). Jang, S., Pouse, N., Keiber, T., White, B. D., Disseler, S. M., Lynn, J. W., Collini, J. C., Janoschek, M., Bridges, F., Maple, M. B., APS, 2018. The dissertation author was the primary investigator and author of this paper.

Chapter 4

Temperature vs. Sm concentration phase diagram and quantum criticality in the correlated electron system $Ce_{1-x}Sm_xCoIn_5$

We report electrical resistivity, magnetization, and specific heat measurements on the correlated electron system $Ce_{1-x}Sm_xCoIn_5$ ($0 \leq x \leq 1$). Superconductivity (SC) in the heavy fermion compound $CeCoIn_5$, which is suppressed with increasing Sm concentration x, and antiferromagnetic (AFM) order of $SmCoIn_5$, which is suppressed with decreasing x, converge near a quantum critical point at $x_{QCP} \approx 0.15$, with no indication of coexistence of SC and AFM in the vicinity of the QCP. Non-Fermi liquid (NFL) behavior is observed in the normal state electrical resistivity, $\rho(T)$, and specific heat, $C(T)$, in the vicinity of the QCP; e.g., the coefficient and the exponent of the power-law T-dependence of $\rho(T)$ exhibit pronounced maxima and minima, respectively, at x_{QCP}, while $C(T)/T$ exhibits a logarithmic divergence in T at x_{QCP}. A low-temperature upturn in $\rho(T)$ develops in the range $0.70 \leq x \leq 0.85$ which is reminiscent of a single impurity Kondo effect, suggesting that Sm substitution tunes the relative strength of competing Kondo and Ruderman-Kittel-Kasuya-Yosida (RKKY) energy scales. The suppression of SC with increasing x is probably associated with the exchange interaction between the

Ce quasiparticles involved in the superconductivity and the magnetic moments of the Sm ions.

4.1 Introduction

Quantum criticality has been an important and fascinating area of correlated electron research due in large part to its presence in disparate classes of materials including cuprates and iron pnictide high-temperature superconductors, as well as lanthanide- and actinide-based heavy-fermion (HF) metals.[78] A quantum critical point (QCP) emerges when a second-order phase transition is suppressed to zero temperature by tuning non-thermal control parameters such as chemical composition, applied pressure, or magnetic field, frequently yielding an observable superconducting state.[79] The proximity of superconductivity to magnetism in these materials has lead to an ongoing debate about the underlying mechanism behind the emergent superconductivity and continues to drive a great deal of research in this area.[80] The HF superconductors CeTIn$_5$ (T = Co, Rh, Ir) are a prototypical class of strongly correlated systems in which unconventional superconductivity (SC) emerges in close proximity to an antiferromagnetic (AFM) quantum critical point (QCP).[81,82,80,49]

The compound CeCoIn$_5$ is a d-wave superconductor[83,84,85,86] that has provided an opportunity to study the effects of impurities, either magnetic or non-magnetic, on an unconventional superconductor. The compound SmCoIn$_5$ is iso-structural with CeCoIn$_5$, but undergoes three successive phase transition[87] and has not been found to exhibit superconductivity under ambient or applied pressure up to 8 GPa.[88] This is in contrast with the related compound PuCoIn$_5$ in which superconductivity was observed[89]; PuCoIn$_5$ and SmCoIn$_5$ have the same crystal structure and Pu^{3+} shares the same f-electron shell configuration as Sm^{3+}.

Our study of the system Ce$_{1-x}$Sm$_x$CoIn$_5$reported herein was motivated by a series of studies on the system $Ce_{1-x}Yb_xCoIn_5$.[28,55] Ytterbium, which can have the same valence states as Sm (2+, 3+), was found to display valence fluctuations when substituted into the Ce site, while Ce remained trivalent.[39,28] The Yb valence decreases rapidly from 3+ at low x until stabilizing at 2.3+ for $x > 0.07$.[39] The decrease in Yb valence in $Ce_{1-x}Yb_xCoIn_5$ is accompanied by other anomalous phenomena at $x = 0.07$, such as suppression of the quantum critical field, H_{QCP},[61] a Fermi-surface reconstruction,[60] and a possible crossover from a nodal to nodeless superconducting energy gap.[62] This last result was observed in measurements of the London penetration depth, $\lambda(T)$;[62] though, recent thermal conductivity measurements do not show this change in the SCing energy gap.[63] This nodeless superconductivity has been explored by a composite pairing scenario in which a fully-gapped d-wave molecular superfluid of composite pairs form.[90] By substituting Sm into the Ce site in this study, we were interested in seeing whether we could observe some of the same phenomena reported in the Yb-substituted system.[59,40]

Our measurements of the specific heat of $SmCoIn_5$ indicate that there are two additional phase transitions besides AFM order at $T_N \sim 11.6$ K, including a first-order transition at 10.2 K, and another transition with a smaller feature at 6.0 K. This behavior, with three transitions, is similar to that observed in a previous study of $SmIn_3$;[91] however, the origin of these additional phase transitions is unknown in $SmCoIn_5$. From μSR measurements on $SmIn_3$, it is suggested that these ordering temperatures are associated with a transition between commensurate and incommensurate AFM states,[92] though the signatures of the transitions are qualitatively different when we compare specific heat measurements on $SmCoIn_5$ and $SmIn_3$. Additional experiments such as anomalous x-ray diffraction must be conducted to determine the nature of these transitions. Introducing Ce into $SmCoIn_5$ disrupts the additional phase transitions observed in $SmCoIn_5$ and results in a single, broad transition in the specific heat for concentrations down to $x = 0.175$. On the Ce-rich side of the phase diagram, we find that superconductivity is rapidly suppressed by $x = 0.15$. Electrical resistivity data demonstrate that the Kondo coherence temperature T^* is also suppressed with increasing x. The evolution of SC and AFM order across the $Ce_{1-x}Sm_xCoIn_5$ phase diagram provides information about the interplay of these two phenomena and non-Fermi liquid (NFL) behavior of the physical properties near a QCP in this system.

4.2 Experimental Details

Single crystalline samples of $Ce_{1-x}Sm_xCoIn_5$ were grown using a molten In flux as described in Ref. 64. The crystal structure was characterized through analysis of powder x-ray diffraction (XRD) patterns collected by a Bruker D8 Discover x-ray diffractometer using a Cu-K_α source. The chemical composition was investigated by means of energy-dispersive x-ray spectroscopy (EDX) using an FEI Quanta 600 scanning electron microscope equipped with an INCA EDX detector from Oxford Instruments. Four-wire electrical resistivity measurements, $\rho(T)$, were performed from 300 K down to $\sim$ 1.1 K in a pumped ^{4}He Dewar and down to 1.8 K in a Quantum Design Physical Property Measurement System (PPMS) DynaCool. For selected samples, $\rho(T)$ was also measured down to 25 mK in an Oxford Kelvinox-300 ^{3}He-^{4}He dilution refrigerator. Magnetic susceptibility measurements were performed between 300 K and 2 K in a Quantum Design Magnetic Property Measurement System (MPMS) equipped with a 7 T superconducting magnet. Specific heat measurements were performed down to 1.8 K in a Quantum Design PPMS DynaCool and down to 0.5 K using a ^{3}He option. All specific heat measurements were made using a standard thermal relaxation technique.

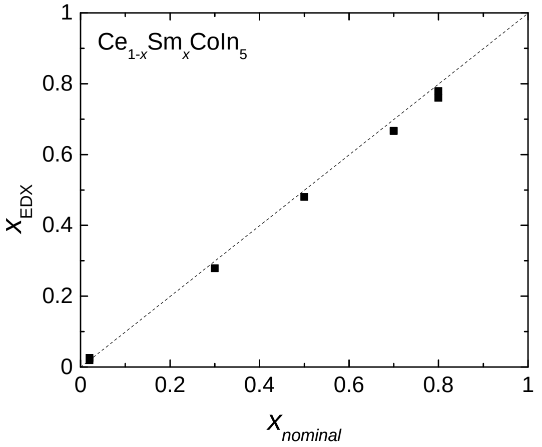

Figure 4.1. Energy-dispersive x-ray spectroscopy (EDX) measurements were performed on selected single crystals of $Ce_{1-x}Sm_xCoIn_5$. We observed excellent agreement between the measured and nominal Sm concentrations. EDX measurements were performed at several locations for each sample to evaluate the chemical homogeneity of synthesized single crystals. The dashed line is a guide to the eye.

4.3 Results

4.3.1 Crystal Structure

EDX measurements were performed on selected single crystals used for measurements in this study; we observed excellent agreement between measured (x_{EDX}) and nominal Sm concentration values (x_{nom}) over the entire range of x as shown in Fig. 4.1. Deviations from this agreement may represent inhomogeneity within the single crystals being measured by EDX or experimental error from the analysis on Sm concentration. Another plausible explanation is the formation of $SmIn_3$ using excess In from the molten flux melt which would contribute to a Sm deficiency in the single crystals. This explanation is backed by observations in $C(T)$ measurements of rare $Ce_{1-x}Sm_xCoIn_5$ single crystals showing multiple peaks associated with $SmIn_3$ transitions.[91] Crystals exhibiting this behavior were screened; however, this could still account for small deficiencies in Sm which can be manifested in EDX and powder XRD data for the lattice parameters.

These results suggest that there is neither a solubility limit nor a miscibility gap in the $Ce_{1-x}Sm_xCoIn_5$ system.

Rietveld refinements were performed on powder XRD patterns for each sample using GSAS [31] and EXPGUI [32]; the lattice constants are presented in Figs. 4.2(a) and (b), while the unit-cell volume is shown in Fig. 4.2(c). The $Ce_{1-x}Sm_xCoIn_5$ system exhibits a single tetragonal crystal structure with space group $P4/mmm$ over the entire concentration range. A representative XRD pattern for an $x = 0.1$ sample is displayed in Fig. 4.2(d). The expected Bragg reflection pattern is shown in red and the measured XRD pattern is displayed as a black scatter plot that overlaps the refined XRD pattern. The agreement between our data and the refinement results was excellent for all samples with typical reduced χ^2 values of less than 5. The lattice constants, a and c, along with the unit-cell volume, V, decrease linearly with increasing Sm concentration which is in agreement with Vegard's law (see Figs. 4.2(a)-(c)). This adherence to Vegard's law suggests that the Sm valence remains constant at 3+ for all concentrations.

4.3.2 Electrical Resistivity

Electrical resistivity, $\rho(T)$, measurements were performed on selected samples in the $Ce_{1-x}Sm_xCoIn_5$system, and the data are displayed in Fig. 4.3. The behavior of $\rho(T)$ evolves with increasing Sm concentration through three distinct regions: low Sm concentrations with $x \leq 0.6$ (panel (a)), intermediate region $0.7 \leq x \leq 0.85$ (panel (b)), and high Sm-concentration region of $x \geq 0.9$ (panel (c)). From published studies, we expect a superconducting transition in $CeCoIn_5$ [81,82,80] and three successive phase transitions, one of which is AFM, for $SmCoIn_5$.[87,88] Our data for the parent compounds are consistent with published studies; rare-earth substitution (Sm for Ce or Ce for Sm) away from the Ce- and Sm-based parent compounds suppresses these transitions to lower temperatures.

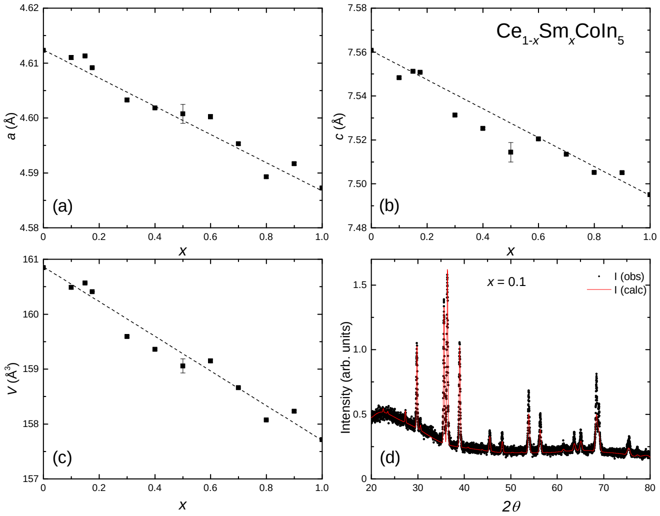

Figure 4.2. (a), (b) Lattice constants, a and c, plotted as a function of x, respectively. (c) Volume of the unit cell, V, plotted as a function of x. (d) Representative powder x-ray diffraction pattern for an $x = 0.1$ sample (black circles) and calculated fit from the Rietveld refinement (red line) used to determine the lattice constants a and c. In panels (a)-(c), dashed lines are guides to the eye. Error bars for all concentrations and most are less than or of the order of 10^{-4} Å; however, the $x = 0.5$ sample has a larger error bar of the order of 10^{-3} Å.

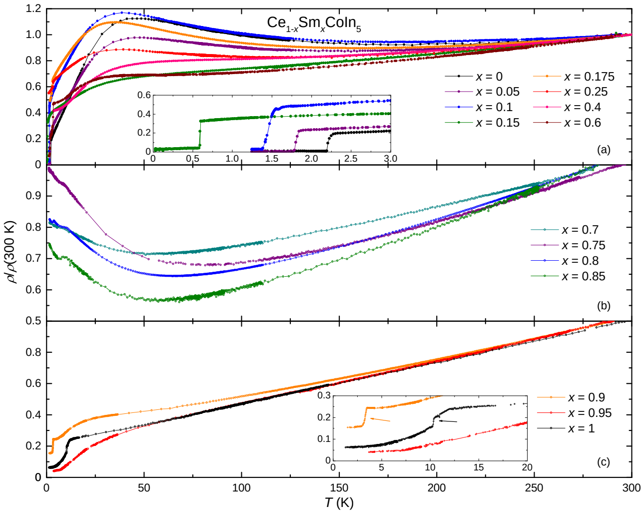

Figure 4.3. Electrical resistivity, ρ, normalized by its value at 300 K, plotted vs. temperature, T, for Ce$_{1-x}$Sm$_x$CoIn$_5$. (a) Samples with low Sm concentration display both a coherence peak associated with the formation of a coherent Kondo lattice and superconductivity (see inset) that is suppressed with increasing x. (b) As x increases above 0.6, we observe a crossover into a single-ion-like Kondo effect in which Ce ions behave as a magnetic impurity in SmCoIn$_5$. (c) On the Sm-rich side of the phase diagram, the only salient feature observed is a sharp, "knee-like" feature consistent with AFM order of the Sm sublattice, as observed previously (see inset).[88]

Upon chemical substitution away from the Ce- and Sm-based end member compounds, both T_N and T_c appear to be suppressed linearly initially (see the phase diagram in Fig. 4.4); we were unable to observe evidence for co-existence of SC and AFM order in measurements down to $\sim$ 25 mK at any Sm concentration, x. We note that it was difficult to clearly identify AFM order for some concentrations due to the presence of the coherence peak and the decreasing size of the drop in $\rho(T)$ associated with the onset of the AFM order. Therefore, only electrical resistivity data are used to identify T_c, while T_N is determined from specific heat data that will be discussed below. These results are summarized in the phase diagram in Fig. 4.4.

As we alloy away from each parent compound, we also observe a change in the interplay between the Ruderman-Kittel-Kasuya-Yosida (RKKY) interaction and the

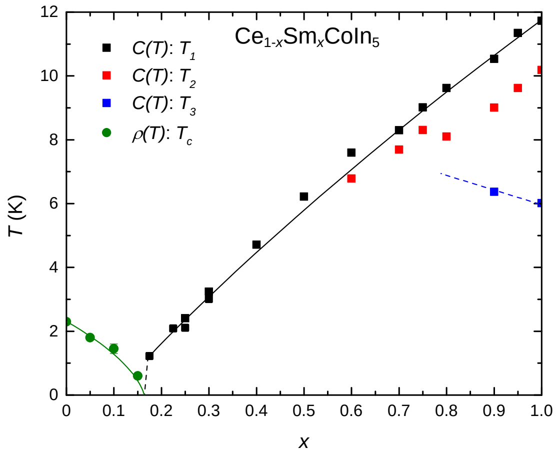

Figure 4.4. Superconducting critical temperature, T_c, and Sm ordering temperatures T_1, T_2, and T_3 (where T_1 is the Néel temperature, T_N) vs. Sm concentration, x. Lines are guides to the eye.

Kondo effect. For CeCoIn$_5$, a coherence peak in $\rho(T)$ associated with the formation of a Kondo lattice involving Ce^{3+} ions is observed. With increasing x, the coherence peak gradually shifts to lower temperature and broadens as seen in Fig. 4.3(a). The magnitude and position of the peak in $\rho(T)$ associated with Kondo lattice behavior may not evolve smoothly throughout the alloy series due to the influence on the aforementioned Kondo lattice of single-ion Kondo-like behavior, AFM and other types of order of the Sm ions, RKKY interactions between Ce and Sm ions, crystalline electric field (CEF) effects, atomic disorder, etc. These effects are highly sensitive to the Ce to Sm ratio which may vary somewhat throughout a Ce$_{1-x}$Sm$_x$CoIn$_5$ single crystal. For $x \geq 0.7$, the Ce^{3+} ion concentration is so dilute that a coherent Kondo lattice can no longer form, which explains the absence of a coherence peak for $x \geq 0.7$. Instead, a minimum followed by an upturn in $\rho(T)$ with decreasing temperature is observed as shown in Fig. 4.3(b). This behavior is reminiscent of the single-ion Kondo effect associated with a moderately dilute concentration of Ce^{3+} ions dissolved into SmCoIn$_5$. The RKKY interaction dominates for $x \geq 0.9$ which leads to long-range magnetic ordering of Sm^{3+} ions.

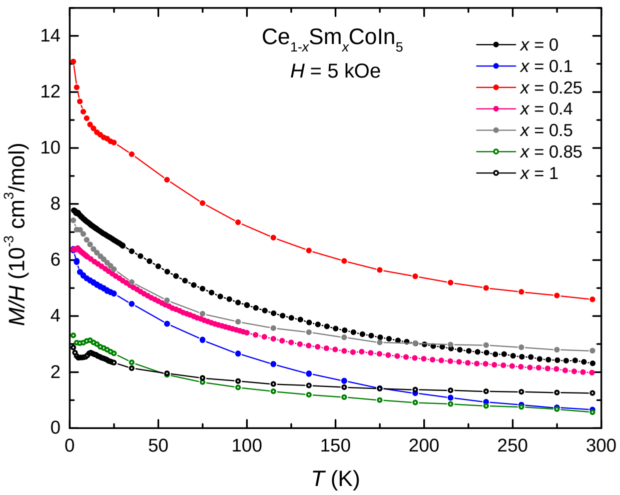

Figure 4.5. Magnetization, M/H, vs. temperature, T, measured in an applied magnetic field $H = 5$ kOe. The magnetic field was oriented parallel to the *ab*-plane.

4.3.3 Magnetization

Magnetization measurements were performed on single crystals in the $Ce_{1-x}Sm_xCoIn_5$ system with an applied magnetic field $H = 5$ kOe oriented parallel to the *ab*-plane; $M(T)/H$ data are shown in Fig. 4.5 for representative samples. This behavior is consistent with a Curie-Weiss law, shown in Eq. 4.1, for temperatures above $\sim$ 50 K.

$$\frac{M}{H} = \frac{C}{T - \theta_{CW}} \tag{4.1}$$

It is challenging to perform a Curie-Weiss analysis of our M/H data since we have two distinct magnetic species with an easy axis along the *c*-axis[83] on the Ce-rich side and perpendicular to the *c*-axis[87] on the Sm-rich side. These issues along with the likelihood of the samples hosting minor amounts of magnetic impurities contribute to the magnetic susceptibility's non-monotonic behavior with x. Therefore, we are unable to provide a detailed analysis of the evolution of the effective magnetic moment, μ_{eff}, and Curie-Weiss temperature, θ, with Sm concentration x.

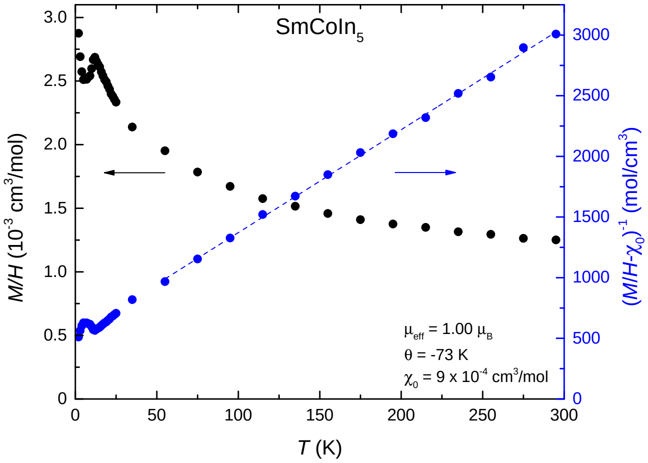

Figure 4.6. Magnetization, M/H, and $(M/H-\chi_0)^{-1}$, where χ_0 is a constant, vs. temperature, T, for SmCoIn$_5$. Best-fit values for the effective magnetic moment, μ_{eff}, Curie-Weiss temperature, θ, and χ_0 were extracted from a fit of the Curie-Weiss law to the data and are given in the panel. Features corresponding to magnetic transitions are observed at low temperatures.

A Curie-Weiss analysis of the $M(H,T)$ data for SmCoIn$_5$ is shown in Fig. 4.6. This analysis yielded an effective magnetic moment $\mu_{eff} = 1.00\ \mu_B$ and a Curie-Weiss temperature $\theta = -73$ K. The value of μ_{eff} for Sm is slightly larger than the Sm^{3+} free ion Hund's rule value of 0.84 μ_B.[93] A negative value for θ reflects the influence of AFM interactions and the Van Vleck temperature-independent contribution to $\chi(T)$.

4.3.4 Specific Heat

Specific heat measurements from 2 to 30 K are shown in Fig. 4.7. Additional measurements down to 0.5 K were also performed for selected samples with concentrations near the concentration where T_N is completely suppressed (AFM QCP) to look for non-Fermi liquid (NFL) behavior. Data for Ce$_{1-x}$Sm$_x$CoIn$_5$ and LaCoIn$_5$ single crystals for $T > 30$ K are similar, particularly the T^2 dependence of C/T which suggests that LaCoIn$_5$ is a suitable non-magnetic reference compound due to the similarity in the phonon contribution to the specific heat. The superconducting transition in CeCoIn$_5$ is

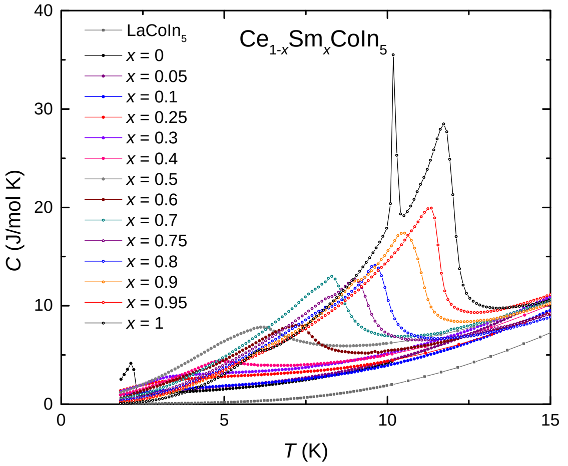

Figure 4.7. Specific heat, C, vs. temperature, T, between 2 and 30 K for Ce$_{1-x}$Sm$_x$CoIn$_5$ and a non-magnetic reference compound, LaCoIn$_5$.

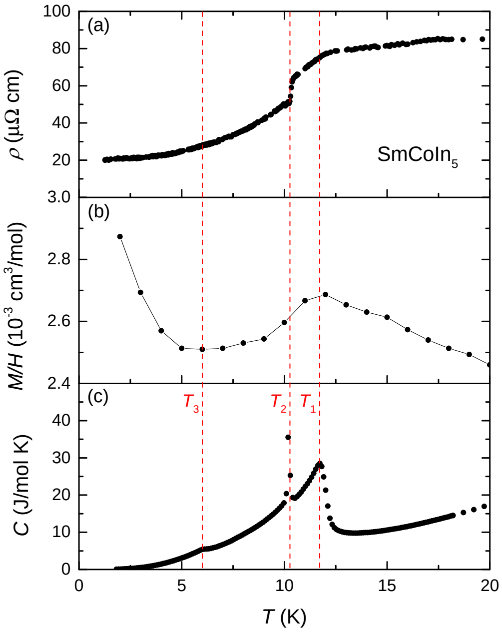

Figure 4.8. (a) Electrical resistivity, ρ, (b) magnetization divided by magnetic field, M/H, and (c) specific heat, C, vs. temperature, T, in the range $0 \leq T \leq 20$ K. Corresponding magnetic transitions can be observed in the different measurements with the vertical red dashed lines drawn through T_1, T_2, and T_3 which serve as guides to the eye.

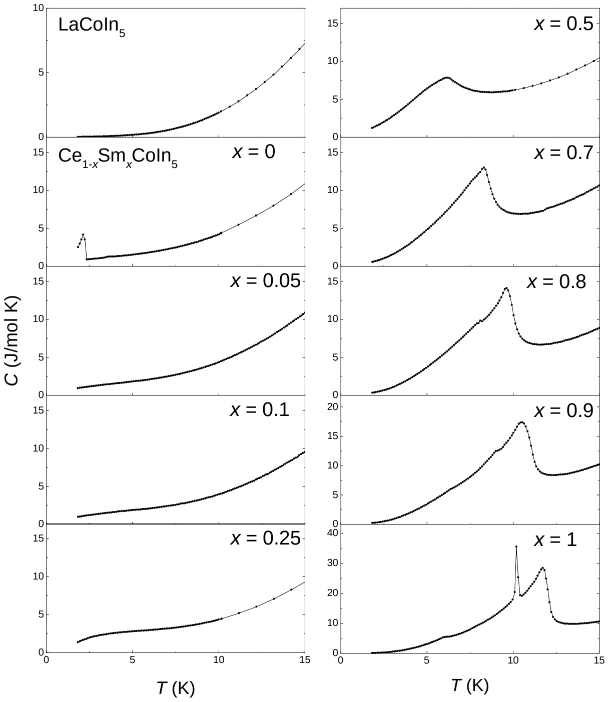

Figure 4.9. Specific heat, C, plotted vs. temperature, T, for LaCoIn$_5$ and Ce$_{1-x}$Sm$_x$CoIn$_5$ ($x = 0$, 0.05, 0.25, 0.5, 0.7, 0.8, 0.9, and 1) to demonstrate the evolution of behavior; we move from superconductivity on the Ce-rich side to antiferromagnetic order on the Sm-rich side.

observed with a sharp jump at $T_c = 2.3$ K. For Sm-rich compounds, we can identify up to three different phase transitions which are consistent with electrical resistivity and magnetization measurements as shown in Fig. 4.8; these transitions are likely associated with magnetic order, but two of them are currently unidentified as will be discussed later. The evolution of the specific heat data as we move from $x = 0$ to $x = 1$ is shown in Fig. 4.9 (where data for LaCoIn$_5$ are included for reference). These data were used to construct the phase diagram displayed in Fig. 4.4.

The highest transition temperature, T_1, is the Néel temperature, T_N, as reported by Inada *et al.* [87] As we substitute Ce into SmCoIn$_5$, we observe a continuous suppression of T_1 down to $x = 0.175$. The second temperature, T_2, is also suppressed; however, it is not suppressed at the same rate as T_1, which eventually leads to an overlap of both

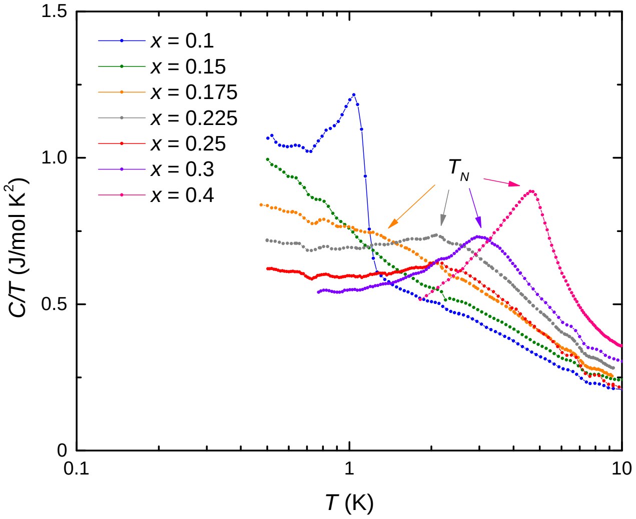

Figure 4.10. Specific heat, C, divided by temperature, T, C/T, vs. $\log(T)$ for selected Sm concentrations x near a potential AFM QCP. $C(T)/T$ exhibits a logarithmic divergence in T for $x = 0.15$, behavior that is consistent with quantum criticality. For other concentrations ($x = 0.1$, 0.175, 0.225, 0.25, 0.3, and 0.4), this behavior is not as apparent due to the proximity to their respective phase transitions, distance from the QCP, and the limited temperature range over which logarithmic behavior in T can be identified.

transition signatures. This coincidence of features indicates either that we have only one distinct transition for these concentrations, or that they cannot be separately resolved by specific heat measurements. The third characteristic temperature, T_3, only appears as a very subtle feature in the data for both $x = 0.9$ and 1 (see Fig. 4.8). For all other concentrations (including $x = 0.95$), the feature at T_3 is either too small to detect, or it disappears. It is also possible that, like T_2, this transition merges with the other magnetic transitions. As seen in the phase diagram, T_3 appears to increase with decreasing x.

Three distinct transitions have been observed in other Sm-based members of the $Sm_nM_mIn_{3n+2m}$ family of compounds (M = Rh or Ir; n = 1, 2; m = 0, 1), such as $SmIn_3$, $SmIrIn_5$, $SmRhIn_5$, Sm_2IrIn_8, and Sm_2RhIn_8.[94,91,95] It is particularly instructive to consider the compound $SmIn_3$, which is closely related to $SmCoIn_5$ (in analogy with the well-known structural relationship between $CeIn_3$ and $CeCoIn_5$). Muon spin rotation

(μSR) measurements have been performed on $SmIn_3$ to clarify the nature of the three phase transitions; the results of this study demonstrated they are all associated with magnetic ordering. [94] From specific heat data[91], we see similar features indicative of phase transitions. We conclude that $SmCoIn_5$ and $SmIn_3$ each exhibit a similar AFM transition at their highest transition temperature, T_1. The nature of the remaining two transitions at T_2 and T_3 is still unknown. From the aforementioned study on $SmIn_3$[92], there is evidence of a transition from incommensurate to commensurate AFM order at T_2; though, the shape of the specific heat feature is qualitatively different from our data presented herein. In either case, the nature of T_3 is still unknown. Additional measurements such as anomalous x-ray diffraction will need to be conducted to identify the nature of these ordered phases.

Heat capacity measurements were performed down to 0.5 K to characterize the $Ce_{1-x}Sm_xCoIn_5$ system around the potential AFM QCP. Figure 4.10 shows $C(T)/T$ data plotted on a semi-logarithmic scale for selected concentrations in the vicinity of the possible QCP near $x = 0.15$. Consistent with NFL behavior, $C(T)/T$ for $x = 0.15$ diverges logarithmically with decreasing T over a large temperature range. Neighboring concentrations do not exhibit this strong logarithmic divergence in T due to the higher values of T_c ($x = 0.1$) and T_N ($x = 0.175$, 0.225, 0.25, 0.3, and 0.4), restricting the range within which NFL behavior can reasonably be distinguished. This picture is consistent with the current phase diagram in Fig. 4.4. As we see from our measurements, SC is observed up to a concentration $x = 0.1$ where $T_c \approx 1$ K and AFM is last observed at $x = 0.175$ below $T_N \approx 1.2$ K. Despite performing measurements down to 0.5 K, we were unable to observe any additional phase transitions at the concentration $x = 0.15$. The suppression of T_c and T_N with x becomes non-linear in this concentration range; instead, SC is suppressed much more rapidly with x for $x > 0.1$, while AFM order is suppressed more rapidly with decreasing x for $x < 0.175$. From this picture, we suggest that a QCP, associated with the suppression of both the SC and AFM phases where T_c and T_N are driven to zero temperatures, lies in very close proximity to the concentration $x = 0.15$.

The apparent AFM QCP at $x_{\text{QCP}} \approx 0.15$ for $\text{Ce}_{1-x}\text{Sm}_x\text{CoIn}_5$reveals a gradual suppression of T_N with decreasing x in comparison to other substituted 115 compounds in which the AFM QCP occurs at larger values of x, such as $\text{CeCo}_{1-x}\text{Rh}_x\text{In}_5$[96,97] ($x_{\text{QCP}} \approx 0.25$), $\text{Y}_{1-x}\text{Ce}_x\text{RhIn}_5$[64] ($x_{\text{QCP}} \approx 0.65$), and $\text{La}_{1-x}\text{Ce}_x\text{RhIn}_5$[98] ($x_{\text{QCP}} \approx 0.5$). This may suggest a robust AFM phase in SmCoIn_5, supported by evidence of three distinct magnetic transitions, when compared to the AFM phase in CeRhIn_5. The measurements reported herein do not provide any evidence for the co-existence of the SCing and AFM phases associated with the Ce and Sm ions, respectively, in contrast to $\text{CeCo}_{1-x}\text{Rh}_x\text{In}_5$ at ambient pressure, in which the Ce ions are responsible for both the SC and the AFM ordering. Thus, the $\text{Ce}_{1-x}\text{Sm}_x\text{CoIn}_5$ system may fall into the class of magnetically-ordered superconductors which consist of a superconducting subsystem involving electrons associated with Ce ions that interact via the exchange interaction with a magnetically-ordered subsystem consistenting of the localized f-electrons of the Sm ions. In these types of systems, SC has been found to coexist with AFM order and to be suppressed by ferromagnetic order of localized magnetic moments.[99]

4.4 Discussion

4.4.1 Electronic and Phonon Contributions to Specific Heat

Further analysis was performed on the specific heat data for $\text{Ce}_{1-x}\text{Sm}_x\text{CoIn}_5$ using the Debye model, $C/T = \gamma + \beta T^2$. By fitting a straight line to the C/T vs. T^2 data in the temperature range $T > T_N$, we extracted best-fit values for β. We used the values of β to calculate the values of the characteristic Debye temperature, Θ_D, using the relation,

$$\beta = \frac{12\pi^4 N_A k_B}{5\Theta_D^3} \tag{4.2}$$

These results are plotted in Fig. 4.11 where Θ_D increases monotonically with x. Due to the broad features from magnetic ordering and the limited temperature range in which the Debye model is applicable, characterized by the calculated Debye temperature, it is difficult to extrapolate meaningful values of γ. We looked at two characteristic "γ" values as a general observation, one at 15 K and another at 2 K to compare to the value (γ = 53 mJ/mol K^2) from a study of SmCoIn$_5$ by Inada *et al.*[87] To do this, we extracted values for C_e/T at 2 K, where $C_e/T \equiv C/T - \beta T^2$ is the electronic contribution to the specific heat divided by temperature; we performed a similar analysis above the magnetic ordering temperature by selecting C_e/T at 15 K. The results for C_e/T are plotted in Fig. 4.11, where we observe that values for C_e/T at high and low T behave in opposite manners; at 2 K, the value of C_e/T simply decreases with x for $x \geq 0.25$ (concentrations where the AFM transition is clearly observed). This trend can be easily understood since the closer T_N is to 2 K, the larger the magnetic contribution is to C_e/T. For C_e/T at 15 K (a high-temperature, normal-state γ), we observe a similar trend with x as we did at 2 K for $x < 0.25$; however, for $x \geq 0.25$, there is a monotonic increase in C_e/T due to the introduction of the AFM transition above $x = 0.225$.

4.4.2 Entropy Calculations from Specific Heat

Entropy calculations were made using measured specific data via numerical integration of Eq. 4.3.

$$S(T) = \int \frac{C_e(T)}{T}\, dT \tag{4.3}$$

Calculations of $S(T)$ associated with magnetic ordering are compared to various

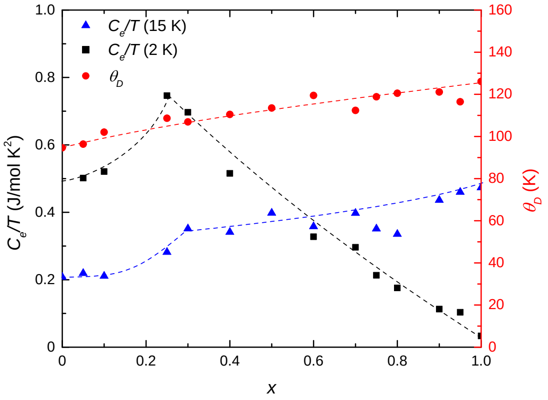

Figure 4.11. Electronic contribution to the specific heat divided by temperature, C_e/T, at 2 K (black squares), temperature-independent contribution to C_e/T at 15 K, above the magnetic ordering temperature (blue triangles), and Debye temperature Θ_D (red circles), all plotted as a function of Sm concentration x, in $\mathrm{Ce}_{1-x}\mathrm{Sm}_x\mathrm{CoIn}_5$. Dashed curves are guides to the eye. The procedures for determining the values of C_e/T at 2 K and 15 K are described in the text.

values of the entropy $R\ln(2J+1)$ in Fig. 4.12 with dashed lines for $J = \frac{1}{2}$, 1, and $\frac{3}{2}$. Concentrations exhibiting large peaks in C vs. T data ($x \geq 0.5$) show a change in slope near characteristic entropy values. For $0.5 \leq x \leq 0.8$, the entropy associated with magnetic ordering is around $R\ln 2$. For Sm-rich concentrations ($x \geq 0.9$), the change in entropy is about $R\ln 3$; we have already described a cross-over in behavior of the electrical resistivity data that also occurs near $x \approx 0.9$ (see Fig. 4.3).

4.4.3 Non-Fermi Liquid Behavior in Low-Temperature Electrical Resistivity

Low-temperature electrical resistivity, $\rho(T)$, data in the paramagnetic state are often fitted using a power-law function of the usual form:

$$\rho = \rho_0 + AT^n \tag{4.4}$$

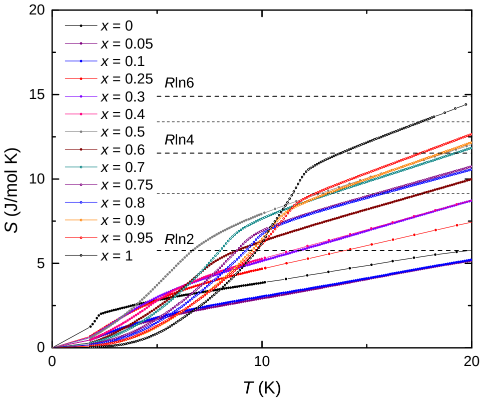

Figure 4.12. Electronic entropy, $S(T)$, calculated as described in the text, plotted vs. temperature, T. Dashed lines showing $R\ln(2J+1)$ at various values of total angular momentum J are provided for comparison.

Due to errors in the geometrical factor A/L (A = cross-sectional area, L = length) used to convert electrical resistance R to electrical resistivity $\rho = R(\frac{A}{L})$, the following equation was fitted to the normalized resistivity, $\rho(x,T)/\rho(300\text{ K})$, data:

$$(\rho - \rho_0)/\rho(300\text{ K}) = A'T^n \tag{4.5}$$

where $A' = A/\rho(300\text{ K})$.

Exponents, n, that are sub-quadratic, indicative of NFL behavior, were observed to develop in the $0 \le x \le 0.5$ concentration region. This fitting procedure is reasonable around the projected QCP near $x = 0.15$; however, due to the proximity to the SCing and magnetically-ordered phases, the temperature range in which this fit can be achieved is very small. By plotting $\log[(\rho - \rho_0)/\rho(300\text{ K})]$ vs. $\log T$ (see Fig. 4.13), we observed a linear region which corresponds to a constant value of n. Extracting n as the slope of the line in these plots, we plotted $\rho_0/\rho(300\text{ K})$, A', and n vs. x to characterize the behavior of the electrical resistivity around the QCP as shown in Fig. 4.14. We observe a decreasing NFL exponent of $n \approx 1$ at $x = 0$ to $n \approx 0.13$ at $x = 0.15$ before n returns to

$n \approx 1$ as x increases beyond the QCP near $x = 0.15$. The normalized residual resistivity, $\rho_0/\rho(300\ \mathrm{K})$, increases steadily as a function of x, likely due to the increasing number of magnetic ions introduced via Sm substitution. The normalized coefficient, $A'(x)$, shows a sharp cusp near the QCP, which is indicative of NFL behavior. The behavior of $n(x)$ is consistent with quantum critical behavior where proximity to a QCP in the normal state results in a departure of the physical properties from Fermi-liquid behavior where $n = 2$. The residual resistivity, $\rho_0(x)$, and the coefficient, $A(x)$, can be determined by multiplying the normalized residual resistivity, $\rho_0(x)/\rho(x, 300\ \mathrm{K})$, and normalized coefficient, $A'(x) = A(x)/\rho(x, 300\ \mathrm{K})$, by the value of $\rho(x, 300\ \mathrm{K})$ determined by making a least-squares fit of the relation $\rho(x, 300\ \mathrm{K}) = \rho(0, 300\ \mathrm{K}) + \alpha x$ to the $\rho(x, 300\ \mathrm{K})$ data. This fit yields the values $\rho(0, 300\ \mathrm{K}) = 0.21 \pm 0.19$ mΩ-cm and $\alpha = 2.23 \pm 0.80$ mΩ-cm. The errors reflect the scatter in the measured values of $\rho(x, 300\ \mathrm{K})$, which are partially due to uncertainties in the geometrical factor used to convert $R(T)$ to $\rho(T)$.

The power-law behavior of the electrical resistivity in this system is consistent with a previous study of other $\mathrm{Ce}_{1-x}R_x\mathrm{CoIn}_5$ systems (R = Yb, Y, Lu, Er, Dy, Gd) by Paglione *et al.*[100], in which values of $n \lesssim 1$ were found for various R substituents. Furthermore, an inverse proportionality between n and ρ_0 for each R ion was found, similar to what we have observed in the $\mathrm{Ce}_{1-x}\mathrm{Sm}_x\mathrm{CoIn}_5$ system.

4.5 Concluding Remarks

Based on powder x-ray diffraction, electrical resistivity, magnetization, and specific heat measurements on $\mathrm{Ce}_{1-x}\mathrm{Sm}_x\mathrm{CoIn}_5$ single crystals, we constructed a T vs. x phase diagram for this system. As Sm is substituted for Ce, we observe a crossover from superconductivity on the Ce-rich side to antiferromagnetism and other types of order whose origin is currently unknown on the Sm-rich side. We observed NFL behavior consistent with quantum criticality in the intermediate region $0.1 < x < 0.225$. There

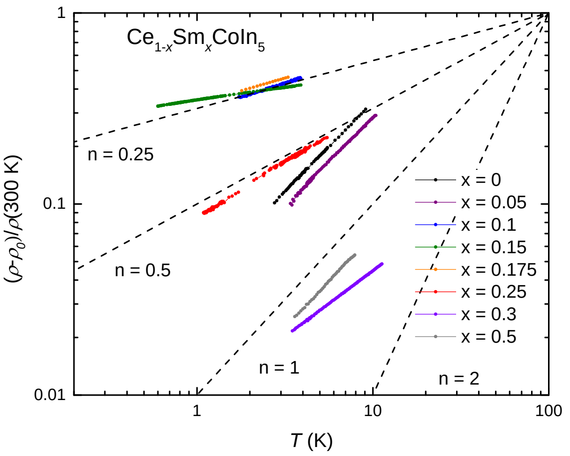

Figure 4.13. Plot of $\log[(\rho-\rho_0)/\rho(300\text{ K})]$ vs. $\log T$ for $\mathrm{Ce}_{1-x}\mathrm{Sm}_x\mathrm{CoIn}_5$ $(0 \leq x \leq 0.5)$ up to $T \approx 15$ K. Linear behavior indicates power-law behavior given by Eq. 4.5. Dashed lines are provided at exponents of n = 0.5, 1, and 2 as guides to the eye.

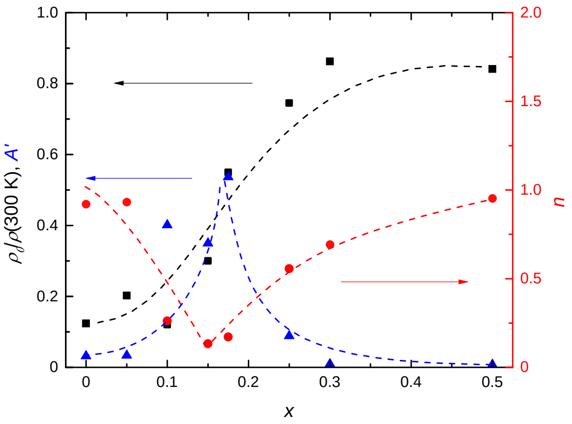

Figure 4.14. Normalized residual resistivity $\rho_0/\rho(300\text{ K})$ (black), normalized coefficient A' (blue), and exponent n (red) vs. Sm concentration x for $\mathrm{Ce}_{1-x}\mathrm{Sm}_x\mathrm{CoIn}_5$. The values of $\rho_0/\rho(300\text{ K})$, A', and n were extracted from fits of Eq. 4.5 to the $\rho(x,T)$ data in Fig. 4.13.

appears to be an AFM QCP in the vicinity of $x = 0.15$ with no indication of coexistence of SC and AFM. An evolution from Kondo coherence to single-ion Kondo behavior and then eventually to magnetic ordering via the RKKY interaction (and other types of order) occurs as x increases from 0 to 1. Since Sm has a high neutron absorption cross-section making it unsuitable for neutron scattering measurements, further studies into this compound using techniques such as anomalous x-ray diffraction will be necessary to elucidate the nature of magnetic order in the $\mathrm{Ce}_{1-x}\mathrm{Sm}_x\mathrm{CoIn}_5$ system.

Acknowledgements

Research at the University of California San Diego was supported by the U.S. Department of Energy, Office of Basic Energy Sciences, Division of Materials Science and Engineering under Grant No. DE-FG02-04-ER46105 (materials synthesis and characterization) and the U.S. National Science Foundation under Grant No. DMR-1206553 (low temperature measurements). Research at Kent State University was supported by the U.S. National Science Foundation under Grant No. DMR-1505826 (low temperature specific heat measurements).

Chapter 4, in full, is a reprint of the material as it appears in Physical Review B (2018). Pouse, N., Jang, S., White, B. D., Ran, S., Adhikari, R. B., Almasan, C. C., Maple, M. B., APS, 2018. The dissertation author was the primary investigator and author of this paper.

Chapter 5

Angular-dependent magnetoresistance measurements on the $URu_{2-x}Fe_xSi_2$ system

We explored the role of angle, θ, as a tuning parameter in the correlated electron system $URu_{2-x}Fe_xSi_2$, where θ is the angle between magnetic field, H, and the c-axis. To accomplish this, we performed electrical transport measurements on single crystals of $URu_{2-x}Fe_xSi_2$ in high magnetic fields at several temperatures, T, to construct an angle-dependent phase diagram. The goal of this investigation was to observe whether θ becomes a tuning parameter as Fe substitution increases and the system is driven toward large-moment antiferromagnetic order (LMAFM) which can help distinguish the HO and LMAFM phases in $URu_{2-x}Fe_xSi_2$. Measurements on $R(\theta)$ at $\mu_0 H = 20$, 33, 40, and 45 T were conducted in the temperature range $0.33 \leq T \leq 20$ K and showed θ-dependent behavior in the various phase transitions of $URu_{2-x}Fe_xSi_2$ ($HO^{(*)}$, LMAFM, SDW, Fermi surface, etc.). These phase transitions were plotted in a phase diagram of T vs. $H//c$ for multiple x which showed that $H//c$, not θ, is a tuning parameter of $URu_{2-x}Fe_xSi_2$ throughout all Fe concentrations. These findings provide more evidence for the similarity between the HO and LMAFM phases, as well as an alternate perspective on the relationship between the LMAFM and re-entrant HO* phase.

5.1 Introduction

The heavy fermion superconductor URu_2Si_2 has been a topic of significant interest in the field of correlated electron systems due to its so-called “hidden order” (HO) phase, whose nature and the identity of its order parameter have eluded researchers for decades.[101] In particular, the HO has been studied extensively via tuning of non-thermal parameters such as pressure, P,[102] magnetic field, H,[103] and chemical substitution, x, like in $URu_{2-x}M_xSi_2$ (where M = Fe,[22] Os,[104] Re,[105] etc.).

In particular, studies on the system $URu_{2-x}Fe_xSi_2$ can probe the nature of the HO, since $URu_{2-x}Fe_xSi_2$ transitions to a large-moment antiferromagnetic (LMAFM) phase through increasing the Fe concentration, with the LMAFM first appearing at $x = 0.15$ at ambient pressures.[22] This phase can also be induced under the application of pressure ($P_c = 0.8$ GPa) at $x = 0$.[102] These two methods of introducing LMAFM can even be combined, suggesting that Fe-substitution is akin to a “chemical pressure”.[20,19,21] This also means that measurements which are difficult to perform on URu_2Si_2 under pressure can instead be performed on $URu_{2-x}Fe_xSi_2$ with an equivalent chemical pressure in order to accomplish the same result. Also, the LMAFM phase observed in $URu_{2-x}Fe_xSi_2$ under both applied pressure and Fe-substitution is specifically intriguing due to the similarities it has with the HO phase.[106,107] Both the HO and LMAFM phases have been further explored through the application of high magnetic field,[23] where a “re-entrant” hidden order (HO*) was even observed as large magnetic field was applied at low temperatures of the LMAFM phase.[108,109,23] With the continuing efforts to understand the underlying physics of the HO, a crucial endeavor would be to probe the field-induced transition between the HO and the LMAFM phases for several x in $URu_{2-x}Fe_xSi_2$.

One such effort to characterize the HO by Kanchanavatee *et al.* was the attempt to study what appeared to be an introduction of higher-order angular symmetry in magnetoresistance, $R(\theta)$, of URu_2Si_2 under applied field of H up to 9 T, directed at an angle θ with respect to the c-axis (see Fig. 5.1), as the temperature, T, was lowered through the HO transition ($T_{HO} = 17.5$ K).[24] In this study, the magnetoresistance of URu_2Si_2 was measured as a function of θ for various temperatures ranging from 1.8 K to well above T_{HO}. The magnetoresistance, $R(\theta)$, could be apparently fit to a Fourier series, according to Eq. 5.1:

$$R(\theta) = R_0 + A_2 \cos 2\theta + A_4 \cos 4\theta + ... + A_{2n} \cos 2n\theta, \tag{5.1}$$

where A_{2n} represents the Fourier coefficient of the $2n$-fold angular symmetry term and A_2 represents the inherent two-fold symmetry of magnetoresistance since the resistivity along the *ab*-plane is lower than the resistance along the c-axis for $H > 0$. Introduction of higher-order symmetry due to the HO transition would therefore appear as significant increases in the coefficients of the four-fold and higher symmetry terms (A_4, A_6, etc.). The study showed jumps in the 4, 6 and 8-fold symmetry terms as URu_2Si_2 went through the HO transition; however, the reason for this could not be explained.

A potential explanation for this angle-dependent behavior is outlined for the parent compound URu_2Si_2 in Ref. 25. Scheerer *et al.*. report on electrical resistivity measurements of URu_2Si_2 in high magnetic fields applied at angle θ to the c-axis and characterized its various phase transitions as a function of θ. The ultimate finding was that the observed θ-dependent behavior of the T vs. H phase diagram of URu_2Si_2 is actually a reflection of the phase transitions depending on the magnetic field projection onto the c-axis, where $H//c = H\cos\theta$. This study showed that neither H nor θ independently are tuning parameters of URu_2Si_2, but instead $H//c$ is the tuning parameter, possibly due to the symmetry of the g-factor of URu_2Si_2.[110,111]

Our primary motivation for the study presented herein was to continue to char-

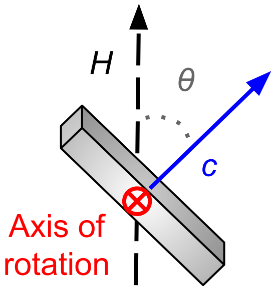

Figure 5.1. Graphic of the sample rotation in a vertical magnetic field representing the experimental setup at both the Pulsed Field facility at LANL and the DC Field facility at FSU.

acterize the θ-dependent behavior of R for several x in URu$_{2-x}$Fe$_x$Si$_2$. We wanted to determine whether the fact that $H//c$ is a tuning parameter remains true across the range of Fe concentrations, x, or perhaps θ may become a tuning parameter since the introduction of Fe in URu$_{2-x}$Fe$_x$Si$_2$ can induce the LMAFM phase. Additionally, these measurements can help probe the transition between LMAFM and HO* ("re-entrant HO"), as well as potentially allowing us to distinguish the closely-related LMAFM and HO ground states. These motivations can be explored by constructing a T vs. H phase diagram for URu$_{2-x}$Fe$_x$Si$_2$, as presented in the work by Ran *et al.*,[23] but with variation of θ. Our construction of the URu$_{2-x}$Fe$_x$Si$_2$ phase diagram with varying T, H, and θ, not only confirmed the results for URu$_2$Si$_2$ presented by Scheerer *et al.*,[25] but also showed that $H//c$ being a tuning parameter, as opposed to θ, was a phenomenon that extended throughout all x in URu$_{2-x}$Fe$_x$Si$_2$.

5.2 Results

Electrical transport measurements on single crystals of URu$_{2-x}$Fe$_x$Si$_2$ were made under high field on the 65 T pulsed-field magnet at National High Magnetic Field Lab (NHMFL), Los Alamos, NM and on the 45 T dc hybrid magnet at NHMFL, Tallahassee, FL. The electrical transport properties of the single crystals, with cleaved surfaces perpendicular to the *c*-axis, were measured using a standard four-wire technique in the *ab*-plane, where voltage was measured in the same direction as current. The magnetic field, H, is applied at an angle, θ, to the *c*-axis, such that $\theta = 0$ represents $H//c$ and $\theta = 90^\circ$ represents $H//ab$. Figure 5.1 shows a depiction of this setup at both facilities.

5.2.1 Angular-dependent magnetoresistance measurements on the $URu_{2-x}Fe_xSi_2$ system

Measurements of the electrical transport properties of URu_2Si_2 were taken under a pulsed field of $\mu_0 H_{max} = 65$ T directed at various angles $0 \leq \theta \leq 90^\circ$ for $T = 1.5$, 10, and 13 K. The results of these measurements are presented in Fig. 5.2(a-c). Electrical resistance, R, of URu_2Si_2 is measured as H is pulsed to 65 T, and several features associated with phase transitions appear at various values of H_{phase}, dependent on T and θ. For fixed T, the θ-dependent behavior as $\theta \rightarrow 90^\circ$ shows these transitions being shifted to higher fields, suggesting strong correlation between H_{phase} and θ, where $\theta = 90^\circ$ makes these transitions impossible to observe. We follow this idea by using the trigonometric relation, $\cos\theta$, which represents the projection of H onto the *c*-axis, and can reduce the scaling of H by $\cos\theta$ on the bottom panels of Fig. 5.2(d-f) to determine if the transitions observed in URu_2Si_2 are dependent on $H//c$. This reduced scaling, based on the geometry of the setup, shows that the transitions observed in URu_2Si_2 are indeed solely dependent on the application of magnetic field along the *c*-axis. Despite a very large $\mu_0 H$ up to 65 T being applied in the *ab*-plane, there is no deviation from this behavior. These results confirm the findings of Scheerer *et al.* and give strong indication that not only the HO, but all phases (Fermi surface reconstruction, spin-density wave, etc.) in URu_2Si_2 are only susceptible to H applied along the *c* axis, suggesting that the magnetic properties of the $5f$-electrons are linked to that of the Fermi surface.[25]

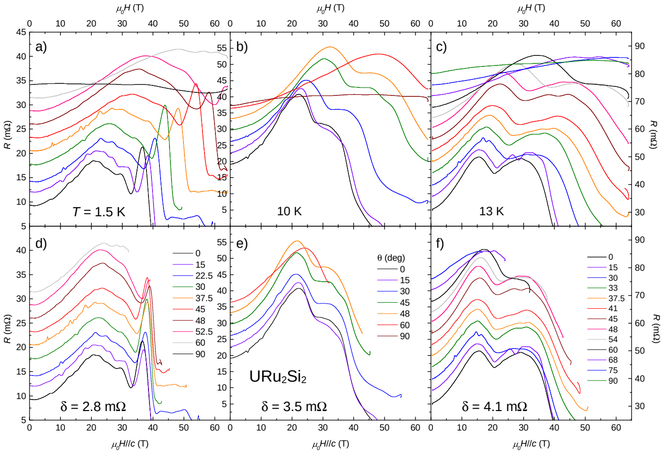

Figure 5.2. (a-c) Resistance, R, vs. magnetic field, H, of URu_2Si_2 at multiple angles θ for T = 1.5, 10, and 13 K, respectively. (d-f) Resistance curves from (a-c) plotted versus the projection of the magnetic field onto the c-axis of URu_2Si_2, $H//c$, where $H//c = H\cos\theta$. The behavior of magnetoresistance in URu_2Si_2 appears to only depend on $H//c$, consistent with Scheerer *et al.*[25]

5.2.2 Magnetoresistance versus θ in $URu_{2-x}Fe_xSi_2$

In an effort to further understand the study on URu_2Si_2 by Kanchanatavee *et al.*[24], measurements of R vs. θ were performed on $URu_{2-x}Fe_xSi_2$ in the 45 T hybrid magnet at NHMFL to characterize the angular symmetry of $R(\theta)$ at higher fields and across the phase diagram for $URu_{2-x}Fe_xSi_2$ constructed by Ran *et al.*[23] Measurements on $R(\theta)$ were made as θ was swept through the range $0 \leq \theta \leq 180^\circ$ for fixed magnetic fields $\mu_0H = 20$, 33, 40, and 45 T at multiple temperatures above and below the HO and LMAFM transitions in $URu_{2-x}Fe_xSi_2$ for selected x. The data taken for this measurement on $x = 0.2$ at $\mu_0H = 45$ T are shown in Fig. 5.3 as an example. As T is lowered below T_{LMAFM}, the $R(\theta)$ data appear to develop higher-order angular symmetry which could be fit to Eq. 5.1. This analysis is consistent with the previous study on just the parent compound URu_2Si_2;[24] however, it is difficult to explain due to the unknown nature of the symmetry.

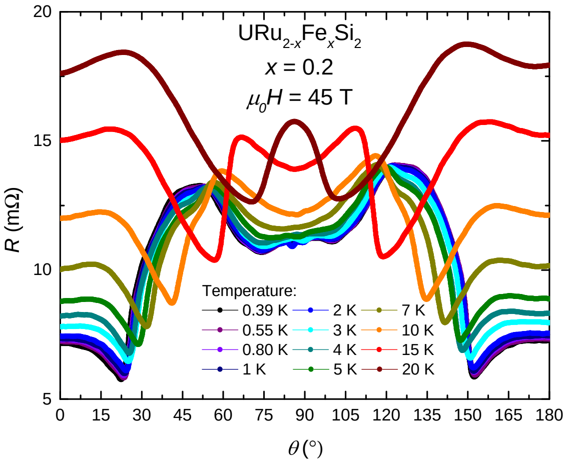

Figure 5.3. Select R vs. θ curves at select temperatures for $x = 0.2$ with the applied field magnitude of $\mu_0 H = 45$ T. Initially believed to be reflection of symmetry developing in the LMAFM phase of $\mathrm{URu}_{2-x}\mathrm{Fe}_x\mathrm{Si}_2$, but instead appears to be development of features at high fields representing phase transitions occurring at $\theta_c(T,H)$.

An alternate, more reasonable analysis is that the features in $R(\theta)$, which initially appear to be associated with higher-order angular symmetry in the magnetoresistance, are actually representative of phase transitions. This explanation utilizes the knowledge that the T vs. H phase diagram for $\mathrm{URu_2Si_2}$ does not explicitly depend on the angle, but instead on the projection of H onto the c-axis, as shown by Scheerer *et al.*[25] and confirmed in the prior discussion in this manuscript using an independent, but similar experiment on $\mathrm{URu_2Si_2}$. Much like in Fig. 5.2, where the magnetic field sweeps of $R(H)$ at several θ were reduced to a system of just R vs. $H//c$, a reduction of parameters can be attempted where θ is converted to $H//c$ using the magnitude of the field (45 T, for Fig. 5.3) and the relation $H//c = H\cos\theta$. This conversion is shown for a single R vs. θ dataset in Fig. 5.4, with x-axis values of θ being converted to $H//c$ and shown on the top x-axis. Using the first angular derivative of resistance, dR/dθ, the features in $R(\theta)$ can be more easily identified at specific θ and $H//c$, as shown by the red line in Fig. 5.4.

The features, identified by sharp peaks in dR/dθ, were plotted in phase diagrams

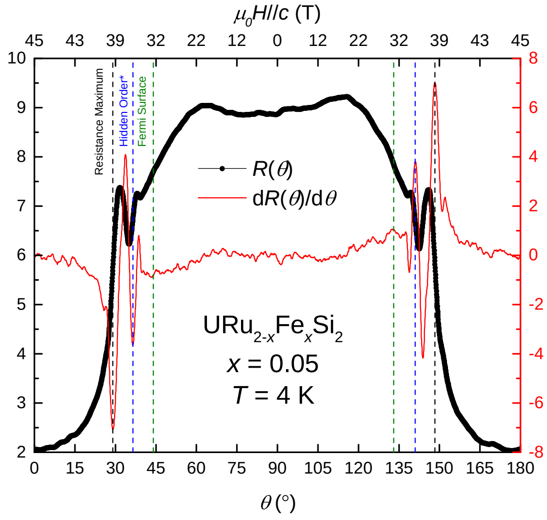

Figure 5.4. Single R vs. θ curve (black) for $x = 0.05$ at $T = 4$ K with its angular derivative dR/dθ as an overlay (red). Sharp features in the derivative data at specific θ can be converted to $H//c$ (top x-axis). This reduction of H and θ into $H//c$ shows that these features actually correspond to phase transitions which were previously mapped out by Ran *et al.*[23]

for all T and H, for several x, with no guidance from prior studies. The phase diagrams constructed from these data are shown in Fig. 5.5. The newly constructed phase diagram shows a remarkable similarity to the phase diagrams explored by Ran *et al.*,[23] suggesting that like in URu$_2$Si$_2$, the T vs. H phase diagrams for URu$_{2-x}$Fe$_x$Si$_2$ are strictly dependent on $H//c$ and exhibit no angle-dependent behavior. Overlap in the T vs. $H//c$ phase diagram confirms no angle-dependence of the phases by noting that an increase in field magnitude H does not change the anisotropy. This is particularly insightful, as one would expect that perhaps the LMAFM phase of URu$_{2-x}$Fe$_x$Si$_2$ could be perturbed by a large magnetic field being applied along the *ab*-plane. Instead, it is shown, that no matter the Fe concentration of URu$_{2-x}$Fe$_x$Si$_2$, all field-induced phase transitions in this system happen along the c-axis and may be closely intertwined. Further, the inability to show a difference in the anisotropy between the HO and LMAFM phases using this measurement technique represents a significant finding.

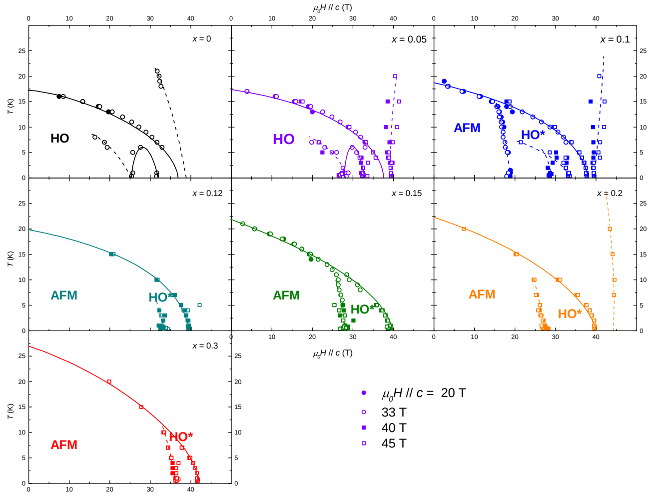

Figure 5.5. A T vs. $H//c$ phase diagram is constructed for several x using extracted values of $\theta(T,H)$ from various $R(\theta)$ curves using the method shown in Fig. 5.4. The phase diagrams presented show shocking similarity to what was mapped out by Ran *et al.*,[23] suggesting that various phases in $\text{URu}_{2-x}\text{Fe}_x\text{Si}_2$ are only susceptible to H along the c-axis.

In the phase diagram we show, for samples with Fe concentration $x \geq 0.1$, that the LMAFM ground state transitions into re-entrant HO as H is increased, which is expected from prior studies on re-entrant HO in $\text{URu}_{2-x}\text{Fe}_x\text{Si}_2$.[23] Since our measurements yielded a large amount of data in a T vs. H vs. x phase diagram, and the reduction of θ and H into $H//c$ provides redundancies in this phase diagram, we can thoroughly explore the phase boundary between LMAFM and HO*. One such visualization is presented in Fig. 5.6, where, for $x = 0.1$ at $\mu_0 H = 33$ T, we can show the signatures of the LMAFM and HO* transitions in dR/dθ. As expected, at higher temperatures, there is only a LMAFM phase before transitioning into the normal state, but as the temperature is lowered, a transition to HO* is observed at high fields.

The interesting behavior shown in Fig. 5.6 is the smooth nature of the transition from the normal state to HO* or LMAFM as a function of T. The normal state boundary traces out continuously with T from the LMAFM to the HO* phases for the Fe concentra-

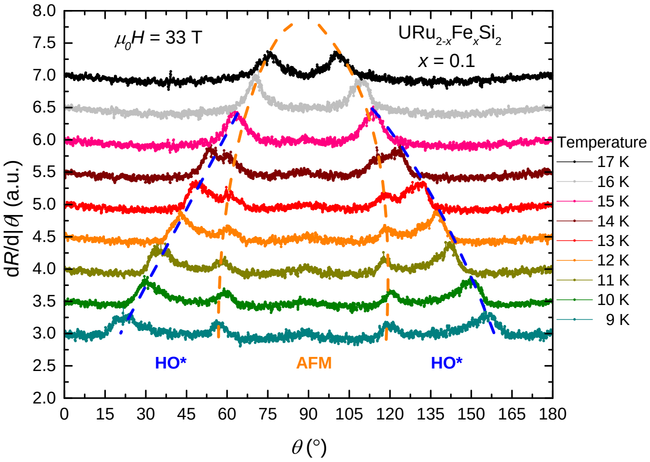

Figure 5.6. Demonstration of the LMAFM and HO* signatures in dR/dθ data for $x = 0.1$ at $\mu_0 H$ = 33 T as HO* comes into the fold at lower temperatures. This picture is consistent with the idea that the LMAFM phase is interrupting the larger HO phase.

tions where both phases are observed. The transition between HO* and LMAFM is very abrupt, however, and its behavior may lend insight into the nature of the LMAFM phase. A possible scenario is that the substitution of Fe is actually "interrupting" the HO phase, rather than a separate re-entrant HO phase "growing out" of the LMAFM ground state. This idea may be supported by characterizing the shape of the outer boundary of the phase diagrams: HO for $x = 0$ and 0.05, LMAFM + HO* for $x = 0.1$, 0.12, 0.15, 0.2, and 0.3, and LMAFM for presumably $x > 0.3$. This characterization is presented in Fig. 5.7, much like what was done by Ran *et al.*,[23] where the phase boundaries are normalized to 1 at the T and H endpoints, such that the qualitative behavior of the boundary can be observed and characterized according to Eq. 5.2. Using this fitting of the curvature, the data can be organized into essentially 3 clusters. The first cluster, where fitting parameter $n = 1.8$, is the same as observed by Ran *et al.*[23], and applies to $x = 0$, 0.05, and 0.1 where HO is the dominant phase. The second cluster represents a flatter boundary where LMAFM is the dominant phase and $n = 1.45$ for $x = 0.15$, 0.2, and 0.3. This suppression of n may be related to the fact that T_0 increases significantly between $x = 0.1$ and 0.15.

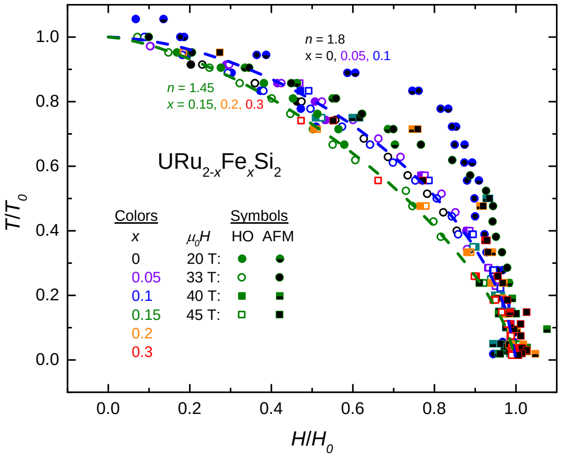

Figure 5.7. Normalized T/T_0 vs. H/H_0 phase boundary for both LMAFM and HO(*) phases for all x and H. Curvature of this boundary is analyzed using Eq. 5.2, showing two clusters for the HO(*) phases: $n = 1.8$ for $x = 0$, 0.05, and 0.1 where HO is the dominant phase and $n = 1.45$ for $x = 0.15$, 0.2, and 0.3 where LMAFM is the dominant phase. As expected, the AFM boundary does not fit into this smooth curve due to the abrupt nature of the transition into HO*.

The final cluster is a more general grouping where this boundary was mapped out to where $H_0 = H_{\mathrm{LMAFM}}$, instead of the usual H_{HO}. As discussed, the LMAFM phase cuts into the HO phase rather abruptly, yielding a phase boundary which is not smooth and therefore cannot be cleanly fit to Eq. 5.2.

$$(T/T_0)^n + (H/H_0)^n = 1 \tag{5.2}$$

Further visualization of the behavior of the LMAFM/HO* to normal state boundary is provided in the 3D phase diagram shown in Fig. 5.8, with the color of the data points corresponding to the various phases in $\mathrm{URu}_{2-x}\mathrm{Fe}_x\mathrm{Si}_2$. The transition from the normal state to LMAFM/HO* follows a continuous boundary with x, whereas the HO* to LMAFM boundary cuts in abruptly. This LMAFM to HO* transition “wedge” in the 3D phase diagram cuts in at an angle such that it eventually converges with the HO* boundary at $x \geq 0.3$, but near $x = 0.1$, this boundary rapidly disappears as the

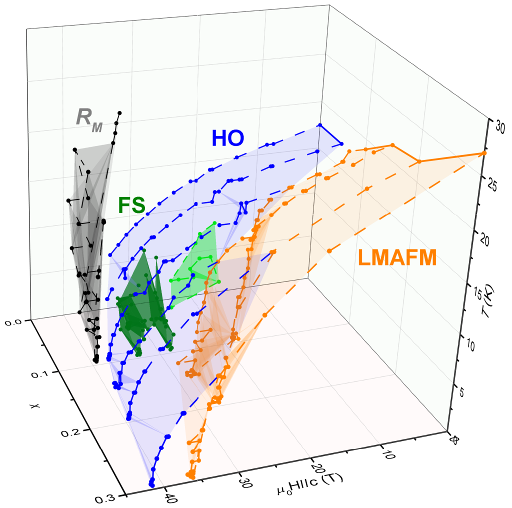

Figure 5.8. 3D phase diagram combining all of the 2D phase diagrams from Fig. 5.5, except for $x = 0.12$, due to likely discrepancy in the Fe concentration. In 3D space, the joint LMAFM-HO boundary appears to curve smoothly in a consistent matter, with the only variation being where the AFM phase cuts in at higher T based on x.

URu$_{2-x}$Fe$_x$Si$_2$ system moves into a HO-only regime. The 3D phase diagram reflects the possible explanation that Fe-substitution leads to an abrupt interruption of the HO phase via introduction of the LMAFM phase at $\mu_0 H = 0$ T. As Fe continues to be substituted into URu$_{2-x}$Fe$_x$Si$_2$, the space in the phase diagram previously occupied by the HO phase is quickly replaced by LMAFM. One can picture a tall "dome" of LMAFM growing into a large "bubble" of HO in this 3D phase diagram. While no angular-dependent behavior is clearly observed in this phase diagram, the data collected from our measurements show a more detailed picture of the interaction between the LMAFM and HO phases in the URu$_{2-x}$Fe$_x$Si$_2$ system.

5.3 Concluding Remarks

We performed a series of measurements on URu$_{2-x}$Fe$_x$Si$_2$ in order to both characterize the T vs. H phase diagram as a function of θ, the angle between H and the *c*-axis, and to further study the introduction of the high-order angular-symmetry of magnetoresistance $R(\theta)$ of the HO and LMAFM phases in order to better understand the nature of both phases, which was initially explored in $\mathrm{URu_2Si_2}$.[24] We show that these two studies are actually probing the same phenomenon, which is that the phases in the T vs. H phase diagram are strictly dependent on the magnetic field applied along the *c*-axis, $H//c$. The reduction of these two seemingly independent problems to a single phenomenon was allowed when magnetoresistance $R(H)$ curves at various θ for fixed T could be understood as being independent of θ by converting H into its *c*-axis projection, such that $H//c = H\cos\theta$. This characterization of the phases as a function of $H//c$ was initially provided by Scheerer *et al.*[25] and then separately verified with our own measurements on $\mathrm{URu_2Si_2}$. By applying this technique to the substitution study in $\mathrm{URu_{2-x}Fe_xSi_2}$, the phase diagram behavior could be reduced by converting values of θ at fixed H to an equivalent $H//c$. After construction of the 2D phase diagram for several x, we found recovery of the original 2D phase diagrams constructed by Ran *et al.*[23], where H was strictly parallel to c, suggesting that, despite large H being applied along the *ab*-plane, potentially causing perturbations to the T vs. H phase diagram, the various phases in $\mathrm{URu_{2-x}Fe_xSi_2}$ are resistant to magnetic fields $H//ab$, and that phenomena such as HO, LMAFM, Fermi surface reconstruction, SDW, etc. are all exclusively dependent on $H//c$. This suggests that these various phases are closely related to each other, with $H//c$, and not H or θ, being a non-thermal tuning parameter. Further, we can continue to observe the x-dependence of these various phases in $\mathrm{URu_{2-x}Fe_xSi_2}$ to provide further insight into their nature, particularly the HO and LMAFM. By studying the characteristics of the various phase boundaries, we can actually imagine an explanation of the relationship between HO(*) and LMAFM, where LMAFM is interrupting the continuous HO phase, as a potential alternative explanation to the idea that re-entrant HO* grows out of LMAFM at high fields. Thus, this study potentially offers two new insights into $\mathrm{URu_{2-x}Fe_xSi_2}$:

(1) not only are the phases in the parent URu_2Si_2 solely dependent on $H//c$,[25] but so is $URu_{2-x}Fe_xSi_2$ despite the introduction of LMAFM via Fe-substitution (this also provides a clear explanation for the observed "symmetry" in $R(\theta)$ for $\mu_0 H \geq 0$ T)[24] and (2) we provide an additional visualization of the T vs. H phase diagram for several x, allowing for an alternate explanation of the interaction between HO and LMAFM induced via Fe-substitution.

Acknowledgements

Research at UCSD was supported by the NNSA through the U.S. DOE under Grant No. DE-NA0002909, by the DOE under Grant No. DEFG02-04-ER46105, and by the NSF under Grant No. DMR 1206553. A portion of this work was performed at the National High Magnetic Field Laboratory, which is supported by National Science Foundation Cooperative Agreement No. DMR-1157490 and the State of Florida. This research was also funded in part by a QuantEmX grant from ICAM and the Gordon and Betty Moore Foundation through Grant No. GBMF5305 to Hector D. Rosales.

Chapter 5, in part is currently being prepared for submission for publication of the material. Pouse, N., Ran, S., Graf, D., Lai, Y., Singleton, J., Balakirev, F. F., Baumbach, R. E., Maple, M. B. The dissertation author was the primary investigator and author of this material.

Chapter 6

Concluding Remarks

In this dissertation, we show several methods of surveying correlated electron systems through chemical substitution. In lanthanide- and actinide-based compounds, f-electron hybridization often yields phenomena such as heavy fermion behavior, the Kondo effect, unconventional superconductivity, magnetic ordering, and quantum criticality. Developing a better understanding of when and why these phenomena occur is crucial to bridging the gap between theory and experimental results in condensed matter physics.

In Chapter 2, we present a study on the system $\mathrm{Yb}_{1-x}\mathrm{Sc}_x\mathrm{Co}_2\mathrm{Zn}_{20}$, which is known to exhibit abnormally heavy fermion behavior and the Kondo effect. Prior studies by Saiga *et al.* show that applying pressure on the parent compound $\mathrm{YbCo}_2\mathrm{Zn}_{20}$ can drive it through a quantum critical point and into a magnetically ordered state.[13] By substituting Sc for Yb, we decreased the size of the unit cell and hoped to apply a chemical pressure without affecting the underlying magnetism since Sc is nonmagnetic. Instead, what we find is that low amounts of Sc surprisingly change the valence behavior of Yb, and with sufficient Sc substitution, the magnetic properties of $\mathrm{Yb}_{1-x}\mathrm{Sc}_x\mathrm{Co}_2\mathrm{Zn}_{20}$ are significantly decreased. These results are apparent in the characterization of the lattice parameters $a(x)$, the strength of the Kondo effect, and the magnetization. This, in conjunction with other studies on Yb-based heavy fermion systems would suggest that Yb is highly susceptible to changes in valence through chemical substitution no matter if it is being replaced by other lanthanides, or a nonmagnetic rare earth element. A more detailed study on this system with a direct measurement of the Yb valence would help in identifying the specifics of the valence behavior. Additionally, more measurements on the electronic structure of $\mathrm{Yb}_{1-x}\mathrm{Sc}_x\mathrm{Co}_2\mathrm{Zn}_{20}$ could further illuminate the underlying mechanisms resulting in this interesting behavior.

Continuing on the discussion of Yb, we studied the "1-1-5" heavy fermion system $\mathrm{Ce}_{1-x}\mathrm{Yb}_x\mathrm{RhIn}_5$ and present the results in Chapter 3, which was guided by the study on related compound $\mathrm{Ce}_{1-x}\mathrm{Yb}_x\mathrm{CoIn}_5$. A comparison of the Co and Rh series show differences which are highlighted by the details that CeCoIn_5 has a SC ground state while CeRhIn_5 exhibits magnetic ordering which is modified by applied field and transitions into SC with applied pressure. We wanted to study the behavior of $\mathrm{Ce}_{1-x}\mathrm{Yb}_x\mathrm{RhIn}_5$ when Yb is introduced and compare it to $\mathrm{Ce}_{1-x}\mathrm{Yb}_x\mathrm{CoIn}_5$ in order to thoroughly understand the role of Yb in the 1-1-5 family of compounds. Remarkably, we find that in both systems, the valence of Yb decreases as Yb concentration is increased, while the valence of Ce stays the same. This is almost the opposite effect of what happens in $\mathrm{Yb}_{1-x}\mathrm{Sc}_x\mathrm{Co}_2\mathrm{Zn}_{20}$. The valence behavior of Yb in $\mathrm{Ce}_{1-x}\mathrm{Yb}_x\mathrm{RhIn}_5$ may also be related to the change in magnetic ordering going from incommensurate AFM to commensurate AFM. From the results presented in $\mathrm{Ce}_{1-x}\mathrm{Yb}_x\mathrm{CoIn}_5$, it is not unlikely for this valence behavior to be related to the modification of the electronic structure, and so it would not be out of the question to see this same related behavior in $\mathrm{Ce}_{1-x}\mathrm{Yb}_x\mathrm{RhIn}_5$. Much like in $\mathrm{Ce}_{1-x}\mathrm{Yb}_x\mathrm{CoIn}_5$, the system $\mathrm{Ce}_{1-x}\mathrm{Yb}_x\mathrm{RhIn}_5$ also exhibited interesting behavior where nominally substituted Yb did not replace Ce at a 1:1 ratio. This made it difficult to study Yb concentrations in the range $0.4 \leq x \leq 1$. If one were to follow up this study, focus on synthesizing high quality single crystals in this region and verifying both the valence behavior and the magnetic structure would provide a lot more information on this system without having to extrapolate based on the available data. Additionally, studies on the electronic structure could also highlight the similarities and differences between $Ce_{1-x}Yb_xRhIn_5$ and $Ce_{1-x}Yb_xCoIn_5$.

Chapter 4 presents an analogous study to $Ce_{1-x}Yb_xRhIn_5$, where the initial motivation is provided by the results of $Ce_{1-x}Yb_xCoIn_5$. The lanthanide Sm, much like Yb, can take on valence states of 3+ and 2+. Our goal was to determine whether Sm behaves analogously to Yb when substituted in for Ce in the heavy fermion superconductor $CeCoIn_5$. Additionally, the parent compound $SmCoIn_5$ displays three types of magnetic ordering, only one of which can be reasonably identified as an AFM ordering.[87] This provides potential motivation for studying the interaction between magnetic ordering and SC near $T = 0$ K. A similar study on $PuCoIn_5$ revealed SC likely due to proximity to an AFM QCP.[89] Since Pu has an analogous structure in the $5f$ shell versus the $4f$ electron shell of Sm, one might imagine that similar behavior can be observed in $SmCoIn_5$. No SC in the parent compound $SmCoIn_5$ was observed, however a robust AFM QCP was discovered at $x \approx 0.15$ in $Ce_{1-x}Sm_xCoIn_5$. The location of this QCP was also characterized by locally strong NFL behavior. This study provides yet another way of learning about the interaction between AFM and unconventional SC. This compound may be of further interest with additional studies in proximity of the QCP with additional measurement parameters or techniques. One might be interested in the behavior of this compound under magnetic field or applied pressure at dilution refrigerator temperatures. Also, a detailed study to uncover the nature of the three types of magnetic ordering from the parent $SmCoIn_5$ could shed a lot of light on this system.

In Chapter 5, we present an alternative explanation for the angle-dependent behavior of the various phases in URu_2Si_2 shown by Ref. 24. This explanation falls in line with the study presented by Scheerer *et al.* in Ref. 25, where the phases of URu_2Si_2, including the HO, are only sensitive to magnetic field applied along the *c*-axis. We continued these measurements on the $URu_{2-x}Fe_xSi_2$ system to determine whether this anisotropy extended throughout the phase diagram, considering $URu_{2-x}Fe_xSi_2$ goes through a LMAFM transition, and to see whether the HO and LMAFM phases could be distinguished with this technique. We found that the anisotropy of URu_2Si_2 carried over to the Fe-substituted series, even as it went through the LMAFM transition. Additionally, both the HO and LMAFM phases remained sensitive to the magnetic field in only the c-direction. These findings suggest that the underlying mechanisms for all the phases in URu_2Si_2 including those found under applied pressure[102] or magnetic field[23] are the same, and have strong anisotropy. This is consistent with the idea that the anisotropy of the g-factor is what drives these phases.[110,111] Finally, in addition to demonstrating the anisotropy of $URu_{2-x}Fe_xSi_2$ across a large range of T, H, and x, we showed with additional data that there may be another way of understanding the relationship between the LMAFM and the HO. Follow-up studies should certainly benefit from the vast amount of measurements performed on this system and can narrow down the search parameters to move us closer to revealing the true nature of the HO.

This dissertation hopefully demonstrates to the reader that chemical substitution is a very powerful way of probing and understanding the various exotic phenomena exhibited by correlated electron systems. In many systems, chemical substitution can allow more effective access to phases that typically require specialized measurement techniques to observe. Therefore, substitution studies can be a good method of surveying a compound without investing heavily into difficult measurement techniques until the basics of the system can be understood.

Bibliography

[1] M. S. Torikachvili, S. Jia, E. D. Mun, S. T. Hannahs, R. C. Black, W. K. Neils, D. Martien, S. L. Bud'Ko, and P. C. Canfield, Proceedings of the National Academy of Sciences **104**, 9960 (2007).

[2] T. Nasch, W. Jeitschko, and U. C. Rodewald, Zeitschrift Für Naturforschung B **52**, 1023 (1997).

[3] J. Kondo, Progress of theoretical physics **32**, 37 (1964).

[4] M. B. Maple, Applied physics **9**, 179 (1976).

[5] S. Jia, N. Ni, S. L. Budko, and P. C. Canfield, Phys. Rev. B **80**, 104403 (2009).

[6] K. Kadowaki and S. Woods, Solid state communications **58**, 507 (1986).

[7] H. Kamerlingh Onnes, Commun. Phys. Lab. Univ. Leiden, b **120** (1911).

[8] W. Meissner and R. Ochsenfeld, Naturwissenschaften **21**, 787 (1933).

[9] V. Ginzburg, Zh. eksper. teor. Fiz. **20**, 1064 (1950).

[10] J. Bardeen, L. N. Cooper, and J. R. Schrieffer, Physical Review **108**, 1175 (1957).

[11] J. G. Bednorz and K. A. Müller, Zeitschrift für Physik B Condensed Matter **64**, 189 (1986).

[12] M.-K. Wu, J. R. Ashburn, C. Torng, P. H. Hor, R. L. Meng, L. Gao, Z. J. Huang, Y. Wang, and a. Chu, Physical review letters **58**, 908 (1987).

[13] Y. Saiga, K. Matsubayashi, T. Fujiwara, M. Kosaka, S. Katano, M. Hedo, T. Matsumoto, and Y. Uwatoko, J. Phys. Soc. Jpn. **77**, 053710 (2008).

[14] K. D. Schotte and U. Schotte, Physics Letters A **55**, 38 (1975).

[15] M. B. Maple, J. W. Chen, Y. Dalichaouch, T. Kohara, C. Rossel, M. S. Torikachvili, M. W. McElfresh, and J. D. Thompson, Phys. Rev. Lett. **56**, 185 (1986).

[16] T. T. M. Palstra, A. A. Menovsky, J. V. d. Berg, A. J. Dirkmaat, P. H. Kes, G. J. Nieuwenhuys, and J. A. Mydosh, Phys. Rev. Lett. **55**, 2727 (1985).

[17] W. Schlabitz, J. Baumann, B. Pollit, U. Rauchschwalbe, H. M. Mayer, U. Ahlheim, and C. D. Bredl, Z. Phys. B Condens. Matter **62**, 171 (1986).

[18] H. Amitsuka, K. Matsuda, I. Kawasaki, K. Tenya, M. Yokoyama, C. Sekine, N. Tateiwa, T. Kobayashi, S. Kawarazaki, and H. Yoshizawa, J. Magn. Magn. Mater. **310**, 214 (2007).

[19] P. Das, N. Kanchanavatee, J. S. Helton, K. Huang, R. E. Baumbach, E. D. Bauer, B. D. White, V. W. Burnett, M. B. Maple, J. W. Lynn, et al., Phys. Rev. B **91**, 085122 (2015).

[20] N. Kanchanavatee, M. Janoschek, R. E. Baumbach, J. J. Hamlin, D. A. Zocco, K. Huang, and M. B. Maple, Phys. Rev. B **84**, 245122 (2011).

[21] C. T. Wolowiec, N. Kanchanavatee, K. Huang, S. Ran, and M. B. Maple, Physical Review B **94**, 085145 (2016).

[22] S. Ran, C. T. Wolowiec, I. Jeon, N. Pouse, N. Kanchanavatee, B. D. White, K. Huang, D. Martien, T. DaPron, D. Snow, et al., Proceedings of the National Academy of Sciences **113**, 13348 (2016).

[23] S. Ran, I. Jeon, N. Pouse, A. J. Breindel, N. Kanchanavatee, K. Huang, A. Gallagher, K.-W. Chen, D. Graf, R. E. Baumbach, et al., Proceedings of the National Academy of Sciences **114**, 9826 (2017).

[24] N. Kanchanavatee, M. Janoschek, K. Huang, B. D. White, P. S. Riseborough, A. V. Balatsky, and M. B. Maple, Philosophical Magazine **97**, 144 (2017).

[25] G. W. Scheerer, W. Knafo, D. Aoki, and J. Flouquet, Journal of the Physical Society of Japan **81**, SB005 (2012).

[26] S. Jang, B. White, P. Ho, N. Kanchanavatee, M. Janoschek, J. Hamlin, and M. Maple, Journal of Physics: Condensed Matter **26**, 425601 (2014).

[27] R. Baumbach, J. Hamlin, L. Shu, D. Zocco, J. OBrien, P.-C. Ho, and M. B. Maple, Physical review letters **105**, 106403 (2010).

[28] L. Shu, R. E. Baumbach, M. Janoschek, E. Gonzales, K. Huang, T. A. Sayles, J. Paglione, J. OBrien, J. J. Hamlin, D. A. Zocco, et al., Phys. Rev. Lett. **106**, 156403 (2011).

[29] S.-J. Oh, S. Suga, A. Kakizaki, M. Taniguchi, T. Ishii, J.-S. Kang, J. W. Allen, O. Gunnarsson, N. E. Christensen, A. Fujimori, et al., Physical Review B **37**, 2861 (1988).

[30] P. C. Canfield and Z. Fisk, Philosophical magazine B **65**, 1117 (1992).

[31] A. C. Larson and R. von Dreele, Los Alamos National Laboratory Report LAUR pp. 86–748 (2000).

[32] H. M. Rietveld, J. Appl. Cryst. **2**, 65 (1969).

[33] T. Takeuchi, S. Yoshiuchi, M. Ohya, Y. Taga, Y. Hirose, K. Sugiyama, F. Honda, M. Hagiwara, K. Kindo, R. Settai, et al., Journal of the Physical Society of Japan **80**, 114703 (2011).

[34] L. Vegard, Physik **5**, 17 (1921).

[35] M. B. Maple and D. Wohlleben, Physical review letters **27**, 511 (1971).

[36] M. B. Maple and D. Wohlleben, in *AIP Conference Proceedings* (AIP, 1974), vol. 18, pp. 447–462.

[37] R. D. Shannon, Acta crystallographica section A: crystal physics, diffraction, theoretical and general crystallography **32**, 751 (1976).

[38] S. Jang, N. Pouse, T. Keiber, B. D. White, S. M. Disseler, J. W. Lynn, J. C. Collini, M. Janoschek, F. Bridges, and M. B. Maple, Physical Review B **98**, 195118 (2018).

[39] L. Dudy, J. D. Denlinger, L. Shu, M. Janoschek, J. W. Allen, and M. B. Maple, Phys. Rev. B **88**, 165118 (2013).

[40] S. Jang, B. D. White, I. K. Lum, H. Kim, M. A. Tanatar, W. E. Straszheim, R. Prozorov, T. Keiber, F. Bridges, L. Shu, et al., Phil. Mag. **94**, 4219 (2014).

[41] T. Muramatsu, N. Tateiwa, T. C. Kobayashi, K. Shimizu, K. Amaya, D. Aoki, H. Shishido, Y. Haga, and Y. Onuki, J. Phys. Soc. Jpn. **70**, 3362 (2001).

[42] J. S. Kim, J. Alwood, G. R. Stewart, J. L. Sarrao, and J. D. Thompson, Phys. Rev.

B **64**, 134524 (2001).

[43] J. Paglione, M. A. Tanatar, D. G. Hawthorn, E. Boaknin, R. W. Hill, F. Ronning, M. Sutherland, L. Talilefer, C. Petrovic, and P. C. Canfield, Phys. Rev. Lett. **91**, 246405 (2003).

[44] A. D. Bianchi, R. Movshovich, N. Oeschler, P. G. Paliuso, and J. L. Sarrao, Phys. Rev. Lett. **91**, 257001 (2003).

[45] T. Park, F. Ronning, H. Q. Yuan, M. B. Salamon, R. Movshovich, J. L. Sarrao, and J. D. Thompson, Nature **440**, 65 (2006).

[46] S. Raymond, E. Ressouche, G. Knebel, D. Aoki, and J. Flouquet, J. Phys.: Condens. Matter **19**, 242204 (2007).

[47] G. Knebel, D. Aoki, D. Braithwaite, B. Salce, and J. Flouquet, Phys. Rev. B **74**, 020501(R) (2006).

[48] G. F. Chen, K. Matsubayashi, S. Ban, K. Deguchi, and N. K. Sato, Phys. Rev. Lett. **97**, 017005 (2006).

[49] B. D. White, J. D. Thompson, and M. B. Maple, Physica C **514**, 246 (2015).

[50] W. Bao, P. G. Pagliuso, J. L. Sarrao, J. D. Thompson, Z. Fisk, J. W. Lynn, and R. W. Erwin, Phys. Rev. B **62**, R14621 (2000).

[51] P. Das, S.-Z. Lin, N. J. Ghimire, K. Huang, F. Ronning, E. D. Bauer, J. D. Thompson, C. D. Batista, G. Ehlers, and M. Janoschek, Phys. Rev. Lett. **113**, 246403 (2014).

[52] A. L. Cornelius, P. G. Pagliuso, M. F. Hundley, and J. L. Sarrao, Phys. Rev. B. **64**, 144411 (2001).

[53] D. M. Fobes, S. Zhang, S.-Z. Lin, P. Das, N. Ghimire, E. Bauer, J. Thompson, L. Harriger, G. Ehlers, A. Podlesnyak, et al., Nature Physics **14**, 456 (2018).

[54] F. Ronning, T. Helm, K. R. Shirer, M. D. Bachmann, L. Balicas, M. K. Chan, B. J. Ramshaw, R. D. McDonald, F. F. Balakirev, M. Jaime, et al., Nat. Lett. **548**, 313 (2017).

[55] C. Capan, G. Seyfarth, D. Hurt, B. Prevost, S. Roorda, A. D. Bianchi, and Z. Fisk, Europhys. Lett. **92**, 47004 (2010).

[56] C. Booth, T. Durakiewicz, C. Capan, D. Hurt, A. Bianchi, J. Joyce, and Z. Fisk, Phys. Rev. B **83**, 235117 (2011).

[57] B. D. White, J. J. Hamlin, K. Huang, L. Shu, I. K. Lum, R. E. Baumbach, M. Janoschek, and M. B. Maple, Phys. Rev. B **86**, 100502 (2012).

[58] Y. P. Singh, D. J. Haney, X. Y. Huang, B. D. White, M. B. Maple, M. Dzero, and C. C. Almasan, Phys. Rev. B **91**, 174506 (2015).

[59] M. Shimozawa, T. Watashige, S. Yasumoto, Y. Mizukami, M. Nakamura, H. Shishido, S. K. Goh, T. Terashima, T. Shibauchi, and Y. Matsuda, Phys. Rev. B **86**, 144526 (2012).

[60] A. Polyakov, O. Ignatchik, B. Bergk, K. Götze, A. D. Bianchi, S. Blackburn, B. Prévost, G. Seyfarth, M. Côté, D. Hurt, et al., Phys. Rev. B **85**, 245119 (2012).

[61] T. Hu, Y. P. Singh, L. Shu, M. Janoschek, M. Dzero, M. B. Maple, and C. C. Almasan, Proc. Nat. Acad. Sci. **110**, 7160 (2013).

[62] H. Kim, M. A. Tanatar, R. Flint, C. Petrovic, R. Hu, B. D. White, I. K. Lum, M. B. Maple, and R. Prozorov, Phys. Rev. Lett. **114**, 027003 (2015).

[63] Y. Xu, J. K. Dong, I. K. Lum, J. Zhang, X. C. Hong, L. P. He, K. F. Wang, Y. C. Ma, C. Petrovic, M. B. Maple, et al., Phys. Rev. B **93**, 064502 (2016).

[64] V. S. Zapf, N. A. Frederick, K. L. Rogers, K. D. Hof, P. C. Ho, E. D. Bauer, and M. B. Maple, Phys. Rev. B. **67**, 064405 (2003).

[65] V. Zaremba, U. C. Rodewald, R.-D. Hoffmann, Y. M. Kalychak, and R. Poettgen, Zeitschrift für anorganische und allgemeine Chemie **629**, 1157 (2003).

[66] J. W. Lynn, Y. Chen, S. Chang, Y. Zhao, S. Chi, W. Ratcliff, II, B. G. Ueland, and R. W. Erwin, Journal of Research of NIST **117**, 61 (2012).

[67] W. H. McMaster, N. Kerr Del Grande, J. H. Mallett, and J. H. Hubbell, Atomic Data and Nuclear Data Tables **8**, 443 (1970).

[68] C. MacKeen, F. Bridges, L. Seijo, Z. Barandiarán, M. Kozina, A. Mehta, M. F. Reid, and J.-P. R. Wells, J. Phys. Chem. C **121**, 2843528442 (2017).

[69] A. D. Christianson, J. M. Lawrence, P. G. Pagliuso, N. O. Moreno, J. L. Sarrao, J. D. Thomson, P. S. Riseborough, S. Kern, E. A. Goremychkin, and A. H. Lacerda,

Phys. Rev. B **66**, 193102 (2002).

[70] A. D. Christianson, E. D. Bauer, J. M. Lawrence, P. S. Riseborough, N. O. Moreno, P. G. Pagliuso, J. L. Sarrao, J. D. Thompson, E. A. Goremychkin, F. R. Trouw, et al., Phys. Rev. B **70**, 134505 (2004).

[71] B. E. Light, Ravhi, S. Kumar, A. L. Cornelius, P. G. Pagliuso, and J. L. Sarrao, Phys. Rev. B. **69**, 024419 (2004).

[72] J. S. Kim, J. Alwood, D. Mixson, P. Watts, and G. R. Stewart, Phys. Rev. B **66**, 134418 (2002).

[73] T. Willers, F. Strigari, Z. Hu, V. Sessi, N. B. Brookes, E. D. Bauer, J. L. Sarrao, J. D. Thompson, A. Tanaka, S. Wirth, et al., Proc. Nat. Acad. Sci. **112**, 2384 (2015).

[74] P. J. W. Moll, T. Helm, S.-S. Zhang, C. D. Batista, N. Harrison, R. D. McDonald, L. E. Winter, B. J. Ramshaw, M. K. Chan, F. F. Balakirev, et al., npj Quantum Materials **2**, 46 (2017).

[75] D. M. Fobes, E. D. Bauer, J. D. Thompson, A. Sazonov, V. Hutanu, S. Zhang, F. Ronning, and M. Janoschek, J. Phys.: Condens. Mat. **29**, 17LT01 (2017).

[76] W. Bao, G. Aeppli, J. W. Lynn, P. G. Pagliuso, J. L. Sarrao, M. F. Hundley, J. D. Thomson, and Z. Fisk, Phys. Rev. B **65**, 100505(R) (2002).

[77] R. T. Azuah, L. R. Kneller, Y. Qiu, P. L. W. Tregenna-Piggott, C. M. Brown, J. R. D. Copley, and R. M. Dimeo, Journal of Research of NIST **114**, 341 (2009).

[78] P. Gegenwart, Q. Si, and F. Steglich, Nature **4**, 186 (2008).

[79] F. Steglich, J. Arndt, S. Friedemann, C. Krellner, Y. Toskiwa, T. Westerkamp, M. Brando, P. Gegenwart, C. Geibel, S. Wirth, et al., J. Phys.: Condens. Matter **22**, 164202 (2010).

[80] J. D. Thompson and Z. Fisk, J. Phys. Soc. Jpn **81**, 011002 (2012).

[81] G. R. Stewart, Rev. Mod. Phys. **56**, 755 (1984).

[82] F. Steglich, C. Geibel, R. Modler, M. Lang, P. Hellmann, and P. Gegenwart, J. Low Temp. Phys. **99**, 267 (1995).

[83] C. Petrovic, P. G. Pagliuso, M. F. Hundley, R. Movshovich, J. L. Sarrao, J. D. Thompson, and Z. Fisk, J. Phys.: Condens. Matter **13**, L337 (2001).

[84] L. H. Greene, W. K. Park, J. L. Sarrao, and J. D. Thompson, Physica B **378**, 671 (2006).

[85] B. B. Zhou, S. Misra, E. H. da Silva Neto, P. Aynajian, R. E. Baumbach, J. D. Thompson, E. D. Bauer, and A. Yazdani, Nat. Phys. **9**, 474 (2013).

[86] M. P. Allan, F. Massee, D. K. Morr, J. Van Dyke, A. W. Rost, A. P. Mackenzie, C. Petrovic, and J. C. Davis, Nat. Phys. **9** (2013).

[87] Y. Inada, M. Hedo, T. Fujiwara, T. Sadamasa, and Y. Uwatoko, Physica B **378**, 421 (2006).

[88] M. Koeda, M. Hedo, T. Fujiwara, Y. Uwatoko, T. Sadamasa, and Y. Inada, J. Phys. Soc. Jpn. **76**, 62 (2007).

[89] E. D. Bauer, M. M. Altarawneh, P. H. Tobash, K. Gofryk, O. E. Ayala-Valenzuela, J. N. Mitchell, R. D. McDonald, C. H. Mielke, F. Ronning, J.-C. Griveau, et al., J. Phys.: Condens. Matter **24**, 052206 (2012).

[90] O. Erten, R. Flint, and P. Coleman, Phys. Rev. Lett. **114**, 027002 (2015).

[91] M. Kasaya, B. Liu, M. Sera, T. Kasuya, D. Endoh, T. Goto, and T. Fujimura, J. Magn. Magn. Mater. **52**, 289 (1985).

[92] T. U. Ito, W. Higemoto, K. Ninomiya, H. Luetkens, T. Sugai, Y. Haga, and H. S. Suzuki, J. Magn. Magn. Mater. **80**, 033701 (2011).

[93] J. H. Van Vleck, *The theory of electric and magnetic susceptibilities* (Oxford University Press, 1932).

[94] U. I. Takashi, W. Higemoto, K. Ninomiya, H. Luetkens, T. Sugai, Y. Haga, and H. S. Suzuki, J. Phys. Soc. Jpn. **80**, 033710 (2011).

[95] P. G. Pagliuso, J. D. Thompson, M. F. Hundley, J. L. Sarrao, and Z. Fisk, Phys. Rev. B **63**, 054426 (2001).

[96] V. S. Zapf, E. J. Freeman, E. D. Bauer, J. Petricka, C. Sirvent, N. A. Frederick, R. P. Dickey, and M. B. Maple, Phys. Rev. B **65**, 014506 (2001).

[97] J. R. Jeffries, N. A. Frederick, E. D. Bauer, H. Kimura, V. S. Zapf, K.-D. Hof, T. A. Sayles, and M. B. Maple, Phys. Rev. B **72**, 024551 (2005).

[98] B. E. Light, R. S. Kumar, A. L. Cornelius, P. G. Pagliuso, and J. L. Sarrao, Phys. Rev. B **69**, 024419 (2004).

[99] M. B. Maple, Physica B **215**, 110 (1995).

[100] J. Paglione, T. A. Sayles, P.-C. Ho, J. R. Jeffries, and M. B. Maple, Nat. Phys. **3**, 703 (2007).

[101] J. A. Mydosh and P. M. Oppeneer, Philosophical Magazine **94**, 3642 (2014).

[102] N. P. Butch, J. R. Jeffries, S. Chi, J. B. Leão, J. W. Lynn, and M. B. Maple, Phys. Rev. B **82**, 060408 (R) (2010).

[103] M. Jaime, K. Kim, G. Jorge, S. McCall, and J. Mydosh, Physical review letters **89**, 287201 (2002).

[104] M. N. Wilson, T. J. Williams, Y.-P. Cai, A. M. Hallas, T. Medina, T. J. Munsie, S. C. Cheung, B. A. Frandsen, L. Liu, Y. J. Uemura, et al., Physical Review B **93**, 064402 (2016).

[105] E. Bauer, V. Zapf, P.-C. Ho, N. Butch, E. Freeman, C. Sirvent, and M. Maple, Physical review letters **94**, 046401 (2005).

[106] Y. Jo, L. Balicas, C. Capan, K. Behnia, P. Lejay, J. Flouquet, J. Mydosh, and P. Schlottmann, Physical review letters **98**, 166404 (2007).

[107] E. Hassinger, G. Knebel, T. Matsuda, D. Aoki, V. Taufour, and J. Flouquet, Physical review letters **105**, 216409 (2010).

[108] N. Harrison, M. Jaime, and J. Mydosh, Physical review letters **90**, 096402 (2003).

[109] D. Aoki, F. Bourdarot, E. Hassinger, G. Knebel, A. Miyake, S. Raymond, V. Taufour, and J. Flouquet, Journal of Physics: Condensed Matter **22**, 164205 (2010).

[110] H. Ohkuni, Y. Inada, Y. Tokiwa, K. Sakurai, R. Settai, T. Honma, Y. Haga, E. Yamamoto, Y. Ōnuki, H. Yamagami, et al., Philosophical Magazine B **79**, 1045 (1999).

[111] M. M. Altarawneh, N. Harrison, S. E. Sebastian, L. Balicas, P. H. Tobash, J. D.

Thompson, F. Ronning, and E. D. Bauer, Physical review letters **106**, 146403 (2011).